Design and Realization of Thin Acoustic Metamaterials and Ventilated Metamaterials for Aerospace Applications

A Thesis Submitted

In Partial Fulfilment of the Requirements

for the Degree Of

DOCTOR OF PHILOSOPHY

by

Sanjeet Kumar Singh

(Roll No. 18119264)

Under the supervision of

Prof. Shantanu Bhattacharya

to the

DEPARTMENT OF DESIGN

INDIAN INSTITUTE OF TECHNOLOGY KANPUR

Kanpur, Uttar Pradesh- 208016, India

February , 2024

Certificate

It is acknowledged that the work done by Sanjeet Kumar Singh, for his thesis "**Design and Realization of Thin Acoustic Metamaterials and Ventilated Metamaterials for Aerospace Applications**," was completed under my supervision and was not previously submitted for credit.

16/02/2024

Dr. Shantanu Bhattacharya
Department of Mechanical Engineering
and Former HOD of Department of Design
IIT Kanpur

February, 2024

DECLARATION

This is to certify that the thesis titled "**Design and Realization of Thin Acoustic Metamaterials and Ventilated metamaterials for Aerospace Applications**" has been authored by me. It presents the research conducted by me under the supervision of **Prof. Shantanu Bhattacharya**.

To the best of my knowledge, it is an original work, both in terms of research content and narrative, and has not been submitted elsewhere, in part or in full, for a degree. Further, due credit has been attributed to the relevant state-of-the-art and collaborations (if any) with appropriate citations and acknowledgements, in line with established norms and practices.

Name: Sanjeet Kumar Singh

(18119264)

Programme: PhD

Department: Department of Design

Indian Institute of Technology Kanpur

Kanpur 208016

SYNOPSIS

Design and Realization of Thin Acoustic Metamaterials and Ventilated metamaterials for Aerospace Applications

By

Sanjeet Kumar Singh

Roll No. 18119264

Submitted to the Department of Design on **February ,2024** in Partial Fulfillment of the Requirements for the Degree of **Doctor of Philosophy** in **Department of Design**

Thesis Supervisor: Dr. Shantanu Bhattacharya

Professor, Mechanical Engineering Department and Former Department Head, Department of Design

---

Being exposed to loud noises can lead to hearing impairment, stress, and difficulties in communication. Active noise cancelling piezo - electric materials, passive foams/foam-like materials and acoustic metamaterials (near-zero, single negative, double negative) are common forms of noise dampening alternatives currently in use, although each has its own set of drawbacks. For the passive foam materials, for instance, weight and volume are issues because they are quite heavy and occupy a high level of space. Certain vehicles, like aircraft, may have heavy foam put inside them, which is a major reason for increased fuel consumption and decreased operational efficiency. Although piezo-based systems may be lighter or smaller than foams, they still need control hardware, circuits, power supply etc. These materials frequently exhibit poor sound absorption characteristics particularly in the low frequency domain, necessitating the use of thicker structures with dimensions corresponding to the working wavelength of acoustic signals. For application, such as damping within aircrafts the component sizes and weights are rigorously

restricted and the noise damping structures may be overtly thick or heavy and thus an engineering tradeoff between the noise absorption, the volume occupancy and the weight addition leads to a very challenging situation. There is a need in the aerospace industry for a thin, lightweight, high sound-absorbing material. Many solutions like passive or active meta-materials are realized for catering to these challenges. Most sub-wavelength acoustic absorbers exhibit good sound absorption in a specific frequency band, however the difficulty with that type of structure is that it is not adaptive to band shifting once it is created. Many researchers have continued to examine the integration of SMPs (Shape-memory polymer) materials in acoustic meta-structures because of the ability to change physical properties with external inputs. Therefore, it is intriguing to think that a new generation of "auto-reconfigurable" AMMs may soon appear, offering performance far superior to the state of the art and enabling novel wave functionalities like tunable focusing, broadband cloaking, dynamic signal processing, and programmable analogue computing.

We focused our efforts in this work on creating, realizing, characterizing, and applying the concept of metamaterials to two separate aspects of science and technology. In one domain, we aim for sound reduction without air circulation by employing a back plate that does not allow acoustic air to pass through. In the other domain, we have created some new designs of 1D and 2D ventilated acoustic metamaterials with air circulation that absorb sound while also allowing acoustic air to travel through. All of the unique metamaterial designs have been created utilizing a 3D printing machine using fused filament fabrication (FFF) procedure.

In this thesis, we have created and designed metamaterials to address this issue from a passive aerostructure point of view. In airplanes, the engine and turbulent airflow around the fuselage typically produces low frequency excitations and this has been identified as

the primary source of cabin noise. The target frequency range for noise damping standpoint further varies between turbofan and turbojets. The turbojet generates a high-velocity exhaust flow that dominates other noise sources, especially at low frequencies (200Hz -800Hz). Turbofans, on the other hand, produce high-frequency noise (1000Hz to 1600Hz). Therefore, the primary objective of our research has been to develop structural designs of materials which are realizable through 3-D printing to develop test size coupons and eventually integrated to a scaleup process relevant to aerospace manufacturing. The designs developed possess thin cross-sections and are amenable to low and medium frequency band sound mitigation. The first design that we have created has been inspired from the famous Ashok Chakra structure which show high tunability independent of thickness. With this design scaled at subwavelength dimensions ($\lambda/7$), almost perfect sound absorption (>99%) is observed. This structure however shows only single-frequency sound absorption behavior once realized and cannot change to variable acoustic emission spectra. Thus, in a way the structure once planned for a specific frequency range and optima may only serve a specific situation and in a way has limited application from damping of dynamic acoustic signals. There has always been a need for a thin sound absorber that can shrink the vertical and lateral dimensions simultaneously while obtaining multiple narrow banded absorption peaks. To address these challenges, we have designed the next solution to get multiple narrow band low frequency sound absorption through realization of the fractal acoustic metamaterials. (FAM) Numerous validations have been conducted using numerical modelling efforts (FEM simulations), closed form analytical solutions (based on equivalent impedance analysis), and experimental analysis. We have also tried conventional micro-perforated panels (MPP), with back cavity made out of FAM designs to obtain the cascade neck-embedded Helmholtz resonator effect with a back cavity of ultra-thin nature (thickness < 2 cm) We

have achieved near perfect absorption around 1000 Hz, with a broadband absorption bandwidth. Approximately 1 octave band sound absorption coefficient > 0.5 have been achieved with single unit cell and more than 0.8 has been achieved within the frequency range 600–1100 Hz. Maximum relative sound absorption bandwidth of 76% has been achieved with an integrated two-unit cell configuration and 61% with 4-unit cell combination. The sound absorption coefficient has been increased by integrating the unit cells.

Although the previously developed structures have been effective at absorbing sound, they have also been obstruction to the airflow necessitating the development of a structure that could do both sound-insulation and air ventilation. Earlier geometries have always been compromised in a way as most of them have created noise damping through barrier effect which is sometimes detrimental to the structure as such. To address these challenges, we have also proposed one-dimensional meta-materials (kink fiber) which allow passage to the air flow while absorbing the incident sound wave (little reflection) in the low- to mid-frequency region (800-1600 Hz). These structures are made with a viewpoint to only muffle the sound over 800 Hz and not low frequency noise which is what jet engines typically produce and transmit into the aircraft cabin. Thus, while the air flow through ventilated passageways may result in good reliability of the shrouds and the dampening structures the basic purpose of meeting the absorption frequency range is unmet. To address these challenges, we have further designed and developed a subwavelength-thin (1.4~3.5 cm) metamaterial structure inspired by a flat Fresnel spiral with good ventilation capacity to obtain broadband multiple sound absorption peaks in the frequency range of 0–1600 Hz. Very low frequency sound (roughly 200Hz) and broadband more than one octave while maintaining air circulation of 5~12% is also

obtained. Further a variation of vacuum pressure within such intelligent materials has always led to increased absorption coefficients at less than 200Hz frequency.

In conclusion, we have designed and created five different types of acoustic metamaterials panels for aircraft applications. Three of them are concerned with establishing targeted frequency sound absorption, multiple frequency sound absorption, and broadband sound absorption, while the other two are concerned with air ventilation in addition to sound absorption. We believe that our proposed designs will have a wide range of applications in noise control, and that the theoretical models produced will provide a solid foundation for building high-efficiency acoustic panels, silencers, and barriers with high ventilation and sound absorption.

ACKNOWLEDGEMENT

I'd like to offer my heartfelt gratitude and admiration to Prof. Shantanu Bhattacharya, my thesis advisor, for his unwavering support over the previous few years. This work would not have been possible without his guidance and technical skill in acoustic metamaterials, for which I am eternally thankful. I have evolved as a researcher and a better human being as a result of my learning experiences in numerous courses at the institution and in the lab, and I hope that I have contributed to these expanding domains.

I'd like to also thank Dr. Om Prakash (Director, Boeing India) for his invaluable advice on acoustic metamaterials. I am appreciative for his help at various phases.

I'd like to thank my lab colleagues, Dr. Kapil Manoharan, Dr. Rishi Kant, Rashik and others for cultivating a positive working environment in the lab. Dr. Govind Sahu, Sidhant Shrivastava, Saurabh Gupta, and other friends have always assisted me in making decisions during my research work.

I extend my gratitude to Prof. Nachiketa Tiwari, current head of the Department of Design for their assistance and support.

Most importantly, I'd like to express my gratitude to my family for their unending support. My parents have always given me the confidence to make the correct choices. I'd like to thank my sisters (Sanju Didi and younger sister Durga). This thesis would not have been possible without their assistance.

BIOGRAPHICAL NOTE

Educations

- 2018- 2023. P.hD., Department of Design, Indian Institute of Technology Kanpur, Uttar Pradesh 208016, India
- 2012-2014- MTech., Machine Design, Guru Ghasidas Vishwavidyalaya, (Central University) Bilaspur, Chhattisgarh, India
- 2008-2012- B.Tech., Mechanical Engineering, Guru Ghasidas Vishwavidyalaya, (Central University) Bilaspur, Chhattisgarh, India

IPRs/Patents

1. Sanjeet Kumar Singh, Om Prakash, Megha Sahu, Shantanu Bhattacharya, "Acoustic metamaterials with discreet band absorption through planer fractal geometries" US patent Application (Field, 2022)
2. Sanjeet Kumar Singh, Shantanu Bhattacharya," Helmholtz metamaterial noise blocker: a novel material for acoustic insulation", Application No. 395885-001 (2023), Under Review, Indian
3. Sanjeet Kumar Singh, Saurabh Gupta, Dr. Syam Nair, Shantanu Bhattacharya," Three-dimensional adjustable video recording setup for smartphones", (Serial Number: 335731-001) awarded on 2022/6/1.
4. Sanjeet Kumar Singh, Saurabh Gupta, Vaishali Jain," Reusable drinking steel straw cum portable hiking cutlery set" (Serial Number: 343134-001) awarded on 2022/5/18.
5. Sanjeet Kumar Singh," Relax and read: Bookshelf and Chair in One", (Serial Number: 357518-001) awarded on 2023/3/30.
6. Sanjeet Kumar Singh, Saurabh Gupta," Sound Amplifier and Reflector for Smart Phones" (Serial Number: 356893-001) awarded on 2023/3/30.
7. Sanjeet Kumar Singh, Saurabh Gupta, Vaishali Jain," Reusable drinking steel straw cum portable hiking kit box" (Serial Number: 343129-001) awarded on 24/04/2023.
8. Sanjeet Kumar Singh, Saurabh Gupta, Dr. Syam Nair, Shantanu Bhattacharya," Collapsible Multiple Drawing Sheets Holding Device", (Application No: 332952-001) Filed on 2019.

9. Sanjeet Kumar Singh, Saurabh Gupta, Dr. Syam Nair, Vaishali Jain," "Reusable drinking straw cum portable multipurpose cutlery set Inbox", (Application No: 202111016769) Filed on 2022.
10. Sanjeet Kumar Singh, Saurabh Gupta," A customized and user-friendly sound amplifier and reflector for smart phone/ iPhone", (Application No: 356889-001.) , Filed on 2022.
11. Sanjeet Kumar Singh, Saurabh Gupta," Smartphone/Tablet stand with adjustable height and angle cum accessories storage box: Open view.**"** (Application No: 369741-001), Filed on 2022
12. Sanjeet Kumar Singh, Saurabh Gupta,": "Smartphone/Tablet stand with adjustable height and angle cum accessories storage box: Closed view.**"** (Application No: 369740-001), Filed on 2022

Publications[1]

Journals

1. Bhattacharya S, Kumar S, **Singh SK**, Bhushan P, Sahu M, Prakash O. Ashok chakra-structured meta-structure as a perfect sound absorber for broadband low-frequency sound. *Appl Phys Lett*. 2020;117(19). doi:10.1063/5.0022998

2. **Singh SK**, Prakash O, Bhattacharya S. Novel fractal acoustic metamaterials (FAMs) for multiple narrow-band near-perfect absorption. *J Appl Phys*. 2022;132(3). doi:10.1063/5.0093128

3. **Singh SK**, Prakash O, Bhattacharya S. Hybrid fractal acoustic metamaterials for low-frequency sound absorber based on cross mixed micro-perforated panel mounted over the fractals structure cavity. *Sci Rep*. 2022;12(1):1-9. doi:10.1038/s41598-022-24621-8

4. **Singh SK**, Bhattacharya S." Flat Fresnel spiral acoustic metamaterials composed of several arms ventilated metamaterials for simultaneous broadband sound absorption and air circulation" August 2022, doi: 10.3397/IN_2022_0058

5. **Singh SK**, Prakash O, Bhattacharya S. Design and development of One dimensional acoustic ventilated metamaterial, Submitted to Applied acoustics, 2024. (Under review)

6. **Singh SK**, Prakash O, Bhattacharya S." Recent progress in programmable acoustic metamaterials and their principles"**,** Submitted to Journal of Micromanufacturing, 2024. (Under Review)

7. **Singh SK**, Bhattacharya S. " Design of aesthetic acoustic metamaterials window panel based on Sierpinski triangle for sound-silencing with airflow" The journal of the Acoustical Society of America, 2023, 154, doi: 10.1121/10.0023103.

---

[1] Based on thesis.

Conference Proceedings

- Sanjeet Kumar Singh, Shantanu Bhattacharya," Flat Fresnel spiral acoustic metamaterials composed of several arms ventilated metamaterials for simultaneous broadband sound absorption and air circulation", 51st international congress and exposition on Noise Control Engineering 21-24, August 2022 Scottish Event Campus (SEC),Glasgow, Scotland. Pages 1-998, pp. 408-416(9), Institute of Noise control Engineering ,https://doi.org/10.3397/IN_2022_0058
- Sanjeet Kumar Singh, Shantanu Bhattacharya," Design of aesthetic acoustic metamaterials window panel based in Sierpinski triangle for sound-silencing with free airflow",AcousticSydney 2023, ICC Sydney, Australia.
-

Book Chapter

- Sanjeet Kumar Singh, Rishi kant, Shanatanu Bhattacharya," Shape Memory Polymers and Their Emerging Applications,"Trend in Fabrication of polymer and composites,2022, chapter 8, AIP publishing Melville,NewYork.

Awards

- 2nd Prize in Startup Conclave-2022, idea pitching completion.
- Top 20 finalists in ideation, a competitive event conducted by Startup masterclass, IT Kanpur 2021
- Certificate of appreciation," Judge the conference titled" mechanical Engineering and Design" at Students Research Convention 2021.
- 1st prize in the Logo Competition for GATE 2023 organized by GATE-JAM office, IIT Kanpur
- Awarded DST -NIDHI-EIR Fund (for developing the "Low-Cost land area mapping devices at IIT Kanpur (Team members: Sanjeet Kumar Singh, Saurabh Gupta)

TABLE OF CONTENTS

LIST OF FIGURES

LIST OF TABLES

NOMENCLATURE

SMPs	=	Shape memory polymers
AMMs	=	Acoustic Metamaterials
FFF	=	Fused filament fabrication
FAM	=	Fractal acoustic metamaterial
MPP	=	Micro-perforated panels
GMM	=	Glass woven mat
SHF	=	Straight silicon hollow fibre
KF	=	Kink fibre
YAM	=	“Y” type kink fibre
CDAM	=	Converging diverging kink fibre
IRAM	=	Internal resonators kink fibre
VAM	=	Ventilated acoustic metamaterials
UVAM	=	Uniform ventilated metamaterial
RTVAM	=	Rainbow trapping ventilated acoustic metamaterial

Chapter 1 : Introduction

In our everyday experience, we encounter a variety of ways in which sound interacts with material medium while propagating. Sound waves can resonate through valleys, covering significant distances. Different musical instruments elicit diverse frequencies, offering unique auditory pleasures. Conversely, sound can disrupt both sleep and work routines. Amid these sound occurrences, resulting noise pollution, emanating from sources like vehicle, industrial, or domestic sounds poses a growing challenge to human well-being and comfort.

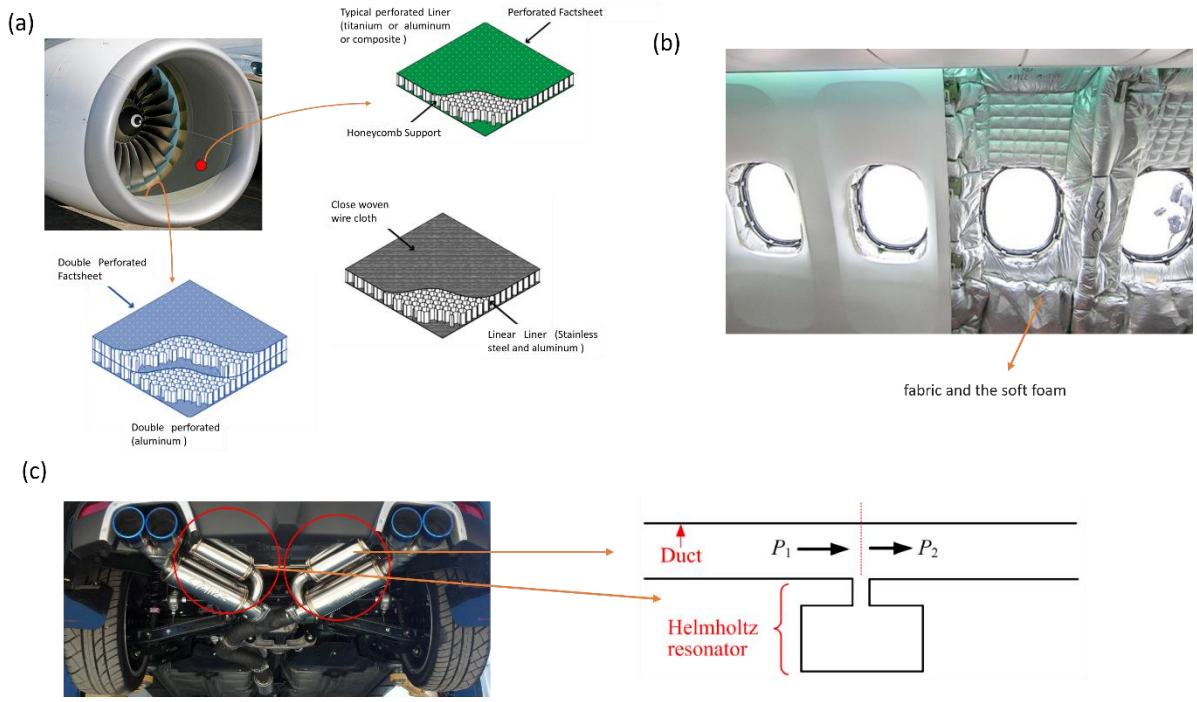

Figure 1.1: Traditional methods for reducing noise and shaping the acoustic environment.[1], [2] (a) Micro-perforated panels used in aerospace jet; (b) Fabric and soft foam in cockpit; (c) Helmholtz resonators in automobile

In response to the escalating need for lower noise levels, regulations regarding the environmental impact of commercial products have become increasingly stringent.

Developed nations and regulatory bodies have established rigorous noise reduction standards to ensure a habitable environment. A common industrial approach to address noise reduction involves the implementation of passive sound-absorbing structure.

Figure 1.1 depicts traditional methods for reducing noise. The human aspiration to comprehend and control sound waves or diminish sound intensity has persisted throughout history.

The acoustic theory significantly contributes to a comprehensive understanding of both the quantitative and qualitative aspects of sound propagation. In broad terms, a sound wave represents a synchronized series of oscillations. Proficiency in comprehending damped harmonic oscillation is crucial for delving into the intricacies of sound. In this context, the aim of this thesis is to examine sound absorption, manipulate sound waves, and attenuate noise signals in metamaterials.

1.1 Sound, Noise and Acoustic

It is believed that humans have the ability to hear before birth.[3] Once born, we can recognize information communicated by sound, appreciate, and produce sound. One of the most essential and critical senses for our learning and understanding of the world is hearing. Sound is essential for many facets of life, including communication, collaboration, artistic expression, time management and many more. From the smallest living cells in the human body to the largest skyscraper, everything vibrates and emits sound. In the tapestry of our sensory world, sound waves paint a vivid and ever-changing portrait of the environment around us. These waves, composed of alternating compressions and rarefactions of air molecules, create the melodious symphony of life. As we delve into the intricacies of sound

waves, we uncover the mechanisms that bring music to our ears, voices to our conversations, and the distant roar of thunder to our senses. As the source vibrates, it compresses the air molecules in front of it, creating a region of high pressure known as compression. Simultaneously, it pulls the air molecules behind it apart, creating an area of low pressure called rarefaction. This cyclical pattern of compressions and rarefactions propagates outward from the source, creating a sound wave that eventually reaches our ears as shown in Figure 1.2.[4]

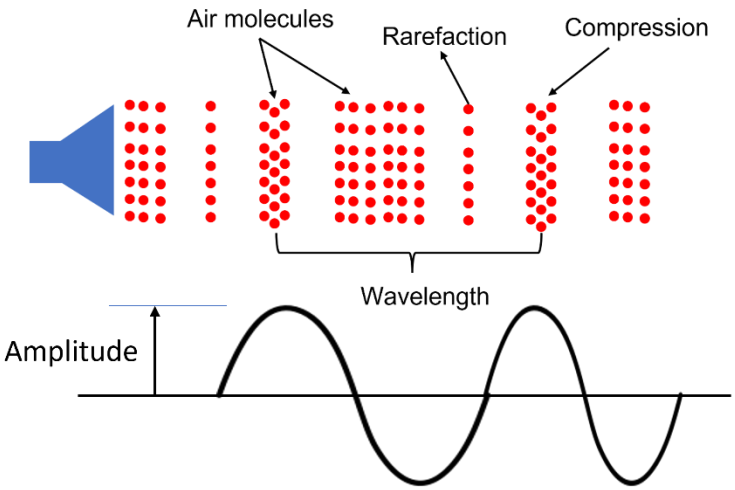

Figure 1.2:Image of sound waves moving through air particles.

In the midst of the harmonious melodies that dance through our auditory landscape, noise emerges as an unwelcome disruptor. Unlike the organized patterns of sound waves that create music and conversation, noise is characterized by its lack of rhythm and structure. It is an intrusive cacophony that can range from the distant hum of machinery to the jarring blare of horns in a bustling city. Noise not only disturbs our tranquility but also impacts our well-being, affecting concentration, sleep, and overall quality of life. As we seek solace in the symphony of nature, the dissonance of noise serves as a reminder of the delicate balance

between the sounds that uplift us and the clatter that challenges our auditory harmony. What one person might consider soothing might be noise to another—a testament to the subjectivity of the concept.

Figure 1.3, various common noise sources are depicted along with their typical frequency content and placement on a sound level scale. Decibels are used as a measurement unit to assess the power of sound sources. Human ears, however, respond differently at various frequencies.

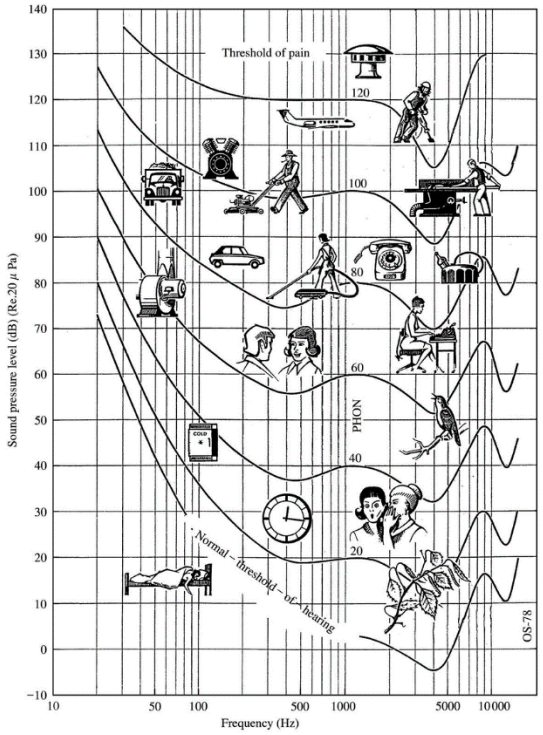

Figure 1.3: Regular noise sources' typical sound pressure levels and frequency ranges.[5]

Acoustics is the multidisciplinary study of sound, encompassing fields such as physics, engineering, psychology, and architecture. It seeks to understand the behavior of sound waves, their propagation, and interactions with various mediums. Simply said, acoustics is the study of the generation, reception, and transmission of sound. Greek is the language's

original home of the word acoustic. Its root words are akoustikos, which means "of or for hearing, ready to hear," and akoustos, which means "heard, audible." This also comes from the verb akouo, which means "I hear." Acoustics encompasses the design of sound barriers, the optimization of building materials for noise reduction, and the creation of acoustic treatments that transform noisy spaces into serene retreats.

In conclusion, Sound, noise, and acoustics are integral facets of human existence, shaping how we perceive and interact with the world. By comprehending the properties of sound, the detrimental effects of noise, and the science of acoustics, we empower ourselves to create harmonious environments that enhance our well-being and preserve the delicate balance of our sonic world. From the awe-inspiring symphonies of nature to the controlled acoustics of performance spaces, the interplay of sound enriches our lives in myriad ways, reminding us of the profound connection between science, art, and the human experience.

The critical factor in quantifying noise is the physical quantity known as sound pressure, which represents the incremental pressure fluctuations caused by the oscillation of waves in the air above and below the ambient pressure. Even within the boundaries of ear pain, the sound pressure is quite tiny in comparison to the static air pressure. For instance, sound pressure comprises a series of rapidly alternating positive and negative values that vary over time. These are commonly assessed using a device that provides a statistical representation, such as the root mean square (rms) sound pressure, which averages out the instantaneous fluctuations. This is given by:[6]

$$p_{rms} = \sqrt{\frac{1}{T}\int_0^T p^2(l)dt} \ N/m^2 \qquad (1.1)$$

where T is a time period sufficient to allow the statistical process to accumulate. The root mean square (rms) value of pressure typically holds significance, leading to the omission of the rms index from the pressure symbol. The representation of sound pressure is not expressed in absolute terms; instead, it is referenced to a specific quantity, typically the pressure at 1 kHz corresponding to the average audibility limit of a typical healthy individual. Thus, the sound pressure level (SPL) is defined as:

$$SPL = 20 \times \log_{10} \left| \frac{p}{p_0} \right| \tag{1.2}$$

SPL is a measure of how loud a sound is mathematically, instead of calculating amplitude directly in acoustics, the sound pressure level is defined as where p is the pressure of sound and p_0 is the reference pressure 2×10^{-5} Pa.

Sound propagates in waveform, which is not merely a sine or cosine wave. From a different viewpoint, it can be described more generally in mathematical terms as a wave and expressed as [7]

$$w(x,t) = g(x - ct) + h(x + ct) \tag{1.3}$$

Where $g(*)$ and $h(*)$ generally shows the wave form. It's important to note that waveforms g and h effectively illustrate patterns across both space and time. These also propagate through space and time via the $x + ct$ or $x - ct$ connection. For deeper understanding of wave propagation, see the Figure 1.4. This figure illustrates the evolution of the function "g" along the x-axis over time. We observe that the "g" function moves a distance $'ct'$ through space. Importantly, we can now visualize the wave represented by the "g" function in space, specifically noting its temporal changes relative to its spatial variations along the x-

coordinate. The result is obtained by rewriting the wave "g" function in terms of time as shown in equation 1.4.

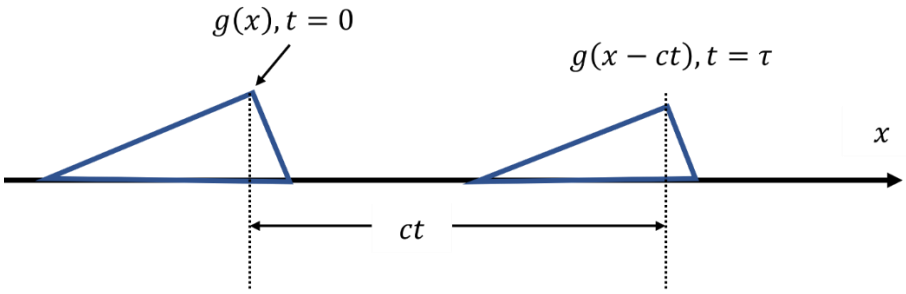

Figure 1.4: The wave travels in a positive (+) x direction; g expresses the wave's shape, c determines the wave's speed, and t and x specify the time and coordinate.

$$g(x - ct) = g(-c\left(t - \frac{x}{c}\right)) \tag{1.4}$$

According to equation 1.4, when a wave moves through time, it can be perceived as a right-moving wave in space. Equation 1.4 can be used to define the sine wave, a particular wave. The sine wave propagating to the right is stated as

$$w(x,t) = Y \sin\left(k(x - ct) + \varphi\right) \tag{1.5}$$

where k converts the units of the independent variable of the sine function to radians; Y denotes the amplitude, $\emptyset$ is an arbitrary phase, and x and ct are length units. These values rely on the sine wave's beginning value of amplitude.

Equation (1.5) can be rewrite as

$$w(x,t) = Y \sin\big((kx - kct) + \emptyset\big) = Y \sin\left(kx - \omega t + \varphi\right) \tag{1.6}$$

where $kc = \omega$ and it is measured in rad/sec because the sine function's independent variable must be expressed in radians. It connects the variable representing the change in space(x), k, with the one representing the change in time(t), ω. That is,

$$k = \frac{\omega}{c} = \frac{2\pi f}{c} = 2\pi \frac{1}{cT} = \frac{2\pi}{\lambda} \tag{1.7}$$

where k is the number of waves in one unit of length. This is referred to as a wave number or propagation constant. We also call this "dispersion relation "which shows space and time relation. In contrast to generic waves, those with a cosine or sin form is regarded as unique types. Only in these unique cases does the dispersion relation apply. Nevertheless, we are aware that any wave can be generated or expressed through a Fourier integral or series by superimposing sine and cosine waves. Therefore, comprehending single harmonic waves is both the foundation for further study and the place where we must always start.

One-dimensional wave is shown in equation (1.3), now let's understand the physical meaning by calculating the derivative of this equation with respect to time and space.[7]

$$\frac{\partial y}{\partial x} = g' + h' \tag{1.8}$$

where $'$ shows the derivative of each function

$$\frac{\partial y}{\partial t} = -cg' + ch' \tag{1.9}$$

Which leads to,

$$\frac{\partial g}{\partial t} = -cg' = -c\frac{\partial g}{\partial x} \tag{1.10}$$

$$\frac{\partial h}{\partial t} = ch' = c\frac{\partial h}{\partial x} \tag{1.11}$$

It is basically stated in equation (1.10) and (1.11), that a wave's rate of change (g) is related to the change in its spatial location by factor "-c". However, wave h's rate of change is related to its change in space by the factor "c" and is propagating in the opposite direction. With respect to space, the g wave moves upward when there is a negative slop and downward when there is a positive slop.

If we differentiate equations (1.10), and (1.11), we get.

$$\frac{\partial^2 g}{\partial t^2} = c^2\frac{\partial^2 g}{\partial x^2} \tag{1.12}$$

$$\frac{\partial^2 h}{\partial t^2} = c^2\frac{\partial^2 h}{\partial x^2} \tag{1.13}$$

This shows that any one-dimensional wave y (x, t) which has left-going and right going wave with respect to the selected coordinate satisfied the partial differential equation.

$$\frac{\partial^2 y}{\partial t^2} = c^2\frac{\partial^2 y}{\partial x^2} \tag{1.14}$$

Equation (14) can be expressed as

$$\frac{\partial^2 y}{\partial x^2} = \frac{1}{c^2}\frac{\partial^2 y}{\partial t^2} \tag{1.15}$$

Equation (1.12) is the one-dimensional wave equation, and it can be extended to third dimensional wave as y (x, y, z, t)

$$\nabla^2 y = \frac{1}{c^2}\frac{\partial^2 y}{\partial t^2} \tag{1.16}$$

It is possible to theoretically consider any wave as one of the solutions to this equation and the steady-state boundary condition.

The interaction of acoustic waves in a compressible fluid is influenced by three main physical aspects: acoustic pressure, fluid particle velocity, and fluctuating density. These factors are interconnected and do not operate independently. Various laws and equations, such as the linearized Euler equation, the conservation of mass, and the gas state equation, are employed to describe the relationships among them, as illustrated.in the Figure 1.5. The linearized Euler equation effectively demonstrates that a fluid with mass per unit volume will flow with an acceleration of $\frac{\partial u}{\partial t}$,in response to a slight pressure change over a short distance (∂x). According to the conservation of mass equation, a steeper negative velocity gradient in space results from a faster rate of temporal compression. According to the equation of state, the features of the medium affect the speed of propagation. We will achieve a faster propagation speed if there is a smaller density change per unit pressure change.

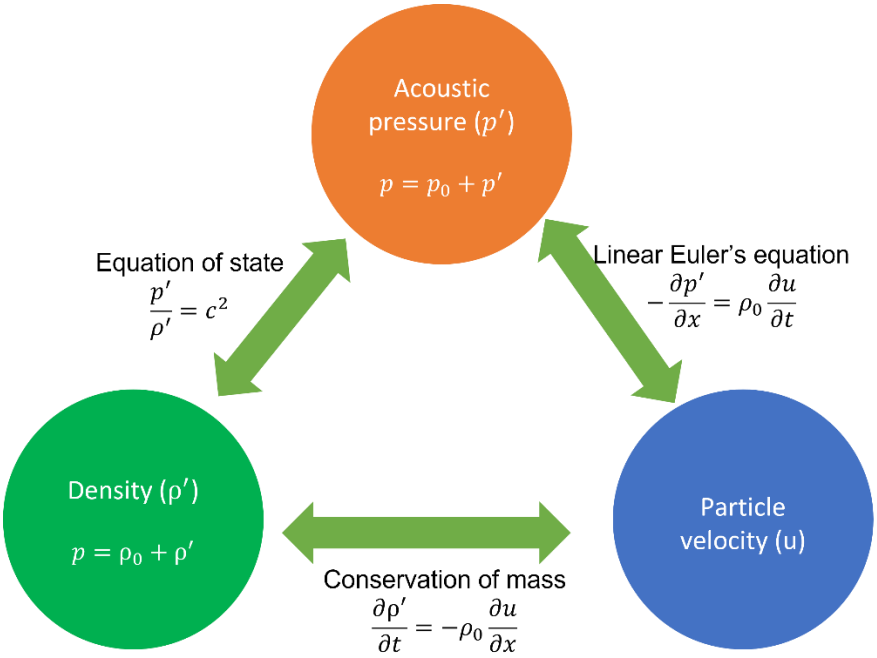

Figure 1.5: Three factors that control the propagation of acoustic waves are represented in a picture. (p_0 and ρ_0 express the mean pressure and static density respectively; p' and ρ' signify, respectively, changing density and acoustic pressure; c represents the sound speed and u is the speed of the fluctuating acoustic medium)

Acoustic Impedance is a valuable quantity in acoustics. It gauges how much the motion brought about by pressure being applied to a surface is slowed down. The ratio of pressure to velocity is an obvious choice for this measure because frictional forces are often proportional to velocity:[6]

$$Z = \frac{p}{u} \tag{1.17}$$

If the reflection coefficient R is defined:

$$R = \frac{p^-}{p^+} = \frac{Z - \rho_0 C}{Z + \rho_0 C} \tag{1.18}$$

Sound **absorption coefficient** α is defined:

$$\alpha = 1 - |R|^2 \tag{1.19}$$

The **impedance** with no reflection (of a plane wave) is thus:

$$Z = \rho_0 C \tag{1.20}$$

Reflection and transmission due to impedance mismatch

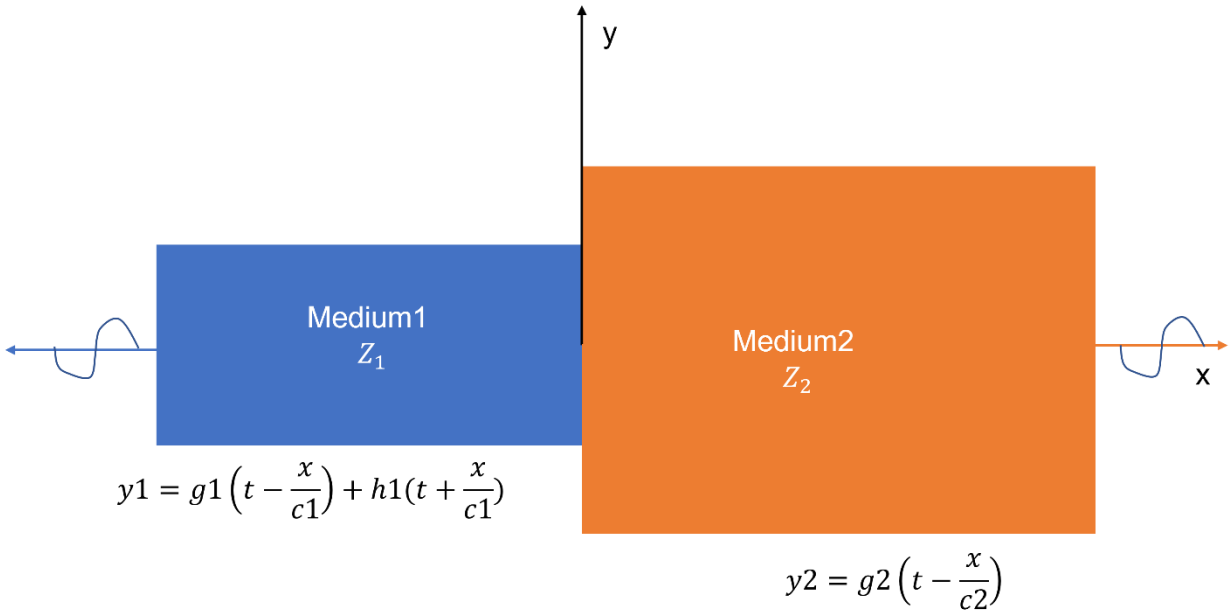

Figure 1.6: Wave in two mediums of different impedance.

We begin by examining the one-dimensional wave equation to explore how waves propagate and interact with their medium and boundaries. In a condensed and straightforward manner, this will enable us to comprehend more complex general waves. The many different one-dimensional waves that could exist are represented by waves moving along a medium.

Let's first look at waves moving across two different media, as shown in Figure 1.6. A wave moves in the right direction, as seen in this diagram. Let's refer to this incident wave, which travels in the positive x direction, as $g1$ This wave appears to be propagating in the positive time axis when observed with regard to time.

Assume there is a thinner medium between an incident wave ($g1$)and a reflected wave ($h1$)(see Figure 1.6). Assume additionally that the thicker material is just a conduit for the transmitted wave $g2$. At this stage, we're trying to figure out how the transmitted wave $g2$ and the incident wave $g1$ are related to reflected wave $h1$.

The incoming wave, reflected wave, and transmitted wave can be expressed as:

$$p_i = p_i \, e^{-i\omega\left(t-\frac{x}{c1}\right)} \tag{1.21}$$

$$p_r = p_r \, e^{-i\omega\left(t+\frac{x}{c1}\right)} \tag{1.22}$$

$$p_t = p_t \, e^{-i\omega\left(t-\frac{x}{c2}\right)} \tag{1.23}$$

The first thing we realise is that the mid-surface (x=0) must have constant pressure. Additionally, a fluid particle's velocity must also be continuous. In other words, the incident and reflected waves combined resultant velocity at x = 0 must be equal to the transmitted wave's velocity at x = 0. This is a straightforward result of the assumption that the medium is continuous; velocity is thus continuous.

Initially, the pressure continuity at x=0 can be expressed as:

$$p_i + p_r = p_t \tag{1.24}$$

The velocity continuity can be written as:

$$U_i - U_r = U_t \tag{1.25}$$

Where P and U are the complex amplitude of pressure and velocity.

Now the incident wave (p_i), reflected wave (p_r), and transmitted wave (p_t) can therefore written as

$$p_i(x,t) = P_i e^{-i(\omega t - k_1 x)} \tag{1.26}$$

$$p_r(x,t) = P_r e^{-i(\omega t + k_1 x)} \tag{1.27}$$

$$p_t(x,t) = P_t e^{-i(\omega t - k_2 x)} \tag{1.28}$$

Where k_1 and k_2 are defined as

$$k_1 = \frac{\omega}{c1}, k_2 = \frac{\omega}{c2} \tag{1.29}$$

Where $c1$ and $c2$ are the speed of sound in medium 1 and 2.

For plane wave we can rewrite equation (1.25) as

$$\frac{p_i}{Z1} - \frac{p_r}{Z1} = \frac{p_t}{Z2} \tag{1.30}$$

In which we use the relation $Z = P/U$

The ratio of $p_r \; to \; p_i$ that is, the reflection coefficient R and $p_t \; to \; p_i$, the transmitted wave can be obtained from equation (1.24) and (1.30),[7]

$$\frac{p_r}{p_i} = R = \frac{Z2 - Z1}{Z2 + Z1} \tag{1.31}$$

$$\frac{p_t}{p_i} = T = \frac{2 \times Z2}{Z2 + Z1} \tag{1.32}$$

We can explore these equations by taking a look at extreme situations, like when Z1 << Z2 or Z1 >> Z2. Figure 1.7 illustrates how waves move when they encounter a change in impedance. It's evident that the characteristics of the transmitted and reflected waves are entirely determined by the impedance mismatch, which, in the current scenario, arises from a discontinuity in mass density. The first example demonstrates how the reflected wave is entirely inverted. To put it another way, there is a phase difference of π ,[7]

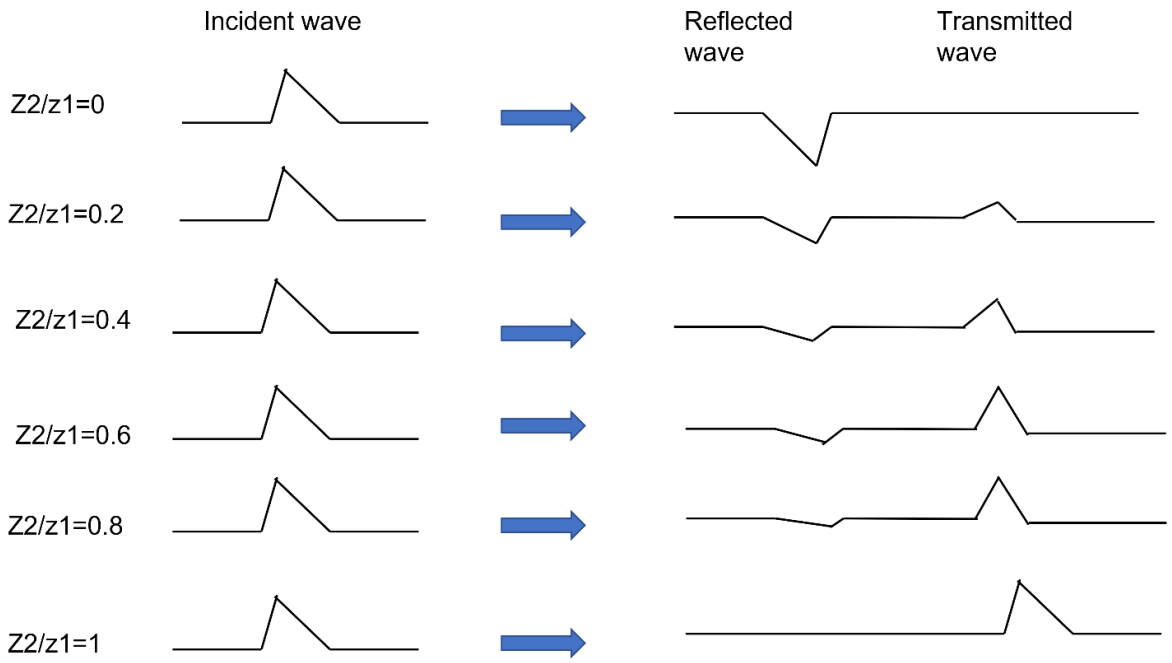

Figure 1.7: Incident, reflected and transmitted waves on a medium when Z2/Z1 less than or equal to 1.

If Z2 is significantly larger than Z1. In this instance, Equation (1.31) approaches -1, indicating that the incident wave's amplitude and phase have been reversed in the reflected wave. The transmitted wave will be very tiny as Z2 exceeds Z1, and Equation (1.32) will be very close to zero. However, the phases of the reflected waves are not reversed from the sixth example (z2/z1=1) in Figure 1.7 when there is a perfect impedance match.

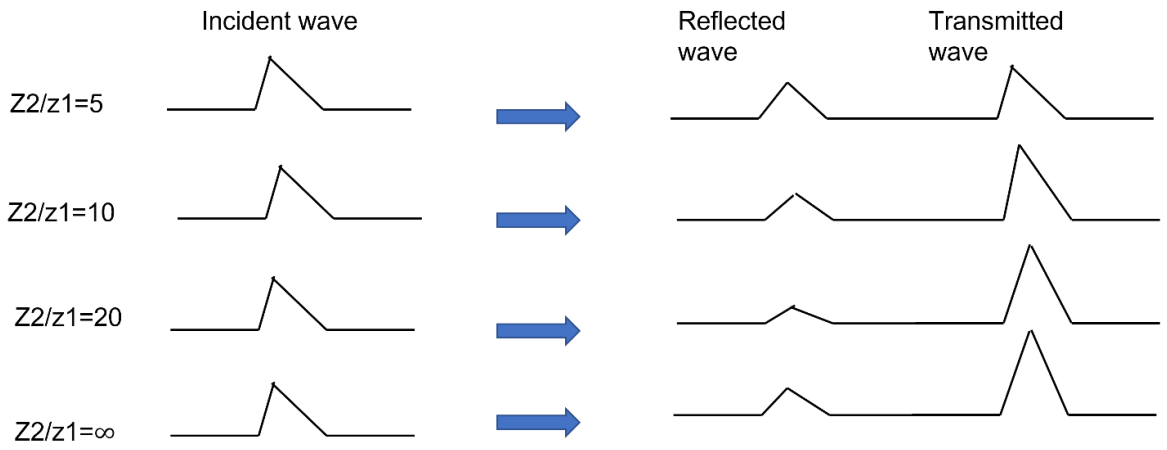

Figure 1.8: Incident, reflected and transmitted waves on a medium when Z2/Z1 greater than 1.

Equation (1.31) states that the incident wave will be entirely reflected without changing phase if Z1 significantly exceeds Z2 (Z1 >> Z2). Although Equation (1.32) shows that the transmitted wave's amplitude is double that of the incident wave, this is highly improbable in practice. The amount of power communicated can be used to explain this paradox, which is somewhat puzzling. Even if the transmitted wave amplitude is twice that of the incident wave, it is clear that the power is zero because the transmitted velocity is zero.

Dispersion Relation: Acoustic dispersion is the process of a sound wave breaking up into its individual frequencies when it travels through a material. The sound wave's phase velocity is considered as a function of frequency. Therefore, the variation in phase velocities as the radiated waves traverse a specific material is utilized to determine the dispersion of component frequencies. The dispersion relation explains how the relationship between a wave's frequency and sound speed fluctuates. Since the wave frequency and wavenumber scale linearly in many simple vibrating systems seen in nature, in that case the sound speed

is constant at all frequencies**.** The dispersion relation can represent by the following equation. [6]

$$\omega(k) = ck \tag{1.33}$$

In the equation, "*k*" represents the wavenumber, $\omega(k)$ denote the angular frequency, and "c" stand for the speed of sound. In a non-dispersive medium like air, all frequencies of a sound wave reach the listener simultaneously. However, in dispersive mediums, such as the classic example of light passing through a prism, the speed of sound varies with frequency, causing each frequency to reach the listener at different times.

Understanding the dispersion relation, also referred to as the dispersion diagram or band diagram, is crucial in modeling acoustic metamaterials and phononic crystals using wave band theory. In such systems, the dispersion relation not only illustrates a nonlinear relationship between frequency and wavenumber but also reveals specific frequency bands, known as band gaps, where sound energy cannot propagate.

The mass-Law: The mass-law establishes a relationship between a wall's mass and how well airborne sound travels through it. The introduction of acoustic metamaterials is seen to be of particular importance since, unlike conventional materials, they are capable of breaking this law. According to the mass-law, the transmission of a sound wave through a material submerged in a fluid is defined by, [6]

$$\tau \approx \left(\frac{2\rho c}{m''\omega}\right)^2 \tag{1.34}$$

In the equation, ρ represents fluid density, c denotes the speed of sound in the fluid, $m'' = \rho_m h$ is the mass per unit area of the materials, where ρ_m is the material density, h is its thickness and ω stands for the angular frequency of the sound wave. As a result, doubling the mass, density, or thickness of a material, or doubling the frequency of the input sound wave, will halve the sound transmission through a wall. A 6 dB SPL attenuation corresponds to halving the sound transmission.

However, acoustic metamaterials can challenge the mass-law by attenuating sound well beyond 6 dB for a doubling of thickness in specific frequency bands, without the need to increase mass, density, or frequency.

1.2 Noise control technique

An array of tactics is used to lessen the effects of noise. For noise suppression, a variety of methods are employed. The three most common conventional ways, however, are noise isolation, noise absorption, and noise suppression.

Noise isolation: The practice of preventing noise from spreading from one area to another is known as noise isolation. It frequently refers to preventing noise from escaping from its source or spreading to a particular area. Acoustic panels, partitions, and barriers are frequently used as solutions for noise isolation. They can be utilized as office panels, partitions, sound barriers, and other structures. These goods are often heavy when made of traditional materials in order to effectively suppress noise.

Noise absorption: Reduced noise intensity is achieved through noise absorption. It can be utilized in aircraft engine lining, ventilation, exhausts, ceilings, walls, sound absorbers in acoustic rooms to enhance the sound quality, etc. Porous materials like fiberglass, acoustic

foam, and blankets are preferred by traditional designs. Additionally, in tough situations requiring hard surfaces and exposure to high temperatures, microperforated plate (MPP) is widely employed for sound absorption applications. The quarter-wavelength principle, which states that high-performance designs must have a thickness in wavelength scale, is still the major factor affecting how well these designs function. They are ineffective in absorbing at low frequencies as a result.

Noise silencing: Acoustic silencers and liners frequently use the noise-silencing technique to absorb and block exhaust noise. Silencers have a classic design that includes a number of chambers, necks, and perforation separations to create resonances at appropriate frequency ranges. Resonant frequencies allow for the blocking or absorption of noise. The majority of modern silencers, however, have winding structures that prevent optimal airflow and optical transparency.

1.3 Mechanism of Acoustic Control

In today's contemporary environment, where noise control has become increasingly crucial, this section explores the diverse strategies employed within the noise control sector. The decibel scale serves as the measure for noise, with sound considered reasonable if it falls below 85dB. However, when sound levels exceed this threshold, they can pose significant health risks. In such cases, personal ear protection or noise barriers are essential. It's imperative to develop techniques for managing and reducing noise when it surpasses safe limits.

These approaches are broadly categorized into two mechanisms: active control and passive control. Active control utilizes electro-acoustical methods, employing either anti-phase signals generated by speakers or addressing structural vibrations to mitigate sound. On the

other hand, passive control involves modifying the environment surrounding the source or receiver, utilizing materials designed to absorb, diffuse, or deflect sound.

Both active and passive strategies can be further classified based on the underlying physics employed for noise filtration. The flow chart depicted in Figure 1.9, provides a visual representation of this classification of control mechanisms, simplifying the understanding of the topic.

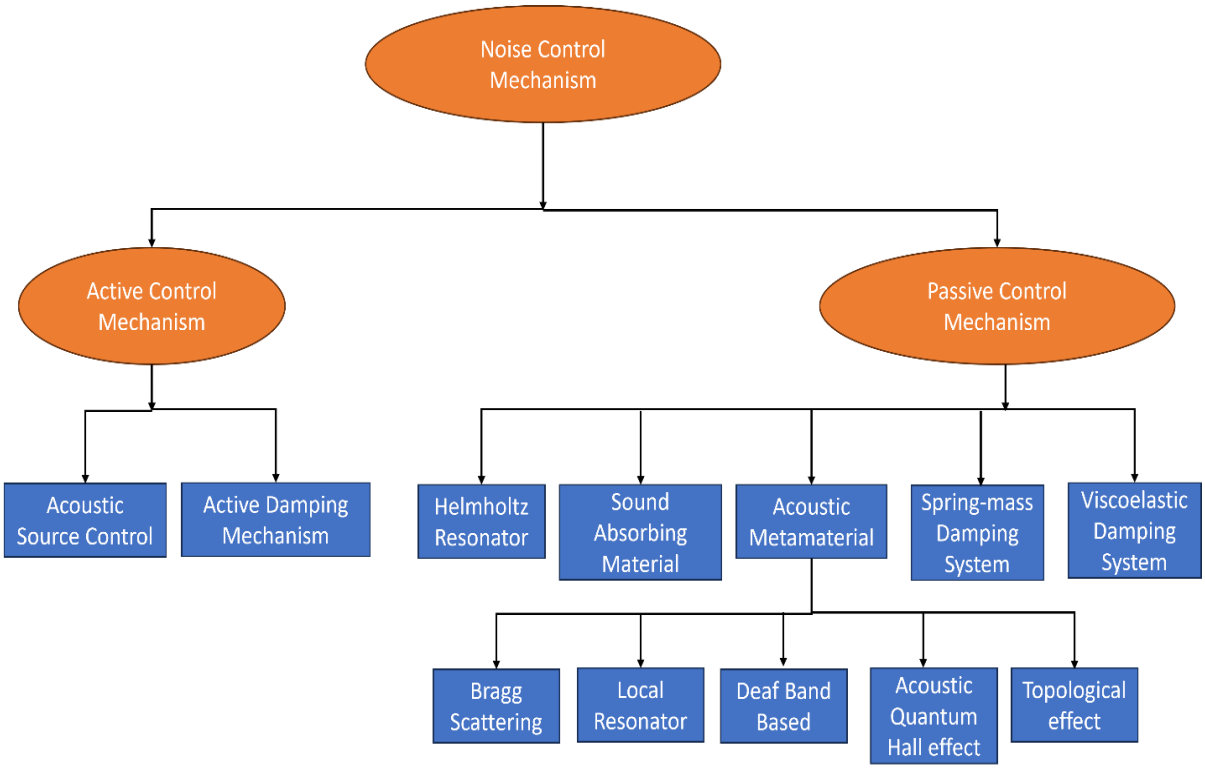

Figure 1.9: Noise control mechanism classification.

1.4 Acoustic metamaterials

The potential to manipulate sound waves in novel ways is what spurs the search for new materials in acoustics. For instance, acoustic metamaterials could replace conventional materials by dampening sound through the use of compact, lightweight structures. They could also be used to control vibrations, bend sound in multiple directions, create acoustic cloaks, and create energy-harvesting devices.

Acoustic metamaterials have made tremendous progress in research labs during the past ten years. However, there has only been a little amount of development from the lab setting to industrial manufacture. Despite this, the sector is expanding quickly, and in the upcoming years, new innovations and practical products are anticipated. The primary uses that have been suggested involving sound management in audio equipment, noise attenuation in the automotive and aerospace industries, acoustic cloaks, acoustic super lenses, and energy harvesting devices.

These two factors, effective mass density (ρ) and bulk modulus (k), are crucial for creating the metamaterials because they affect how acoustic waves propagate inside the designated structure. In general, mass density, which are defined as mass per unit volume and bulk modulus as resistance to applied external compression. Due to their chemical composition and atoms' bonding arrangements, both (ρ) and (k) have positive values in ordinary materials and are susceptible to change. Metamaterials, on the other hand, display a range of effective acoustic parameters, including negative values that cannot be generated with conventional materials.

Acoustic metamaterials can be categorized into four different groups, depending on the positive and negative signs of the acoustic parameters: (1) negative mass density; (2) negative

bulk modulus; (3) double negative parameter s; and (4) near-zero and approaching infinity mass density.

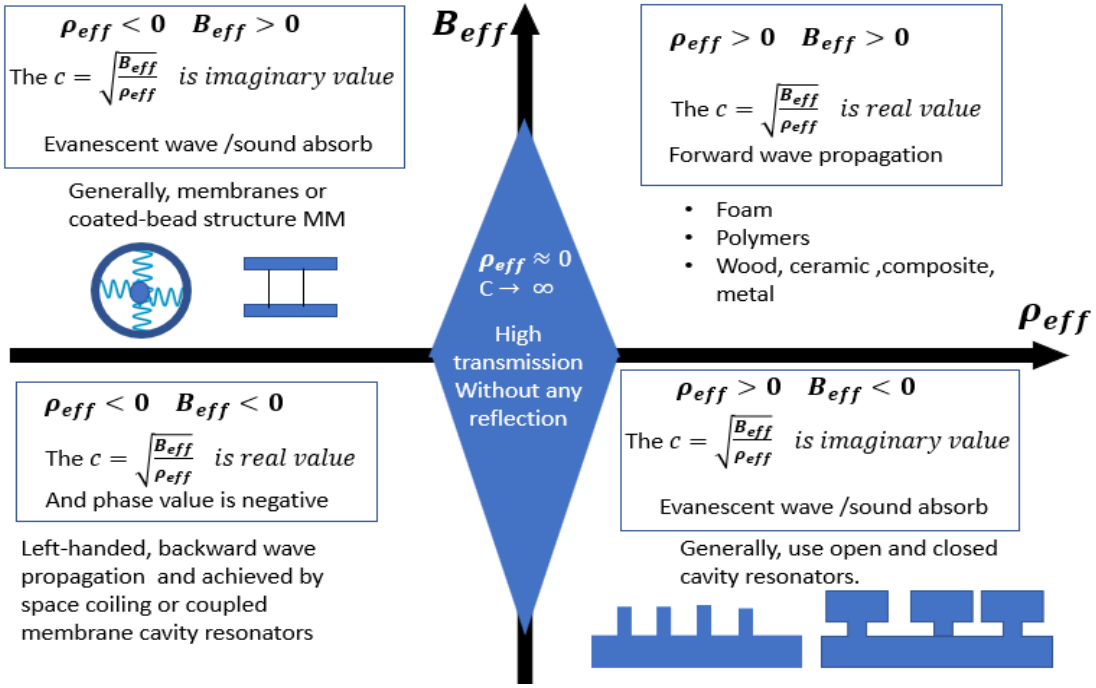

Figure 1.10: Each quadrant in the effective mass density and bulk modulus planning diagram illustrates a particular type of metamaterial and demonstrates how to obtain a negative acoustic parameter.

Any metamaterial's sound speed can be determined using the equation $c = \sqrt{\frac{k}{\rho}}$, where k stands for bulk modulus and ρ for density. If one of the values becomes negative, the speed of sound is revealed to be fictitious, which illustrates the sound wave's decay or absorption by the MM. These types of MM prevent sound waves from being transmitted, causing sound waves to be dampened internally. The speed of sound is real if both acoustic parameters exhibit negative values, but energy and phase velocity are in the opposite direction, i.e.,

negative reflection, and are useful for creating superlences. Figure 1.10, illustrates how AMM are categorized depending on the sign of the mass density and bulk modulus, how they are used, and how to produce this unconventional behavior utilizing acoustic elements.

1.4.1 Effective mass density and bulk modulus

Acoustic metamaterials (AMM) differ from normal materials in that they have an additional degree of freedom that is concealed in their specifically constructed microstructure. The major features of AMM that stand out are its capacity for displaying negative mass density and bulk modulus, which means that medium particles accelerate in the opposite direction of the external force applied and medium particles expand upon compression. Scientists use unit cells that are smaller than the phonos wavelength to obtain these peculiar features.

Dynamic Density

The spring mass system can be used to comprehend the idea of a negative behavior of mass density and bulk modulus as shown in Figure 1.11(a). Theoretically explained by using the straightforward spring mass system.[8]

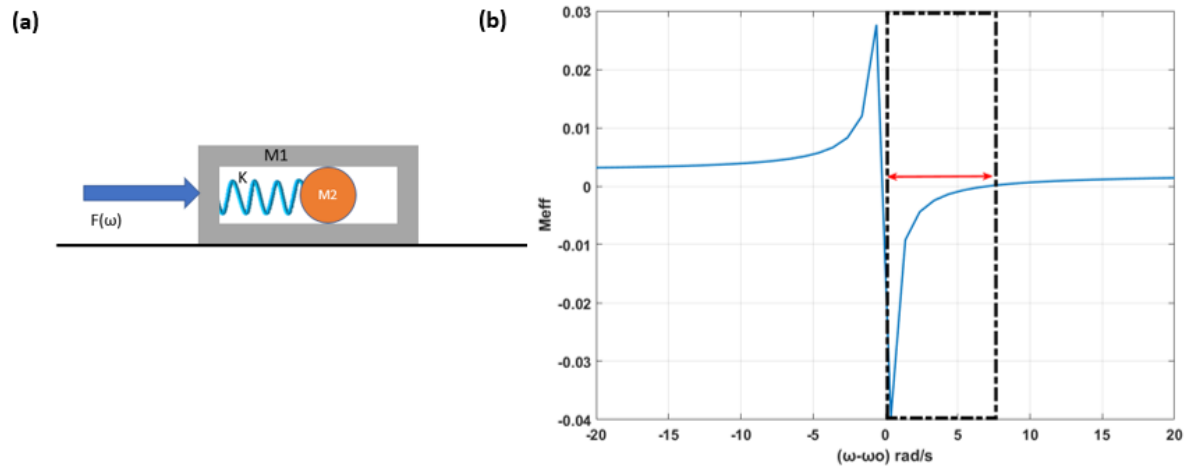

Figure 1.11:(a) Arrangements of simple spring-mass system (b) Effective mass response as a function of angular frequency with respect to frequency difference. (M1=0.002kg, M2=0.001kg, k=1)

The entire spring mass system is depicted in Figure 1.11(a), together with the hidden degree of freedom that is symbolized by a smaller spring mass system. Assuming that there is no friction between the masses and an external force, we may use Newton's second law of motion to explain the motion as follows.

$$M1\ddot{x1} - K(x2 - x1) = F(\omega)$$
$$M2\ddot{x2} - K(x2 - x1) = 0 \quad (1.35)$$

where x1 and x2 are displacement of M1 and M2, solving these differential equations for the applied force.

$$F(\omega) = \left(M1 + \frac{K}{{\omega_0}^2 - \omega^2}\right)\ddot{x1} \quad (1.36)$$

$$F(\omega) = M_{eff}\ddot{x1} \tag{1.37}$$

When the driving frequency crosses the resonance of the concealed mass, which is represented by the local resonance $\omega_0 = \sqrt{K/M2}$, Figure 1.11(b), displays the negative effective characteristics that are emphasized in the box. When using the AMM to represent a mass spring system mathematically, we can use equation (37) to drive the effective density as

$$\rho_{eff} = \frac{1}{V}\left(M1 + \frac{K}{{\omega_0}^2 - \omega^2}\right) \tag{1.38}$$

where V is the volume of the system. The effective density shows the negative value in the range of ${\omega_0}^2 < \omega < \sqrt{\frac{K}{M1} + {\omega_0}^2}$ when we consider the two-object system as a homogenous one-object system.

Bulk modulus Generally bulk modulus represents the resistance of the materials to an external pressure, which is given by.

$$\Delta P = -B\frac{\Delta V}{V} \tag{1.39}$$

where, correspondingly, P stands for pressure change, $\frac{\Delta V}{V}$ for volume strain, and B for bulk modulus. A straightforward Helmholtz resonator, which typically consists of a big cavity coupled to a small neck as illustrated in Figure 1.12(a), can be used to illustrate the negative bulk modulus notion. According to Fang et al.,[9] the effective bulk modulus is expressed.

$${B_{eff}}^{-1} = {B_0}^{-1}\left[1 - \frac{F{\omega_0}^2}{\omega^2 - {\omega_0}^2 + i\mu\omega}\right] \tag{1.40}$$

where ω_0 is the resonant resonance frequency, F is the geometric factor, and is the dissipation loss in the resonating Helmholtz resonators. Once more, we can infer that the effective bulk modulus turns negative close to the resonance frequency. Near the resonance frequency, the cavity begins to expand as a result of external resonant pressures, but the cavity contracts as a result of external compressive force, producing a positive bulk modulus.

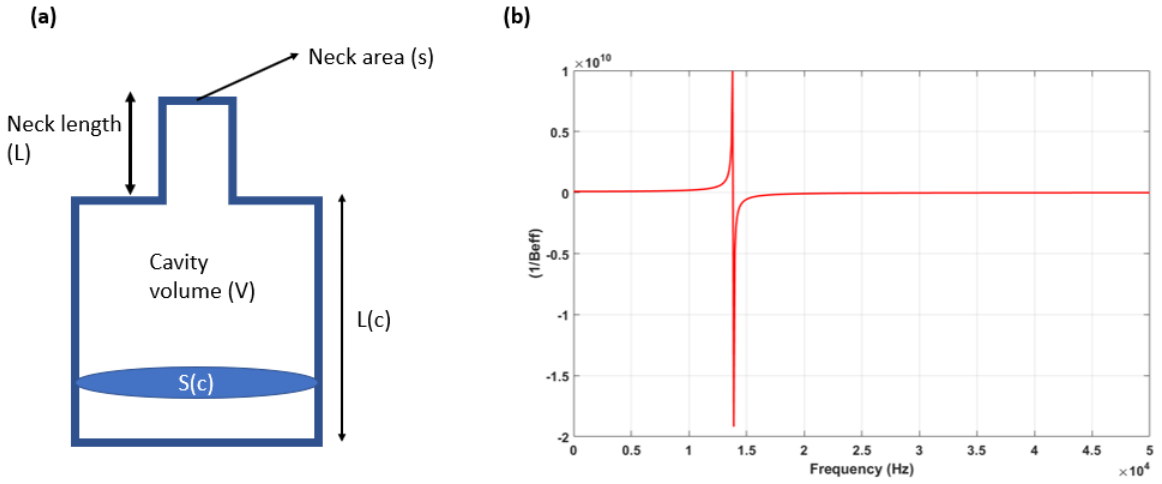

Figure 1.12: (a) Simple Helmholtz resonators system. (b) Effective bulk modulus of rigid Helmholtz resonator.

To prove this concept, we use a Helmholtz resonators (HR) as shown in Figure 1.12 (a) having dimension of neck area(s)=16.63 mm^2 ,L=3mm,V=199.45 mm^3, L(c)=7mm and S(c) =32.17 mm^2 . The natural frequency of HR can be calculated with the following general equation.

$$f = \frac{c}{2\pi}\sqrt{\frac{s}{VL}} \tag{1.41}$$

Where L is the effective length of the neck, V is the cavity volume, c is the speed of sound, s is the cross section of neck. The resonance frequency of the proposed HR is calculated from

equation (41), and it came around 1.386×10^4 Hz. The negative bulk modulus as shown in Figure 1.12(b) around the resonance frequency.

Noise reduction is one of the most popular uses for acoustic materials, and that is also the main goal of the research detailed in this thesis. The capacity to defy the mass-law and create thin, light materials that can attenuate low frequencies are, of course, the main benefits of using acoustic metamaterials for noise attenuation.

Acoustic metamaterials have either negative dynamic mass density or effective bulk modulus. When these characteristics are negative, sound propagation inside the material ends and noise is filtered out since the speed of sound is only made up of the imaginary portion.

1.4.2 Bragg scattering and local resonance

Two crucial qualities bragg scattering and local resonance of some metamaterials displaying within the design itself. Researchers are interested in learning how to regulate or alter the flow of mechanical energy that manifests as vibrations or, more properly, acoustic waves. In order to create acoustic materials that defy the well accepted mass-density law for sound transmission, local resonance mechanism has been used. For dissipation of acoustic energy inside the metamaterials, researcher uses bragg sctaering and locally resonant structure. Based on these concept many researcher design acoustic metamaterials[10]–[13]

Bragg scattering

We know that the wave in space can be seen as the wave propagation in time and it can be described by a cosine wave as expressed in

$$y(x,t) = Y\cos(\omega t - kx + \varphi) \tag{1.42}$$

where $k = {}^{\omega}/_{c} = {}^{2\pi}/_{\lambda}$ is the wave number and $\omega = {}^{2\pi}/_{T}$ is the angular frequency. φ is a phase.

The capacity of waves to interfere is one of their most significant characteristics and destructive and constructive interface depend upon the phase.

Destructive interference when $\Delta\varphi = \pi$ and constructive interference happen when $\Delta\varphi = 0$

Let us now consider a wave that strike with the scatterer. When wave is strike with the scatterer, the scatterer get excited and some of the energy get absorbed in it and some of the energy get radiated in the space as shown in Figure 1.13 (a).

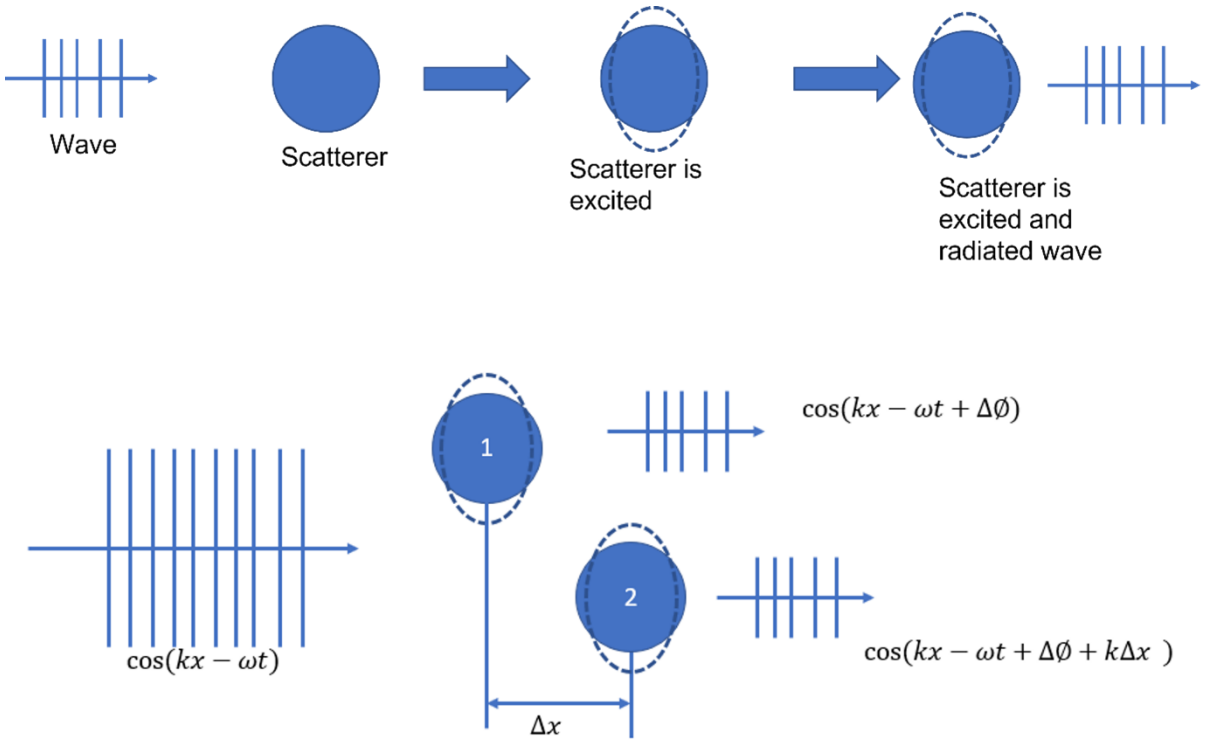

Figure 1.13: (a) Scattering phenomenon when wave is strike against it. (b) Bragg phenomenon.

Let's now consider two scatterers presented in the way of travelling wave. The distance between these scatterers are Δx as shown in Figure 1.13 (b). The time lag, i.e. the phase difference $\Delta\varphi$ between the incident wave and the radiated wave by scatterer 1 and $\Delta\varphi + k\Delta x$ is the phase difference between incident wave and the scatterer 2.

We can observe from the Figure 1.13 (b) is that.

when $k\Delta x=\pi$ the scattered wave interferes destructively

$\Delta x = {}^{\pi}/_{k} = {}^{\lambda}/_{2}$, lead to strong destructive effects

If we deal with periodic arrays of scatterers, this phenomenon is known as "Bragg scattering." The fundamental principle of phononic crystals is Bragg scattering. At frequencies where the Bragg condition holds true, it is not difficult to envisage that periodic arrays with a typical length-scale ΔL can have tremendous effects on wave propagation.

$$\Delta L = {}^{\lambda}/_{2} \tag{1.43}$$

In particular, a condition where waves cannot travel at the particular frequencies where the Bragg condition is satisfied. This is known as a band gap.

Local resonance

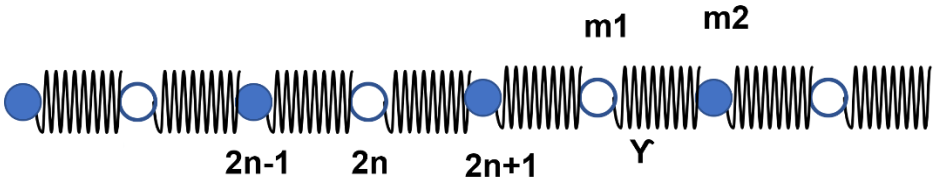

Figure 1.14: The one-dimensional diatomic harmonic crystal is shown schematically. Odd atoms have a mass of m2, while even atoms have a mass of m1. The springs' force constant

is γ. The crystal's periodicity is 2a, where “a” is the space between the mass while they are at rest.

The infinitely long chain of masses, m, in the one-dimensional (1-D) monoatomic harmonic crystal interact with their nearest neighbors via harmonic springs with a spring constant, γ . The spacing between the masses while they are at rest is known as “a”. The model system is shown in Figure 1.14.

Understanding the coupling of two oscillators is necessary to comprehend the idea of local resonances. Let consider that the displacement of oscillators 2n is x(t) and 2n+1 have the displacement y(t) and angular velocity of oscillation is ω for both the oscillators.

By using newton’s law of acceleration, we can write the equation as

$$\ddot{x}\ (\mathrm{t}) = -\omega^2 x(t) + \gamma^2 y(t) \tag{1.44}$$

$$\ddot{y}\ (\mathrm{t}) = -\omega^2 y(t) + \gamma^2 x(t) \tag{1.45}$$

Let’s assume that the movement of the oscillators are.

$$\begin{pmatrix} x(t) \\ y(t) \end{pmatrix} = \begin{pmatrix} x_0 \\ y_0 \end{pmatrix} e^{i\omega t} \tag{1.46}$$

We have to find the combined solutions.

So

$$\begin{pmatrix} x(t) \\ y(t) \end{pmatrix} = \begin{pmatrix} x_0 \\ y_0 \end{pmatrix} e^{i\omega_c t} \tag{1.47}$$

Solve the equation (1.44), (1.45), (1.46) and (1.47) and do some algebraic manipulations, we got the following expression.

$$-{\omega_c}^2 \begin{pmatrix} x_0 \\ y_0 \end{pmatrix} = \begin{pmatrix} -\omega^2 & \gamma^2 \\ \gamma^2 & -\omega^2 \end{pmatrix} \begin{pmatrix} x_0 \\ y_0 \end{pmatrix} \tag{1.48}$$

This is the eigenvalue problem of ω_c. And after solving the equation (1.46), we got.

$$\omega_c \pm = \sqrt{\omega^2 \pm \gamma^2} \tag{1.49}$$

We can easily generalize that the two coupled oscillators have different frequency instead of single frequency as discussed above.

Let assume that the angular frequency of oscillator 1, is ω_1 and second osscilator is ω_2 ,finally got the solution[14],

$$\omega_c \pm = \sqrt{\left(\frac{\omega_1^2 + \omega_2^2}{2}\right)^2 \pm \left[\left(\frac{\omega_1^2 - \omega_2^2}{2}\right)^2 + \gamma^2\right]^2} \tag{1.50}$$

from the equation (1.50), we can conclude that, the strongest coupling effect occurs when two oscillators are degenerate or have the same frequency. The main effect is due to coupling i.e. γ and play important role to split the frequency of two oscillator system. The wave and the local oscillator's degenerate system will be divided by the coupling. Where the two frequencies overlap, this effect is strongest. A frequency window is opening where no waves may travel, just like in the Bragg scattering phenomenon. But this time, the frequency is determined by the frequency of the local oscillator rather than the spacing of the periodic array.

1.5 3D Printing

Additive manufacturing, sometimes referred to as three-dimensional printing, is a technique for building up physical objects layer by layer. The item is initially created in STL format using Computer-Aided Design (CAD) software or by three-dimensionally scanning an existing shape. The STL file is divided by the three-dimensional printing software into layers of a specific thickness, which is determined by the highest resolution of the printer. The object can then be constructed layer by layer using a variety of three-dimensional printing techniques. The three methods that are most frequently used are melting powders, extruding heated materials from a nozzle, and hardening liquid polymers. The printed item is then polished and cleaned. In the past ten years, three-dimensional printing has gained popularity as a quick prototyping technique in both industry and academia. The use of additive manufacturing in finished goods is beginning to emerge as these methods are improved.

The use of three-dimensional printers could be extremely advantageous for acoustic metamaterials. Numerous models have been published in the field of acoustic metamaterials, but in comparison, few labs have made samples, and even fewer have created fully functional products. The difficulty of manufacturing several identical unit cells could be the cause of the paucity of experimental research.

1.6 Impedance tube measurements

The most popular method for calculating the acoustic absorption coefficient of material samples is the impedance tube. A sound source is located at one end of the tube, while a test sample is located at the other. The measurement of absorption is based on the analysis of the interaction between the incident sound wave's acoustic pressure and the plane wave's

reflected sound wave at the positions of the microphones. An impedance tube, sometimes referred to as a standing wave apparatus or standing wave tube, is a tool frequently used to gauge how well acoustic materials absorb sound. One can measure the absorption and reflection coefficients as well as the usually incident acoustic impedance using a standing wave tube and two microphones as shown in Figure 1.15. It is also possible to obtain transmission coefficients using four microphones.

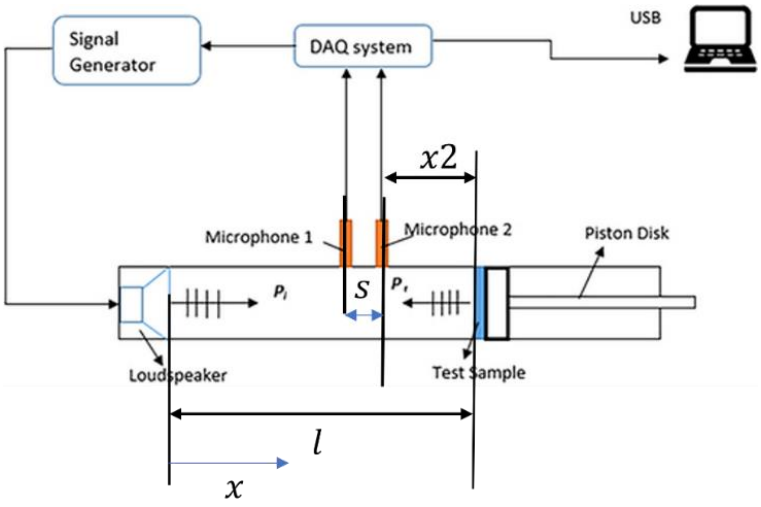

Figure 1.15:Diagram of an impedance tube featuring two microphones.

The incident wave's acoustic pressure,$p_i(x)$, and the sample's reflected wave, $p_r(x)$ make up the wave field inside the tube $p(x)$.

$$p(x) = p_i(x) + p_r(x) = Ae^{-jkx} + Be^{jkx} \quad (1.51)$$

where A and B are the acoustic pressure amplitudes of the incident and reflected waves, respectively.

The sound pressure amplitudes of the incident and reflected waves are compared to determine the reflection factor, which is equal to the ratio r = B / A. In terms of the likelihood of a wave phase shift, the reflection factor r is seen as a complex number. While it holds true that the

acoustic absorption coefficient and the reflection factor r (acoustic reflection coefficient) are dimensionless quantities with values between 0 and 1, and the absorption coefficient can be calculated as

$$\alpha = 1 - |r|^2 \tag{1.52}$$

The acoustic absorption coefficient α= 1 (r = 0) is the scenario where the material completely absorbs the energy that is incident. For sound absorption, materials with a porous or fibrous structure are advised. The acoustic absorption coefficient α = 0 (r = 1) occurs if the material perfectly reflects all incident sound waves from the surface.

In order to determine the reflection factor:

$$r = r_r + jr_i = \frac{H_{12} - e^{-jkS}}{e^{jks} - H_{12}} e^{2jk(S+x2)} \tag{1.53}$$

where S is the distance between microphones, x2 is the separation between the sample and the position 2 microphone, k is the wave number, H_{12} is the transfer function between locations 1 and 2.

The following equation often holds for a complex acoustic transmission function:

$$H_{12} = \frac{p(x_2)}{p(x_1)} = \frac{S_{12}}{S_{11}} = H_r + jH_i \tag{1.54}$$

where H_r is the realm component and H_i is the imaginary component of the transfer function H_{12}, S_{12} is the cross power spectral density of the signal (from microphone 1 and 2) and $S_{11}$is the power auto-spectral density of the signal (from microphone 1)

The ASTM E1050-12 Standard suggests using the following equation to compute the transfer function in the event that white noise is used to trigger acoustic waves in the tube:

$$H_{12} = \frac{S_{22}}{S_{21}} = H_r + jH_i \tag{1.55}$$

where S_{22} is the power auto-spectral density of the signal (from microphone 2), S_{21} is the cross power spectral density of the signal (from microphone 2 and 1)

put the equation (1.55) or (1.54) in equation (1.53) and get the reflection factor. Once the reflection factor calculated, from equation (1.52), absorption coefficient of the sample.

1.7 Finite element modelling method

It is common to rely on mathematical and analytical models, as in the case of the transfer matrix described in the previous section. When analyzing the acoustic behaviors of systems based on well-known acoustic systems, such as musical instruments, pipes, and Helmholtz resonators, or of systems based on simple geometrical objects, like circles and rectangles. By connecting Newton's laws of motion to the principles of energy conservation, thermodynamics, and other physics that characterize it, the analytical approach models the physics of the acoustic systems under test and derives the equation of motion of such an object. However, when the system under examination is characterized by a complicated geometry, various boundary conditions, or many materials, analytical models and the related differential equations can become highly challenging to solve or rely on oversimplified assumptions. Finite Element Modelling is a substitute for analytical models (FEM). FEM techniques reduce complicated geometries into basic shapes like triangle, quadrilateral, or tetrahedral parts using meshes. Depending on the parameters of the application or physics domain, a number of degrees of freedom are assigned to the nodes at the intersection of meshes or element vertices. The next step is to create and solve a set of differential equations at each node. The user can easily create or import a CAD design, select one or more domains

(such as acoustics, structural mechanics, heat transfer, or optics), set material parameters and boundary conditions manually or by choosing predefined models and materials using software ANSYS acoustic module,[15] which was used for research throughout this dissertation. The user can then choose an analysis type and a mesh, and the package's ANSYS Acoustic module can be used to analyze the data. When employing FEM methods, significant trade-off considerations must be made because the choice of mesh resolution impacts the computation power and accuracy of results.

1.8 Acoustic Circuits

It is possible to draw a direct comparison between electrical circuits and how sound travels through pipes or other enclosed spaces. A lumped-parameter model is appropriate when the dimensions of the region in which the sound propagates are significantly less than the wavelength. Importantly, the phase is essentially constant throughout the system.

1.8.1 Acoustic impedance of an open and closed pipe

Assume that the tube is hollow, cylinder-shaped, open at one end, and closed at the other end by impedance Z_f.The location of the tube's open end is chosen as the coordinate system's origin. We'll presume that the tube's diameter is modest enough for the waves to travel down it with planar wave fronts in a tube. This is only true if the ratio of the sound wave's wavelength to the tube's diameter is more than roughly 6.

Let's assume that the initial travelling wave inside the pipe in the positive "x" direction is P_i, when the wave propagates at the point $x = l$, a reflected wave P_r, travelling in the negative direction of "x". the corresponding particle velocity can be written as

$$v_i = V_i\, e^{i(\omega t - kx)} \tag{1.56}$$

$$v_r = V_r\, e^{i(\omega t + kx)} \tag{1.57}$$

Where $V_i = {}^{P_i}/_{\rho_0 c_0}$, $V_r = {}^{P_r}/_{\rho_0 c_0}$

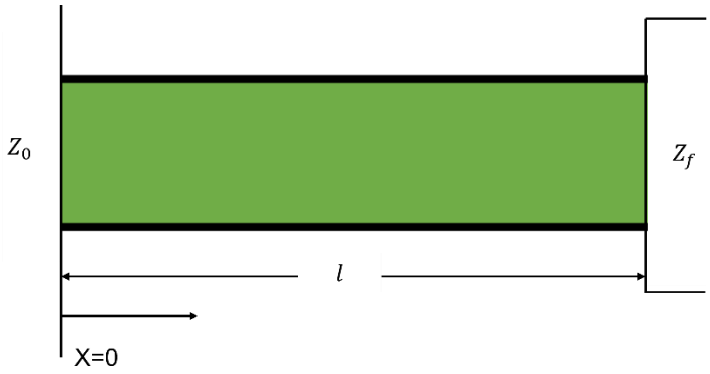

Figure 1.16: A tube with terminated with acoustic impedance Z_f

At any one moment, the tube's overall pressure is.

$$P = P_i + P_r \tag{1.58}$$

The total particle velocity is

$$V = v_i + v_r = {}^{P_i}/_{\rho_0 c_0} + {}^{P_r}/_{\rho_0 c_0} \tag{1.59}$$

Therefore, the basic formulation for the acoustic impedance that accounts for the reflected wave is.

$$Z_A = \frac{P}{Sv} = \frac{\rho_0 c_0}{S}\frac{p_i e^{-ikl} + p_r e^{ikl}}{p_i e^{-ikl} - p_r e^{ikl}} \tag{1.60}$$

So, we know the impedance at x=0, l as

$$Z_{A0} = \frac{\rho_0 c_0}{S}\frac{p_i+p_r}{p_i-p_r}=Z_0 \tag{1.61}$$

$$Z_{Al} = \frac{\rho_0 c_0}{S}\frac{p_i e^{-ikl}+p_r e^{ikl}}{p_i e^{-ikl}-p_r e^{ikl}}=Z_f \tag{1.62}$$

Combined the equation (1.61) and (1.62), we can express the impedance of the open-end x=0, as a function of the impedance Z_f

$$Z_{A0} = \frac{\rho_0 c_0}{S}\frac{Z_f + i\frac{\rho_0 c_0}{S}\tan(kl)}{\frac{\rho_0 c_0}{S} + iZ_f\tan(kl)} \tag{1.63}$$

Let's consider an air in a tube with length l and area S. Assume the tube is open on both ends and is acoustically stiff. When the tube's dimension is substantially less than the corresponding wavelength, all values are in phase, causing it to move with displacement when an unbalanced force is applied. Because of the open ends, the entire portion moves without experiencing a noticeable compression.

Substitute equation (39) with $Z_{Al} = 0$

Substitute equation (39) with $Z_{Al} = 0$, [16]

$$Z_{A0} = j\frac{\rho_0 c_0}{S}\tan(kl) \tag{1.64}$$

Since l is much smaller than wavelength,$kl = {}^{2\pi l}/_{\lambda}$ is a very small value, the tangent can be replaced by the Taylor series form,

$$\tan(kl) = kl + \frac{(kl)^3}{3} + \frac{2(kl)^5}{15} + \cdots \ldots\ldots\ldots\ldots\ldots \quad (1.65)$$

When $kl < \frac{\lambda}{16}$, we keep only first term and neglect the higher term within about 5% error.

So, we can define the acoustic inductance for an open-end tube as

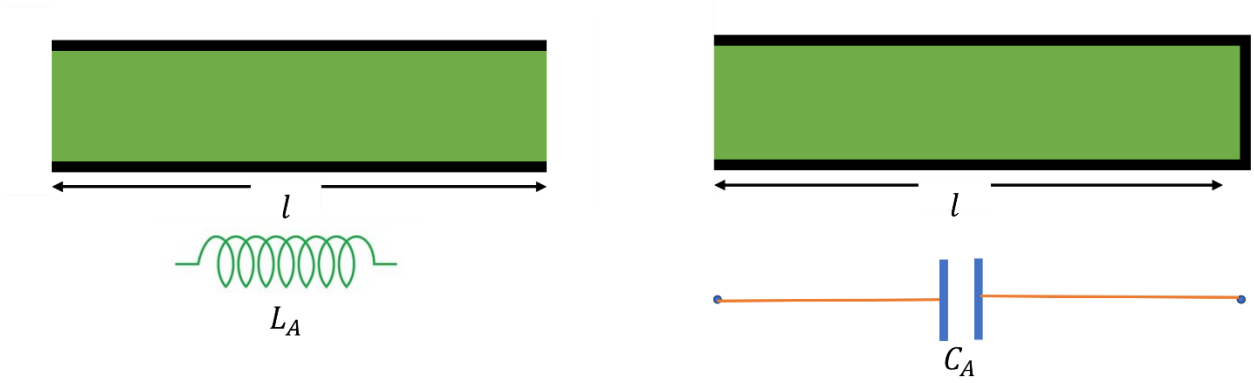

Figure 1.17 :A tube with open end and rigid end is analogous to an acoustic inductor and acoustic capacitor respectively.

$$\mathrm{LA}L_A = j\omega\frac{\rho_0 l}{S} \quad (1.66)$$

In the case of open pipe there should be considered the radiation correction factor for accurate calculation, and it is $l' = l + 8a/3\pi = l + 0.85a$, where a is the radius of the tube.

If the tube is rigidly closed at one end , substitute $Z_{Al} = \infty$ in equation (1.63)[17]

$$Z_{A0} = -j\frac{\rho_0 c_0}{S}\,\mathrm{Cot}\,(kl) \quad (1.67)$$

For small value of kl ,the cotangent cab be replaced by the equivalent series form.

$$\cot(kl) = \frac{1}{kl} - \frac{kl}{3} - \frac{(kl)^3}{45} \ldots\ldots\ldots\ldots \quad (1.68)$$

from equation (1.67) and (1.68),

$$Z_{A0} = j\frac{1}{\omega(\frac{v}{\rho_0 c^2})} + j\omega\frac{l\rho_0}{3S} + \cdots \ldots \ldots \ldots \quad (1.69)$$

Moreover, if the second term is small enough, we may omit it, so that the impedance of the cavity can be written as an acoustic capacitance. Z_{A0} is valid within 5% for l up to $\lambda/8$ series as a combination of an acoustic inductance and capacitance.

$$C_A = \frac{v}{\rho_0 c^2} \quad (1.70)$$

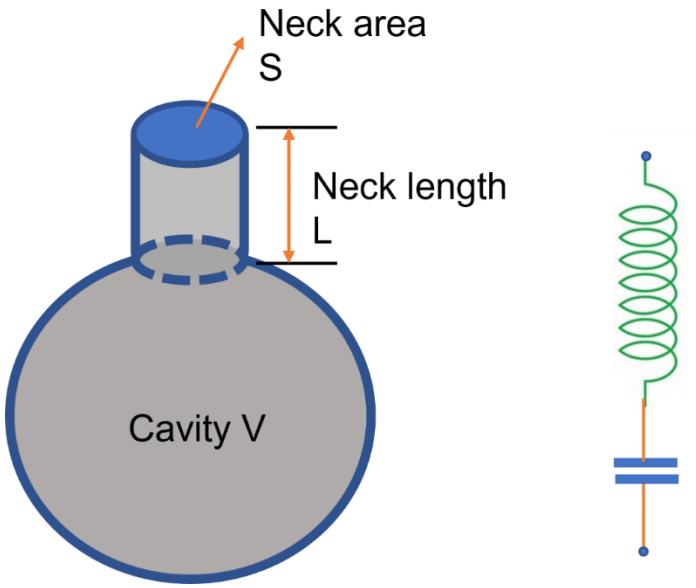

Figure 1.18: A Helmholtz resonator and its electrical acoustic circuit.

Let's understand the concept of inductance and capacitance with the help of Helmholtz resonators as shown in Figure 1.18. Compared to the fluid in the neck portion, the fluid inside the cavity is much easier to compress. Additionally, the pressure gradient along the open neck is substantially higher than the pressure gradient inside the big cavity. With the smaller neck acting as an acoustic inductor as a result of the cavity's capacitive characteristic. The

cavity having volume of V act as a closed pipe and the neck as an open pipe, therefore Helmholtz resonators can be represented as a series connection of inductance and capacitance.

1.9 Motivations and an outline

Exposure to loud noises can cause hearing loss, stress, and communication problems, hence sound-absorbing materials are desirable in many vehicles and buildings. Active noise cancelling piezo - electric materials[18],[19], passive foams/foam-like materials and acoustic metamaterials(near-zero, single negative, double negative)[20],[21],[22],[8] are common forms of noise dampening materials currently in use, although each has its own set of drawbacks. For the passive foam materials, for instance, weight and volume are issues because they are frequently rather heavy and voluminous. Certain vehicles, like aircraft, may have heavy foam put inside of them, which could increase fuel consumption and decrease operating efficiency. Another drawback of passive foam materials is that they are often not intended to absorb sound in frequency ranges of importance that are particular to a given application. Although piezo-based systems might be lighter and/or smaller than foams, they still need hardware, like electrical parts, circuits, and power supply. In comparison to passive foams, piezo-based systems are typically more difficult to build, install, operate, troubleshoot, and repair. The reliability of the systems might also be a problem. Perforated panels, porous and fibrous materials, gradient index materials, and similar items are used in several traditional methods of acoustic absorption. These materials frequently exhibit poor sound absorption properties in the low frequency range, necessitating the use of very thick structures with dimensions corresponding to the working wavelength. For particular applications, such as aircraft applications where component sizes and weights are rigorously

restricted, the structures may be overly thick and/or heavy. There is a need for a lightweight, thin sound-absorbing panel, air ventilated effective panel and broadband sound absorber, that is effective in dampening noise within an interest frequency range, such as at low frequencies.

In this dissertation, we will use metamaterial structures to design noise control devices that overcome the limitations of current designs, as discussed above. Based on Ashoke chakra and fractal structure and a broadband sound absorption acoustic panel will be proposed and cover in the chapter 2, chapter 3, and chapter 4.

Other two novel metamaterials have been designed for the air circulation as well as the sound absorption will be discussed in chapter 5, and chapter 6. Traditional acoustic barriers that are intended to isolate sound also prevent airflow transfer. While in reality, there may be some specific situations that require both airflow passage and noise suppression at the same time. For instance, natural ventilation, a crucial element of green architecture, unavoidably results in residents having to put up with the "intrusive" noise that goes along with it. The conventional thinking is to construct a one dimensional and two-dimensional planer metamaterials to provide an airflow path in order to achieve a soundproof barrier that also allows airflow through.

The outline of the thesis as follows.

Chapter 2, Introduction of a one-of-a-kind Ahok Chakra-like metamaterial for optimal sound absorption in the low frequency band. The finite element approach is used to investigate the effect of resonant frequency tunability at various parameters such as circular hole diameter, number of spokes, spoke length ratio, and cavity thickness. The simulation, theoretical modelling, and experimental results are all in good agreement.

Chapter 3, Fractal-based acoustic observer is presented in this chapter, specifically. Acoustic energy is damped inside the structure by using fractally distributed Helmholtz resonators that is created at the local resonant mode of the metamaterials. A thorough theoretical model analysis of the FAM is created and validated via FEM simulation and experimental.

Chapter 4, The design of a high-performance broadband sound absorption and lightweight acoustic panel uses a cross perforated plate with absorption performance that is introduced in this chapter. Investigation is also conducted into how the cross-perforation ratio of the frame affects the panel's unit cells' ability to retain performance. The resulting design's testing result matches simulation well and exhibits outstanding sound absorption in a broadband in the middle and low frequency zones.

Chapter 5, A study is presented on the development of a one-dimensional kink hollow fiber structure and high-performance acoustic absorption with air ventilation. Once more, a thorough theoretical analysis (Transfer Matrix Method) has been created and successfully validated using both simulation and experimental results.

Chapter 6, The flat spiral resonance created in coupled channels, and a ventilation channel for air circulation, is first examined in. Here, a novel subwavelength device with a thickness of 14mm (about 2 cm) is introduced. In this work, a miniature prototype that is built on a Fresnel spiral shape with numerous arms is designed and made. Through experimental and numerical investigations, the proposed ventilated metamaterial's acoustic characteristics in terms of sound absorption and air ventilation were identified. The findings of the experiment demonstrate excellent sound attenuation with a broad bandwidth (greater than one octave in the range of > 884 Hz), acoustic qualities that may have applications in the low- and mid-frequency regions of urban noise management.

Chapter 7, Finally, some noteworthy dissertation conclusions are presented in this chapter. Summary of the main findings of the work mentioned in section 1 and section 2. It also outlines the future scope of the programmable type metamaterials using shape memory polymers.

Chapter 2 : Ashok Chakra-structured meta-structure as a perfect sound absorber for broadband low-frequency sound

2.1 Background

Absorption of undesired noise is an indispensable aspiration in the field of acoustics. A sound absorber generally changes acoustic energy into some other form typically thermal energy via irreversible processes. The dissipation of acoustic wave propagation is governed by the frequency power law function.[23] The absorption of sound in deep subwavelength by homogeneous materials have always been a challenging task because of the dissipative power being quadratic in acoustic field amplitudes requiring high energy localization density inside the material.[24],[25] The sound absorption in this domain needs either higher field concentration or longer sound wave path.[26] The conventional method of acoustic absorption makes use of perforated panels, porous media and fibrous materials, gradient index materials, etc. These absorbers usually show a low level of impedance with respect to the incoming sound wave resulting in a poor sound absorber in low frequency and do require an overall bulky structure with dimensions comparable to working wavelengths. From the past decade, considerable efforts have been made to enhance the sound energy dissipation at deep subwavelength. Recently, total sound absorption has been realized by creating local resonant effect inside the artificially engineered acoustic meta-structures such as decorated membrane resonators (DMR),[27],[28] asymmetric absorbers,[29] honeycomb-corrugation hybrid core metamaterials,[30] Helmholtz-type resonators,[31],[32] acoustic coherent perfect absorbers (CPAs),[33] Mie resonance-based metamaterials,[34] etc. In recent years, a new type of technique called, the ‘concept of coiling up space’ has been used to increase the sound wave path in a thin structure of dimensions less than one-quarter of the working wavelength.[35],[36]

This type of meta-structures exhibit unique acoustic properties such as near-zero index, double negativity.[21] The coiling of space results in slow propagation of sound inside the meta-structure and dissipates the sound through thermal and viscous loss, which facilitates the achieving of sound absorption in low-frequency regime.[37] However, the current acoustic meta-structures are mostly reflective, and the effective bandwidth is too narrow to attenuate the noise. Recently, some progresses have been made in the development of perfect sound absorption systems. Wu et al. demonstrated a tunable acoustic absorber which possess a split tube resonating architecture.[38] Tang et al. proposed a hybrid meta-structure for absorption of low frequency sound**.** The structure proposed by them consisted of a perforated plate with honeycomb-corrugation hybrid core and exhibited broadband sound absorption behavior. Wang et al. reported the sound absorption using a layered acoustic metamaterial structure comprising of a porous sandwich layer between two coupled membranes.[39]

2.2 Structure design strategy

In this study, we propose a highly efficient tunable acoustic metamaterial panel for broadband noise reduction based on Ashok Chakra like meta-structures with subwavelength thicknesses as shown in Figure 2.1(a) consisting of an array of unit cells each of which is an Ashok-Chakra structure**.** Perfect sound absorption is achieved by dissipation of incident sound energy through the designed meta-structures. Figure 2.1(b) illustrates the basic design concept of a highly absorptive acoustic meta-structure in one unit cell of the array shown in Figure 2.1(a). It consists of a thin panel with circular hole (top), an intermediate layer, inspired from the artificially textured Ashok Chakra-like frame (a circular wheel comprising of 24 radial spokes), and supported with a back plate.

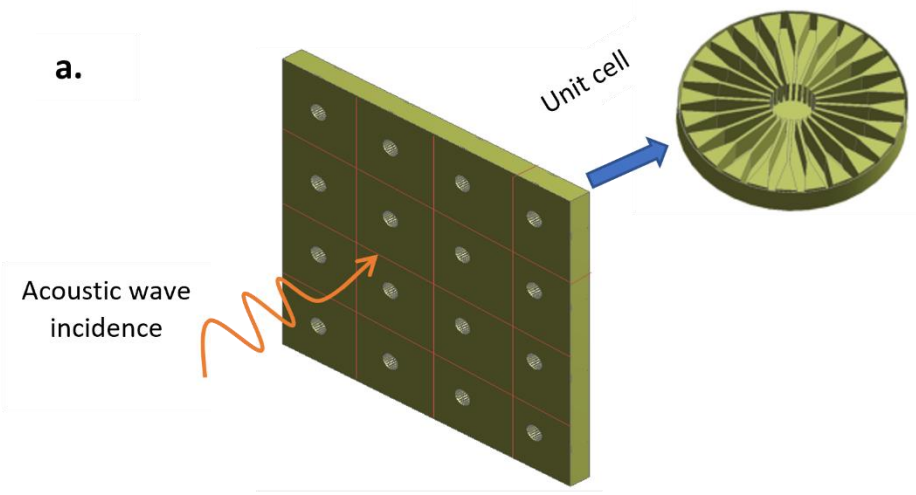

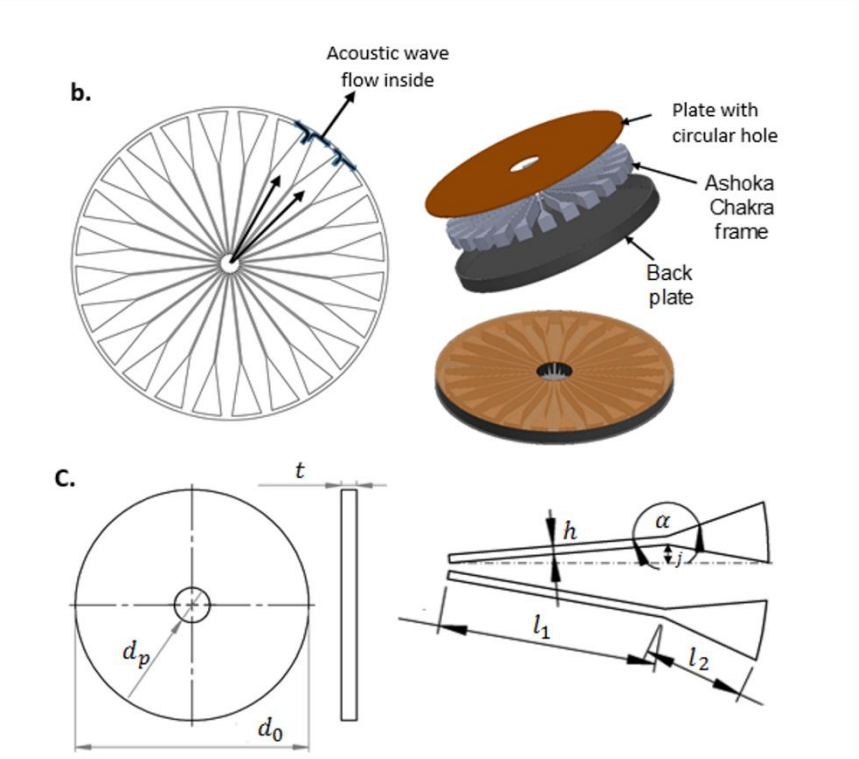

Figure 2.1: (a) Schematic representation of the proposed highly efficient tuneable acoustic metamaterial panel with an array of Ashok chakra shaped unit cells. (b) Schematic of a unit cell of the proposed acoustic metastructure, the exploded view of the absorber (right). (c) Schematic of the acoustic structure assembly d_p is the diameter of circular hole of the plate

dia, d_0, tp are diameter and thickness of perforated plate, l_1/l_2 is the spoke length ratio, h is the spoke thickness, and α is the obtuse angle of spoke called spoke angle.

The Ashoka Chakra structure has 24 spokes radially connecting two concentric annular with the spoke layout designed in a manner so that the inter-spoke distance for some fraction of the spoke length in the radial direction is divergent beyond which it converges. The thin front panel contains a cut-through circular hole to allow for propagation of acoustic waves into the absorber. Then, the acoustic scalar waves would propagate along the converging-diverging channels, i.e., along the gaps between the two spokes from the center point to the outer periphery as shown in Figure 2.1(b). The bottom panel is a thin, rigid plate which prevents sound leakage. The details of an absorbing unit cell are shown in Figure 2.1(c)

2.3 Theoretical modeling

First, the sound absorption characteristics of the proposed meta-structure (at the unit cell level) are analyzed using an impedance-based numerical analysis scheme. In general, the acoustic surface impedance at the inlet of the meta-structures is given by: $Z_s = Z_P + Z_C$, where Z_P and Z_C are the acoustic surface impedance of the perforated plate and cavity respectively. The acoustic impedance of perforated plate Z_P is calculated from a relationship which was arrived at for a small circular tube based on the solution of Crandall by Tang et al.,[30] Ruiz et al.,[40] and Maa:[41]

$$Z_P = \frac{j\omega\rho_0 t_p}{\phi}\left[1 - \frac{2J_1\left(y_n\sqrt{-j}\right)}{\left(y_n\sqrt{-j}\right)J_0\left(2\sqrt{-j}\right)}\right]^{-1} + \frac{\sqrt{2}\eta y_n}{\phi d_p} + j\frac{0.85\omega\rho_0 d_p}{\phi} \qquad (2.1)$$

Here, d_p and t_p are the hole diameter and thickness of the perforated plate, respectively. ω is the angular frequency, ρ_0 is the density of air. J_0, J_1 are the Bessel function of the first kind of

zeroth and first order respectively. y_n is a dimensionless factor which is the ratio of hole diameter d_p to the viscous boundary layer thickness δ_{visc}, and may be termed as the perforate constant. It is determined from the relation, $\delta_{visc} = \sqrt{2\eta/(\omega\rho_0)}$, where η is the dynamic viscosity coefficient of air (Pa.s). $\phi = \pi {d_p}^2/4A_c$, A_c is the total area of the plate, Indicate porosity of the perforated plate side. The last two terms on the right-hand side in equation (2.1) are the end corrections corresponding to the sound dissipation and radiation around the perforated hole inlet and outlet, respectively. For the perforated plate with uniform circular hole, the relative acoustic impedance is given as: $z_1{}' = Z_P/Z_0 = z = r_p + jx_p$, where r_p and x_p are the resistance and reactance of the acoustic impedance of perforated hole and can be expressed as[41]

$$r_p = \frac{32\eta t_p}{\phi\rho_0 c {d_p}^2}\left(\sqrt{(1+\frac{K^2}{32})} + \frac{\sqrt{2}}{32}\frac{Kdp}{t_p}\right) \tag{2.2}$$

And

$$x_p = \frac{\omega t_p}{\phi c}\left(1 + \left[1+\frac{K^2}{2}\right]^{-0.5} + 0.85\frac{d_p}{t_p}\right) \tag{2.3}$$

Here, $K = dp\sqrt{\omega\rho_0/4\eta}$. For the back cavity, the acoustic impedance is determined from the following equation:

$$Z_c = -j\frac{a_c}{a'_{cn}} Z_0 cot k_c t_c \tag{2.4}$$

where $Z_0 = \rho_0 c_0$ is the impedance of air, t_c is the cavity thickness and $k_c = 2\pi f/c$ is the acoustic wave number. $a_c = \pi r_c^2$ is the cross-sectional area of the cavity, a'_{cn} is the cross-

section of the unit cell in the incident side which is calculated as, $a'_{cn} = n \times \{(t_c \times w) + (2 \times j \times t_c)\}$, where n is the number of slits (Figure 2.1 **(b)**) and j is the slits thichness. Therefore, the relative acoustic surface impedance for the whole system can be given as, $Z = Z_s/Z_0 = (Z_p/Z_0) + (Z_c/Z_0) = r_s + x_s = r_p + j(x_p + x_c)$, where with the normalized surface impedance of the back plate x_c. Here, $(x_p + x_c)$ is the reactance offered by the perforated hole and compensated by the back cavity and r_p is the acoustic resistance of the structure which matches that of air. For a normally incident acoustic plane wave, the reflection coefficient can be related to the relative surface impedance as: $R = (Z - 1)/(Z + 1)$. Finally, the sound absorption coefficient of the sound absorber can be analytically obtained from the following equation:

$$\alpha(f) = 1 - |R|^2 = \frac{4r_p}{(1 + r_p)^2 + \left(x_p + x_c\right)^2} \tag{2.5}$$

As is evident from equation (2.5), for perfect absorption is achieved when $R \to 0$. In other words, for perfect absorption, two conditions, $(x_p + x_c) \to 0$ and $r_p \to 1$ have to be simultaneously achieved. To achieve these conditions, the thickness of the cavity, t_c, yields to be, $t_c = (c_0 a'_{cn}/\omega\, a_c) \cot^{-1} x_p$.

2.4 FEM (ANSYS) Simulation

Using the above relations, we analytically predict the sound absorption coefficient by considering the basic physics of sound absorption through the proposed acoustic meta-structure. The acoustic performance of the meta-structure is studied using a finite element-based simulation performed in ANSYS Acoustic Module[42] as shown in Figure 2.2. The acoustic-thermoacoustic interaction module is selected to perform the simulation of the sound

pressure wave in the air for a single unit cell as illustrated in Figure 2.1 before. The surrounding medium is chosen as air, for which the mass density, sound speed, and dynamic viscosity values are $1.2\ kg/m^3$, $343\ m/s$ and$1.8 \times 10^{-5}\ Pa.s$, respectively. Mechanical properties are same as used in Polyamide PA2200 polymer normally considered in 3D printing of the samples for the unit cell. The sound hard boundary conditions are applied at the interface of the air and solid. The plane wave radiation boundary is imposed at the termination of the downstream air domain to avoid multiple reflections of the sound waves. In order for the FEM method to be effectively applied, it's crucial to determine the cutoff frequency. This frequency marks the point below which only plane waves propagate within the duct. The cutoff frequency of the rectangular cross-section can be calculated as $f_{cutoff} = {c_0}/{H}$ [41], where H is the largest cross-sectional dimensions and c_0 is the speed of sound. Both upstream and downstream domains have the same cross-sectional dimensions 100 mm× 100 mm × 200mm.

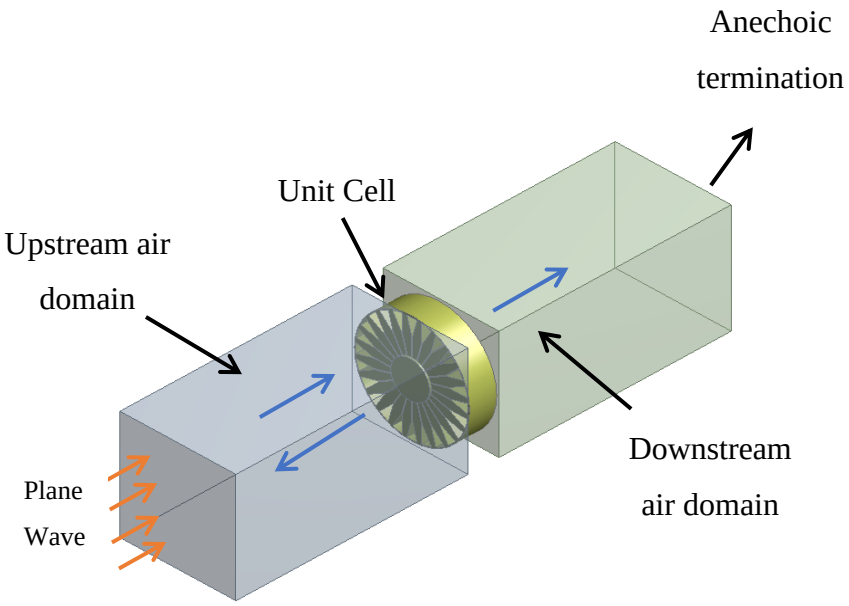

Figure 2.2: Noise attenuation performance of the proposed acoustic metamaterial: Acoustic analysis model to numerically evaluate the noise attenuation performance.

2.5 Acoustic characteristics of proposed structure

It is discerning that the resonant frequency and sound absorption bandwidth of the meta-structures are considerably dependent on the geometrical parameters. So, in the following, the effect of various geometrical parameters on sound absorption performance is examined through simulations. It is observed that with an increase in the circular hole diameter, the overall sound absorption coefficient increases (Figure 2.3(a)). It is due to the fact that if the perforated hole is too small, the fluid resistivity is very high, the incoming waves hardly penetrate the Ashok Chakra embedded rigid plate, and acoustic waves are thus reflected back.[20] There is almost no change in resonant frequency with the change in number of spokes while sound absorption coefficient increases with the number of spokes. This is due to the increased resistance at the air-wall interface. Also, as can be seen from the Figure 2.3(c), the spoke-length ratio highly influences the resonant frequency of meta-structures while a small variation in sound absorption coefficient is reported. A higher value of spoke length ratio (leading to a higher value of diverging side l_1), results in a left shift of the resonant frequency. In addition, the sound absorption of meta-structure increases with increase in cavity thickness of the meta-structure. Larger size of the central hole results in a right shift of the resonant frequency of the meta-structure **(**Figure 2.3(d)).As is evident from Figure 2.3, absorption coefficient of meta-structure depends on various geometrical parameters such as perforated hole diameter, number of spokes, spoke length ratio, back cavity thickness, etc. So, it is very cumbersome to choose appropriate sizes of the meta-structure.

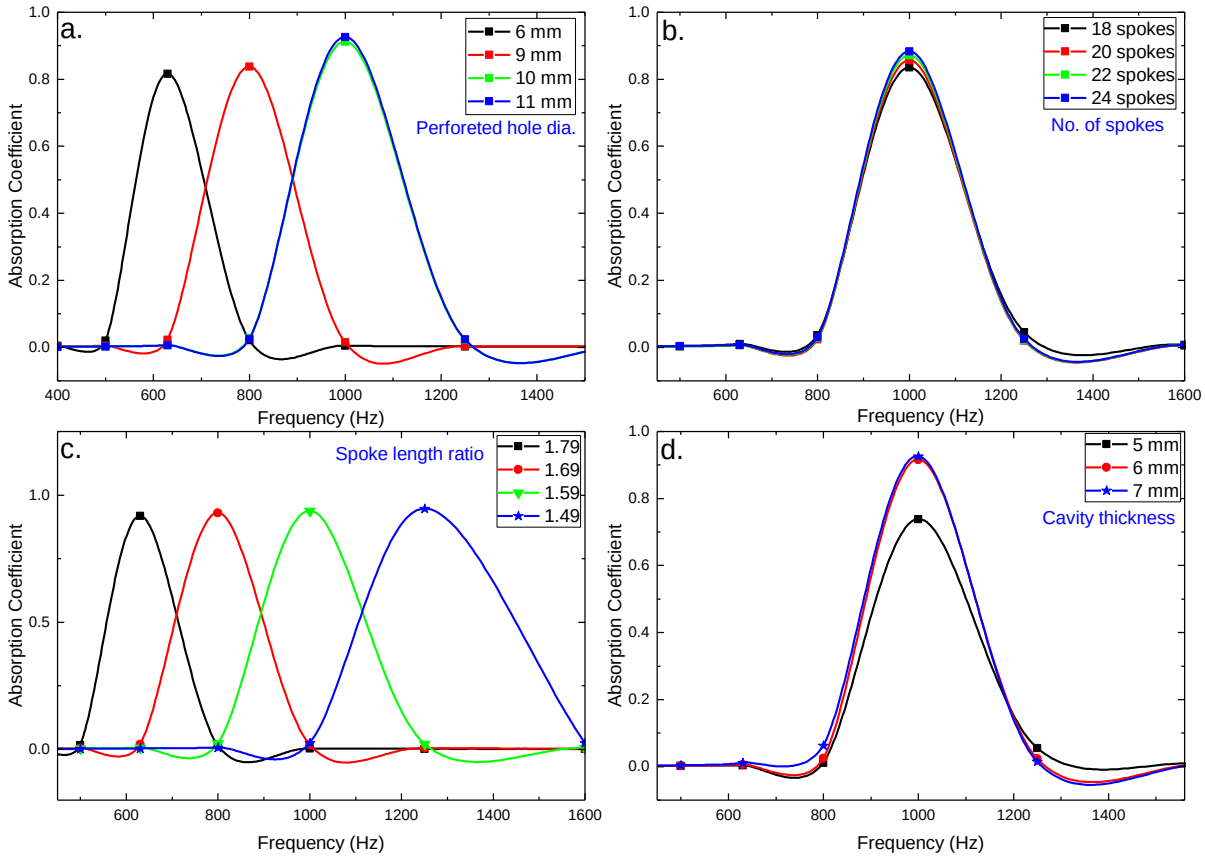

Figure 2.3 : Simulation results of various parametric sweeps to study the resonant frequency tunability of the acoustic meta-structure. a, Circular hole dia. b, Number of spokes c, spoke length ratio and d, back cavity thickness.

A circular unit cell sample of acoustic metastructure of 100 mm diameter is fabricated by 3D printing technique using a thermoplastic polyamide polymer (PA2200). The photograph of the fabricated samples by 3D printing is shown in inset of Figure 2.4 (a). The fabricated sample is mounted into an impedance tube system (Brüel & Kjær type-4206) to measure its absorption coefficient by using the standard transfer-function method. Five consecutive measurements are performed and averaged to increase the signal-to-noise ratio.

Figure 2.4 **,** shows the absorption coefficient curve of the acoustic absorber in the frequency range of 63-1600 Hz. The experimental result exhibits the high absorption coefficient (>40%)

over a wide frequency range (800-1600 Hz) and almost perfect absorption ($\alpha = 0.998$) is obtained at 1000 Hz. The corresponding working wavelength to thickness ratio of the proposed meta-structure at the resonant frequency is 7.08 (>4) which confirms that the sample is within the subwavelength scale. Therefore, the proposed Ashok Chakra-structured meta-structure with sub-wavelength sizes, showed significant absorption in the low-frequency domain.

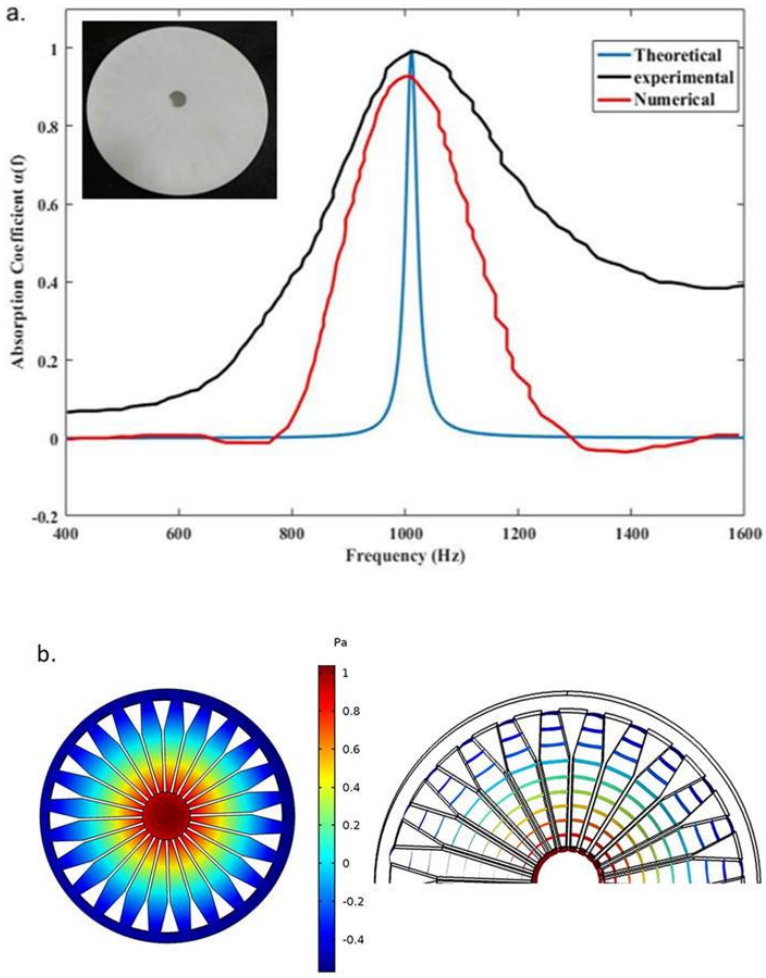

Figure 2.4: Sound absorption coefficient vs. frequency: experimental, theoretical and Numerical.

Further, the experimental results are quite comparable with simulated absorption coefficients. An overall good agreement is seen between the simulated and experimental results except that the absorption coefficient values are higher for the experimental case. This discrepancy between the two may have resulted from improper fitting of the sample in the impedance tube[21] and the excitation of plate modes of the solid medium of the meta-structure. Additionally, unlike the numerical simulation (smooth surface considered), surface of the 3D printed sample is generally rough which further enhances the energy dissipation in the meta-structure.

The array of four and six identical unit cells having 7 mm thickness were placed periodically in the y-z plane as shown in Figure 2.5 ((a),(b)), so that an acoustic metamaterial panel could then be built for observing the broadband behaviour of the structure.

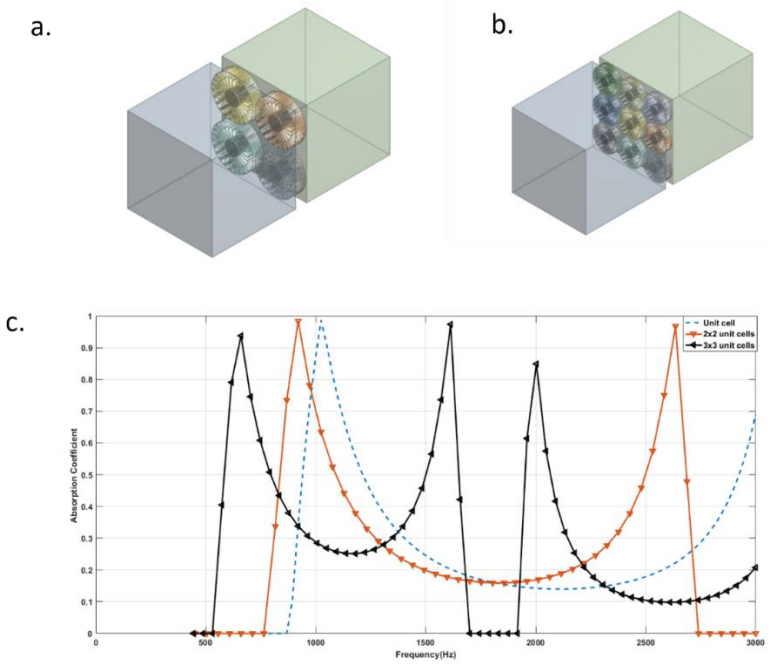

Figure 2.5: (a) 2x2 Unit cells arranged in rectangular manner. **(b)** 3x3 Unit cells arranged in rectangular manner. **(c)** Sound absorption coefficient vs. frequency: unit cell, 2x2 unit cells and 3x3 unit cells

In Figure 2.5(a)-(c) we are able to see multiple peaks coming from the 2x2 unit cells array and the 3x3 unit cells array where there is an overall reduction in the absorbance over multiple frequencies. This behavior of the simulated data may correspond to the broad band dampening effect although at some cost of reduced overall absorbance. In summary, a sound absorbing panel containing the Ashok chakra-like frame has been designed and fabricated. Almost perfect absorption (>99%) is achieved with the proposed design with subwavelength dimensions ($\lambda/7$).

2.6 Conclusion

A sound absorbing panel containing the Ashok chakra-like frame has been designed and fabricated. Almost perfect absorption (>99%) is achieved with the proposed design with subwavelength dimensions (k=7).

Acknowledgement

This work was supported by Boeing International Corporation India Private Limited (Grant No. BOEING/ME/2016081). A U.S. patent (Publication No.: U.S. 2020/0239125 A1) has been filed based on the results reported in this manuscript.

Chapter 3 : Novel fractal acoustic metamaterials (FAMs) for multiple narrow-band near-perfect absorption

3.1 Introduction

The metamaterial concept was first introduced in the field of electromagnetics and was subsequently extended to acoustics. Acoustic metamaterials are planned and designed structures exhibiting damping properties that are generally not found in naturally occurring materials. The acoustic properties, namely, effective mass density and effective bulk modulus of the metamaterials, depend upon the structural design/geometry rather than the chemical composition. The effective noise absorption at a low frequency of generally 100–1600 Hz is very difficult to obtain by using traditional acoustic materials due to the long wavelength of acoustic signals (3.43–0.21 m) and weak intrinsic dissipation. For sound absorption in this low-frequency range, porous materials are generally preferred, which follow the mass law.[43] According to this law, the lower the target frequency at which dissipation should occur, the greater the thickness of the structure and the mass. A similar damping behavior is found to happen in some alternate structures like micro-perforated plates and Helmholtz resonators showing less dependency on structural thickness. Metamaterials of this type are based on distributed cavity volume through intensive micro-structuring. These alternate structures are light in weight and effective as sound absorbers and serve in many modern industrial applications, such as within aircrafts, automotives, and vibrating machinery.

In the past few years, acoustic metamaterials (AMs) have attracted a great deal of attention of the research community because of their remarkable properties, such as perfect absorption (nearly one),[44] negative mass density/bulk modulus,[45],[21] reflected sound

manipulation,[46] resistance for sound propagation,[47],[48] acoustic cloaking,[48],[49] etc. For achieving perfect absorption or broadband absorption in the low-frequency range, researchers have used various strategies like labyrinthine or space coiling type of sound paths,[50],[51],[52] membrane-type acoustic metamaterials,[53],[54],[55] periodic distribution of thin closed slits in combination with Helmholtz resonators,[56], Helmholtz resonators with embedded apertures,[57],[58] materials combining double negative acoustic properties,[21] radial acoustic meta-structures,[59] etc. By coiling channels and cavities, researchers have been able to achieve near-perfect sound absorption in small thicknesses almost to within a fraction of the incident sound wavelength. These designs have some drawbacks that limit their usefulness in real life scenarios. First, the lateral dimensions of these designs are high, which are linked to the effectiveness of sound absorption. Also, it is difficult to adjust the absorption bandwidth of these structures owing to their long sound paths. Spiral meta-structures or equally dividing cavities have been reported to produce perfect sound absorption at desired frequencies.[59] The performance of these structures depends upon the channel thickness and length and, thus, there may be inconvenience in tunability. However, these structures need a careful selection of structural parameters at the very initial stages in order to realize near-perfect sound absorption at the targeted frequency. Moreover, these complex geometries can only show single frequency sound absorption and pose many limitations in terms of their easy manufacturability. Hence, developing thin sound absorbers that can shrink the vertical and lateral dimensions simultaneously while obtaining multiple narrow banded absorption peaks remains a challenging task.

The development of fractal geometry is generally inspired by an in-depth study of the naturally created patterns found in clouds, trees, foliage plants, galaxies, etc. The term “fractal” is

derived from the Latin word “fractus,” meaning broken, fragmented, or irregular, and was conceived by the mathematician Benoit Mandelbrot in 1975. He studied the different patterns found in nature and produced his immense work in his book titled “The Fractal Geometry of Nature.” [60] He defines fractal geometry as “that that can be split into parts, each of which is (approximately similar) a shrinking copy of the whole.”

Fractal metamaterials have been extensively used in electromagnetic applications because of their many unique properties like miniaturization, multiple resonating peaks, multiple modes, and self-matching aspects.[61],[62],[63] Similarly due to properties like self-similarity, researchers have used these materials in the field of acoustics to realize acoustic barriers,[64] acoustic lenses,[65] labyrinthine fractals,[66] etc.

To overcome the above-mentioned challenges, in this paper we explore a novel, thin, and highly efficient tunable fractal acoustic metamaterial (FAM) panel based on side branch Helmholtz resonators. The FAM structures use different sizes of the side branches distributed fractally on the wall of a backing plate in the meta-structures. Moreover, the proposed structures use four equal fractals arranged at angles of 0°, 90°, 180°, and 270°, respectively. Each of the Helmholtz resonators further subbranch into reduced dimension structures with the same aspect ratios but with scaled down dimensions. The purpose of this geometry is to increase the absorption coefficient and shift the resonance peak toward lower frequencies. Furthermore, this shift happens without changing the overall thickness of the metastructure. We report an analytical model based on the equivalent impedance method that represents the complete acoustic characterization of the meta-structure and further helps to estimate the absorption coefficient. This model has been further corroborated through finite-element analysis and thorough experimental validation.

3.2 Fractal metamaterial description and theoretical modeling

3.2.1 Fractals acoustic metamaterial design strategy

Figure 2.1 shows the different steps of constructing this new kind of FAM structure. Figure 3.1(a) depicts the base unit of the fractal shape with a design that contains multiple Helmholtz resonators. In the first step of realization, the unit shape is rotated by 90°, 180°, and 270°, respectively, to create four arms of the FAM, and these are interconnected in a cross-road-like manner [Fig. 3.1(b)]. As the Helmholtz arm iterates "n" times to a scaled down geometry, it is connected to the base arms (Helmholtz resonators) after a rotation of 90°. The scale factor used for such an iteration is 0.6 in respect to the previous dimensions without any change in the aspect ratio [Fig. 3.1(c)]. The final acoustic metastructure up to which we have investigated, corresponds to a "n" value of 3 [Fig. 3.1(d)].

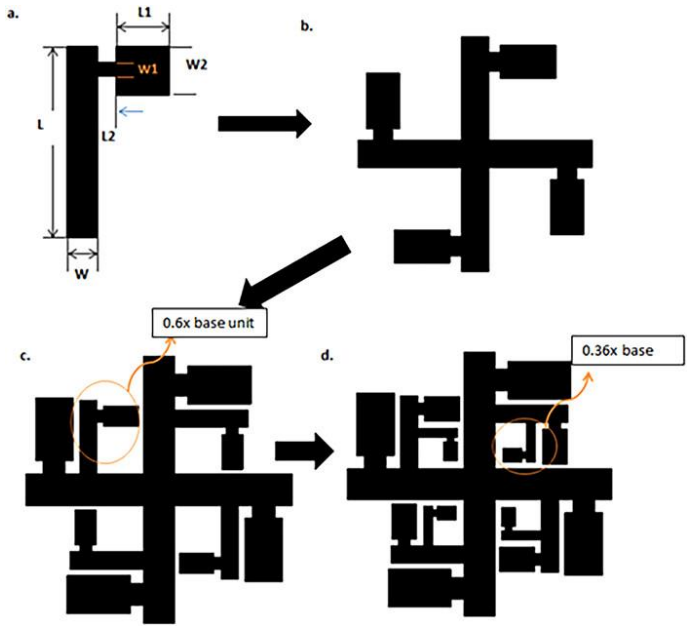

Figure 3.1 :Design procedure of the proposed acoustic fractal meta-structure geometry. (a) Basic unit shape. (b) First order fractal geometry. (c) Second order fractal geometry. (d) Third order fractal geometry.

The resonator design, as attached to each duct through a narrow side branch, is shown in Fig. 3.1(a), where the basic assumption is that the wave propagating through the duct is a plane wave and the sound attenuation would happen through an impedance mismatch in the resonator neck due to a sudden enlargement in the cross-sectional area. We achieve a perfect sound absorption and tunability by fractally arranging the Helmholtz resonators in the overall scheme shown in Fig. 3.1.

The designed structure uses the Helmholtz resonator to achieve perfect sound absorption behavior at a definite frequency of 1000 Hz by dissipation of the incident sound energy. Figure 3.2(a) shows the fractal acoustic meta-structure unit consisting of 12 resonators corresponding to a fractal order "n" of value 3. It consists of a thin panel with a single circular hole on the wave incident side at the middle of the FAM structure that is outlaid on a thin backing plate. The thin front panel with the perforation covering the FAM structure is used for propagating the plane waves into the metastructure, and, thus, the total acoustic energy is distributed into the fractals. [Figure 3.2(b) shows a plan view.] The bottom panel prevents any sound leakages and adds to the sound confinement within the structures. The FAM exploded view of the unit cell is shown in Fig. 3.2(c). The sample is made through the fusion deposition modeling (FDM) process using the materials' polylactic acid (PLA), as shown in Fig. 3.2(d). Absorption occurs mostly at the viscous and thermal boundary layers formed along the resonator walls.

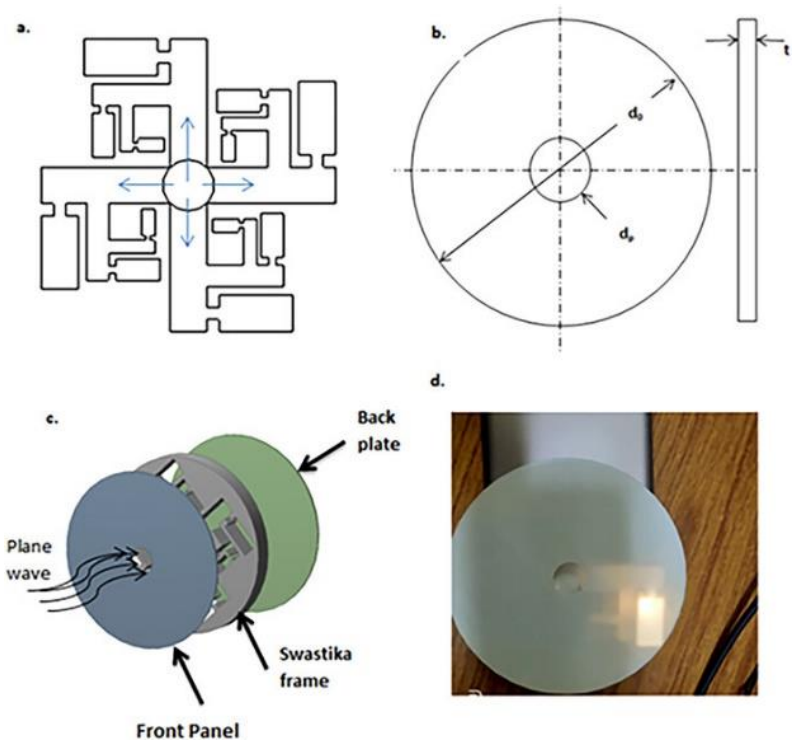

Figure 3.2. (a)Schematic diagram of a unit cell of the proposed acoustic meta-structure. (b) Schematic of the acoustic structure assembly. "dp" is the diameter of the pore and "d_0" and "t" are the diameter and thickness of the meta-structure, respectively. (c) Exploded view of the absorber. (The acoustic structure consists of a front panel with a pore, a fractal frame, and a backing plate, and the assembled view) (d) 3D printed sample having optimized dimensions of "dp" =11.68mm, "w_2/w_1" = 2, "l_1/l_2" = 20, and "tc" =8.5m

3.2.2 Theoretical analysis

We first introduce the equivalent impedance model representing the acoustic behaviour of the proposed meta-structure and present the optimization scheme adopted. The broad objective in this optimization is to converge on a design which possesses perfect absorption properties at targeted 1KHz frequency. In general, acoustic absorption of any system is defined as the sound

energy dissipation inside the material structure, as the sound traverses through a predetermined path. The acoustic absorption coefficient, α, of such a structure can be found by its normal acoustic impedance, Z , and this relationship can be given by[17].

$$\alpha = 1 - \left|\frac{Z_s - \rho_0 C_0}{Z_s + \rho_0 C_0}\right|^2 \tag{3.1}$$

where, Z_s refers to the surface impedance of the acoustic absorber, ρ_0 is the static air density and C_0 is the sound velocity. To get perfect sound absorption, impedance of the structure should match with the impedance of air, i.e., $Re(z) = \rho_0 C_0$ and $Im(Z) = 0$ as indicated by equation (3.1).

The surface impedance of the proposed structure can be represented in a general form as:

$$Z_s = Z_p + Z_c \tag{3.2}$$

where $'Z_p'$ denotes the surface impedance of the circular pore and $'Z_c'$ is the surface impedance of the meta-structure.

3.2.3 Surface impedance of the meta-structure calculation

The surface impedance of the circular pore $'Z_p'$ can be determined from a relationship for a small circular tube based on the solution of Crandall's theory by Maa[67] and Tang et al.[30] as shown in equation (3).

$$Z_P = \frac{j\omega\rho_0 t_p}{\phi}\left[1 - \frac{2J_1\left(y_n\sqrt{-j}\right)}{\left(y_n\sqrt{-j}\right)J_0\left(2\sqrt{-j}\right)}\right]^{-1} + \frac{\sqrt{2}\eta y_n}{\phi d_h} + j\frac{0.85\omega\rho_0 d_p}{\phi} \tag{3.3}$$

where $'d_p'$ and $'t_p'$ are the pore dimeter and the thickness of the front plate, $'\omega'$, $'\rho_0$' and J_0, J_1 refer to the angular frequency, density of air contained within the structure and the first kind

of Zeroth and first order Bessel functions, respectively. The term y_n is a dimensionless factor which is the ratio of pore diameter to the viscous boundary layer thickness that is further represented by $\delta_{visc} = \sqrt{2\eta/(\omega\rho_0)}$, (where η is the dynamic viscosity coefficient of air). The porosity of the perforated plate is represented by the term $\phi = \pi {d_h}^2/4a_c$. The last two terms on the right-hand side of equation (3) are the end corrections corresponding to the sound dissipation and radiation around the perforated hole inlet and outlet, respectively.

The surface impedance of the circular pore can also be represent in terms of resistance and reactance by the expression given as [28,][68]

$$\mathrm{Z_p} = \mathrm{r_p} + \mathrm{jx_p} \tag{3.4}$$

From the equation (3.3) and equation (3.4), we get.

$$r_p = \frac{32\eta t_p}{\phi c {d_h}^2}\left(\sqrt{(1+\frac{K^2}{32})} + \frac{\sqrt{2}}{32}\frac{Kd_h}{t_p}\right) \tag{3.5}$$

$$x_p = \frac{\omega t_p}{\phi c}\left(1 + \left[1+\frac{K^2}{2}\right]^{-0.5} + 0.85\frac{d_h}{t_p}\right) \tag{3.6}$$

The terms $'r_p'$, $'x_p'$ represent the resistance and reactance of the acoustic impedance offered by the perforated holes. The term $K = d\sqrt{\omega/4\eta}$.

3.2.3.1 Impedance of the cavity (z_c) calculation

As mentioned in the main manuscript, the surface impedance of the proposed fractal metamaterial absorber is represented with a general form as below:

$$z_s = z_p + z_c \tag{3.7}$$

Where Z_P and Z_C are the acoustic surface impedance of the perforated plate and cavity respectively.

The proposed structure consists of four identical units (having 3 Helmholtz resonators) of the type as shown in Figure 3.2 (a), placed parallelly with the perforated hole. Using an equivalent impedance concept, we can explain the acoustic characteristics according to the resonator's arrangement.

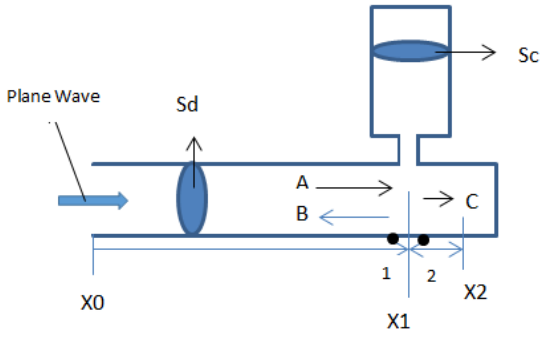

Figure 3.3. One branch of the unit cell of the FAM

The sound pressure (p) and the velocity (U) can be expressed as follows:

$$P_1 = \mathrm{A}e^{-jkx} + \mathrm{B}\, e^{jkx}\ , P_2 = \mathrm{C}e^{-jkx} \tag{3.8}$$

$$U_1 = \frac{1}{z}\left(Ae^{-jkx} - \mathrm{B}e^{jkx}\right), U_2 = \frac{1}{z}\left(\mathrm{C}e^{-jkx}\right) \tag{3.9}$$

The impedance of the resonator Zr at section 'X1' can be expressed as

$$Zr = -jZ_c \cot(kh) + Z_h \tag{3.10}$$

$$Z_h = \frac{\rho c}{s_h} [\, 0.0072 + jk\,(l + 0.75)] \tag{3.11}$$

Where Zc = $\rho c / s_c$ is the impedance of the cavity and Z_h neck impedance of the resonator. [69],[70]

S_h is the cross- sectional area of the neck.

We now take one complete branch of the unit cell and calculate the equivalent impedance of the cavity formulated therein. We make an electrical analogy of the structure as shown below in Figure 3.4, 3.5 and 3.6.

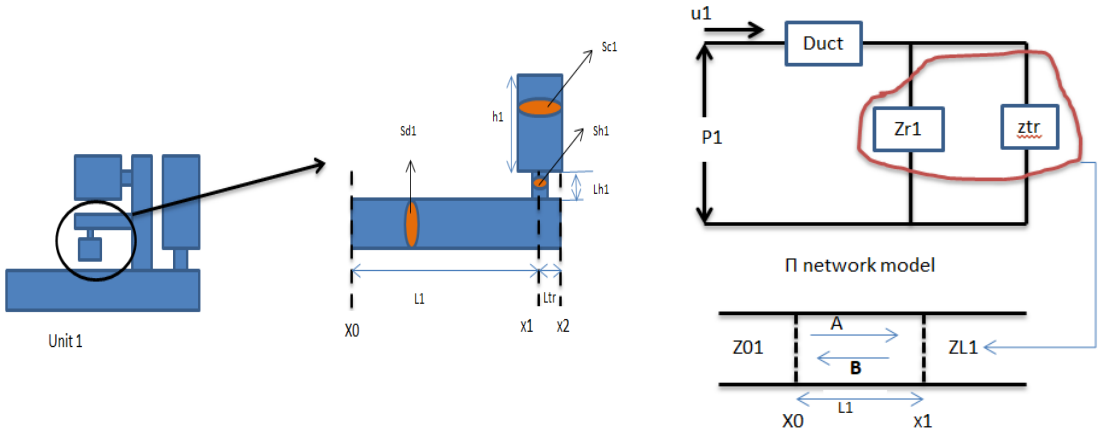

Figure 3.4 : Impedance model for one branch for a corresponding n value of 1

$$Zc1=\frac{\rho.c}{sc1} \tag{3.12}$$

$$ZL1=\frac{zr.ztr}{zr+ztr} \tag{3.13}$$

$$Zr=-j.zc1.\cot(k.h1)+Z_h \text{ ,where } Z_h=\left(\frac{\rho.c}{sh1}\right)(0.0072+j.k.(Lh1+0.75)) \tag{3.14}$$

$$Z01=z\frac{\left(\frac{zL1}{z}\right)+jtan(k.L1)}{1+j.\left(\frac{zL1}{z}\right)\tan(k.L1)} \tag{3.15}$$

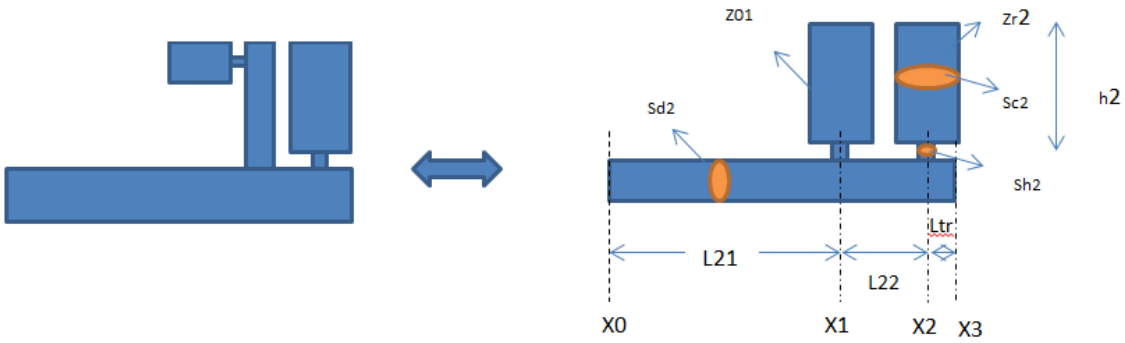

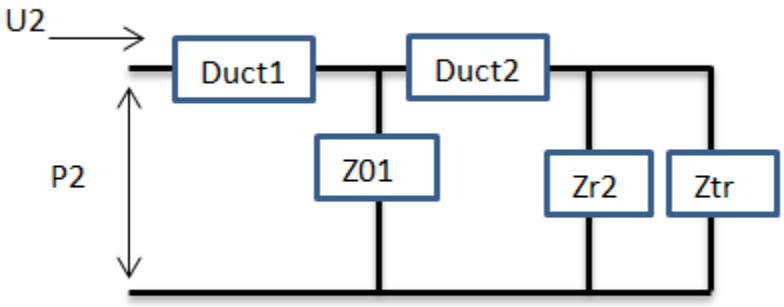

Figure 3.5: Impedance model for one branch with a corresponding n value of 2

$$Zx2 = \frac{\boldsymbol{Zr2\ .Ztr}}{\boldsymbol{Zr2+Ztr}} \tag{3.16}$$

$$Zx1 = Zd2\ \frac{\left(\frac{\boldsymbol{Zx2}}{\boldsymbol{Zd2}}\right)+\boldsymbol{j\ tan(kL22)}}{\boldsymbol{1+j\left(\frac{Zx2}{Zd2}\right)tan\ (kL22)}} \tag{3.17}$$

$$Z_{eq} = [\ (1/Z01) + (1/Zx1)]^{-1} \tag{3.18}$$

$$Z02 = Zd2\ \frac{\left(\frac{Zeq}{Zd2}\right)+j\ \tan\ (kL21)}{1+j\left(\frac{Zeq}{Zd2}\right)\tan\ (kL21)} \tag{3.19}$$

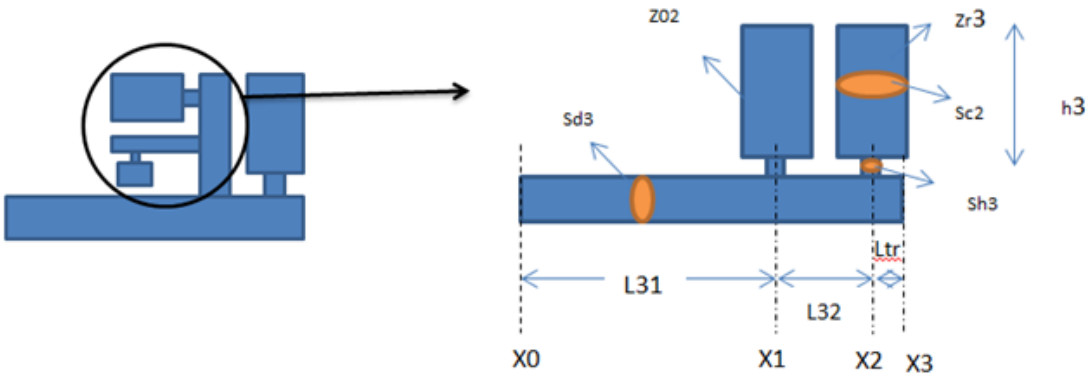

Figure 3.6: Impedance model for for the complete branch with a corresponding n value of 3

$$Zx2 = \frac{\boldsymbol{Zr3\ .Ztr}}{\boldsymbol{Zr3+Ztr}} \tag{3.20}$$

$$Zx1 = Zd3 \frac{\left(\frac{Zx2}{Zd3}\right)+j\ tan(kL32)}{1+j\left(\frac{Zx2}{Zd3}\right)tan\ (kL32)} \quad (3.21)$$

$$Z_{eq} = [\ (1/Z02) + (1/Zx1)]^{-1} \quad (3.22)$$

$$Z03 = Zd2 \frac{\left(\frac{Zeq}{Zd3}\right)+j\ \tan\ (kL31)}{1+j\left(\frac{Zeq}{Zd3}\right)\tan\ (kL31)} \quad (3.23)$$

There are 4 identical cavities placed parallelly in the complete unit cell, so the total impedance of the cavity.

$$Z\,c\ =\ Z03/4 \quad (3.24)$$

Putting the value of Z_p and Z_c in equation (3.7) can lead to the calculation of the surface impedance Z_s of the meta-structure. Now finally, the sound absorption coefficient can be obtained analytically by equation (3.1).

3.3 Optimization of the fractal structure

3.3.1 Regression analysis

Multivariate linear regression analysis is used to develop a functional relationship between the sound absorption coefficient α(f), and the geometrical parameters (perforated hole dia, Neck and cavity width ratio, Neck and cavity length ratio, and back cavity thickness) of the acoustic meta-structure. In this analysis, scores on the response variable ($\hat{Y}$) is predicted from the scores on predictors or regressors ($X's$) using the following relationship.

$$\hat{Y} = \beta_0 + \sum_{i=1}^{n} \beta_i X_i + \sum_{i}^{n} \sum_{j}^{n} \beta_{ij} X_i X_j \qquad (3.25)$$

Where β_0, β_i and β_{ij} are called the regression coefficients, $i = 1, 2, \ldots, n$ is the number of regressors.

RA (Regression Analysis) is performed by using Design Expert 8.0 software to form the equation connecting input and output response.

Using the Table 3.2, a second order regression model is developed which is given as

A=d_p , B =$\left(\frac{w2}{w1}\right)$, C =(l_1/l_2), D= t_c

$\alpha(f)$ =-1105.72 +11979.01* A - 2661.78* B+272.75* C+0.6820* D-0.2008* A * B+11978.56* A * C+0.7707*A * D-2662.29* B * C-0.0236* B * D+0.3695* C * D+7985.91* A^2+0.2713* B^2 +2436.62* C^2 + 0.0236*D^2+0.6126*A*B*D - 0.3315*A^2*B+7985.89*A^2*C+0.0348*A^2*D-0.7647A*B^2-0.3227*A*D^2-

0.6108*B^2*D+0.5445 *A^3-0.2662*B^3+

+1057.72*C^3-0.0005*D^3+0.2589* B^4

Values of "Prob > F" less than 0.0500 indicate model terms are significant. In this case there are no significant model terms.

Table 3.1: ANOVA Table

Std. Dev.	0.0633	R-Square	0.9965
Mean	0.6090	Adj R-Squared	0.9487
C.V. %	10.39	Pred R-Squared	N/A
PRESS	N/A	Adeq Precision	13.9092

"Adeq Precision" measures the signal to noise ratio. A ratio greater than 4 is desirable. Our model ratio of 13.909 indicates an adequate signal. This model can be used to navigate the design space.It can be concluded that the developed model fits the data well."

Table 3.2: Control factors and their levels

Control factors
Perforated hole Dia (d_p), mm
Neck and cavity width ratio(w2/w1)
Neck and cavity length ratio (l_1/l_2)
Back cavity thickness (t_c), mm

	Factor	Name	Units	Type	SubType	Minimum	Maximum	Coded Low	Coded High	Mean	Std. Dev.
	A	dp	mm	Numeric	Continuous	10.00	14.00	-1 ↔ 10.00	+1 ↔ 14.00	11.93	1.01
	B	w2/w1		Numeric	Continuous	2.00	6.00	-1 ↔ 2.00	+1 ↔ 6.00	3.57	1.44
	C	l1/l2		Numeric	Continuous	6.67	20.00	-1 ↔ 6.67	+1 ↔ 20.00	9.49	5.38
	D	tc	mm	Numeric	Continuous	6.00	9.00	-1 ↔ 7.00	+1 ↔ 9.00	8.37	0.9994

Table 3.3:Simulation results of the swastika type acoustic metamaterial.

Run	d_p	$w2/w1$	l_1/l_2	t_c	Alpha α (f) at 1000Hz
1	10	2.85	6.67	9	0.5
2	10	2	20	9	0.75
3	10	2	20	8	0.82
4	11	2	20	8	0.7
5	11	2	20	7	0.87
6	11	2	20	9	0.9
7	11	2.85	6.67	6	0.27
8	11	6	6.67	9	0.87
9	12	2.85	6.7	9	0.9
10	12	2.85	8	9	0.25

11	12	2.85	10	9	0.4
12	12	5	6.67	9	0.9
13	12	3.33	6.67	9	0.6
14	12	2.5	6.67	9	0.45
15	12	2	6.67	9	0.45
16	12	2.85	6.67	9	0.38
17	12	2.85	6.67	8	0.3
18	12	2.85	6.67	7	0.2
19	12	2.85	6.67	6	0.15
20	12	5	6.67	9	0.9
21	12	5	6.67	8	0.73
22	12	6	6.67	9	0.9
23	13	2.85	6.67	6	0.1
24	13	2.85	6.67	9	0.4
25	13	6	6.67	9	0.79
26	13	4	6.67	9	0.91
27	13	4	6.67	8	0.72
28	14	6	6.67	9	0.95
29	14	6	6.67	8	0.91
30	12	5	20	9	0.3

The Model F-value of 20.88 implies the model is significant. There is only a 4.67% chance that an F-value this large could occur due to noise.

P-values less than 0.0500 indicate model terms are significant. In this case A, B, C, AC, BC, A^2, C^2, A^2C, C^3 are significant model terms. Values greater than 0.1000 indicate the model terms are not significant. If there are many insignificant model terms (not counting those required to support hierarchy), model reduction may improve your model.

a.

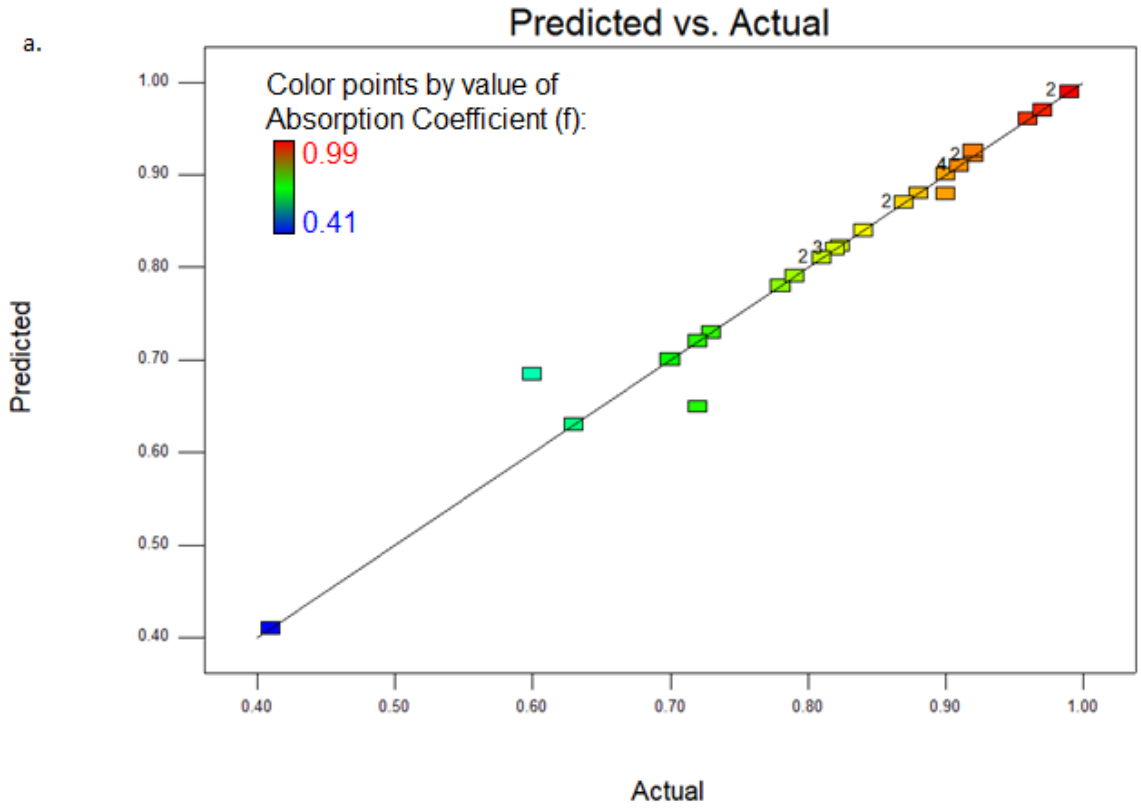

(b)

Factor Coding: Actual

All Responses

0 1

X1 = A

X2 = D

Actual Factors

B = 3.65303

C = 6.67293

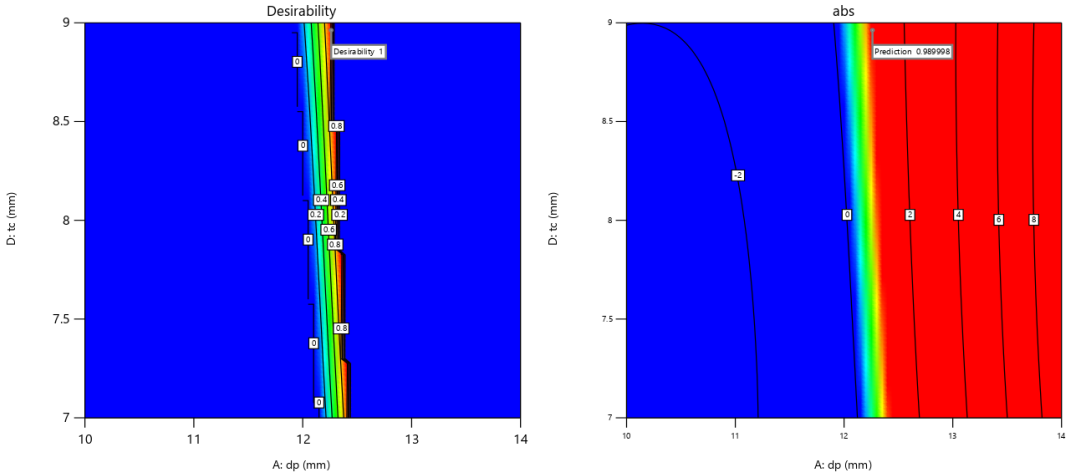

(c)

Factor Coding: Actual

All Responses

Design Points

0 1

X1 = A

X2 = B

Actual Factors

C = 6.67

D = 9

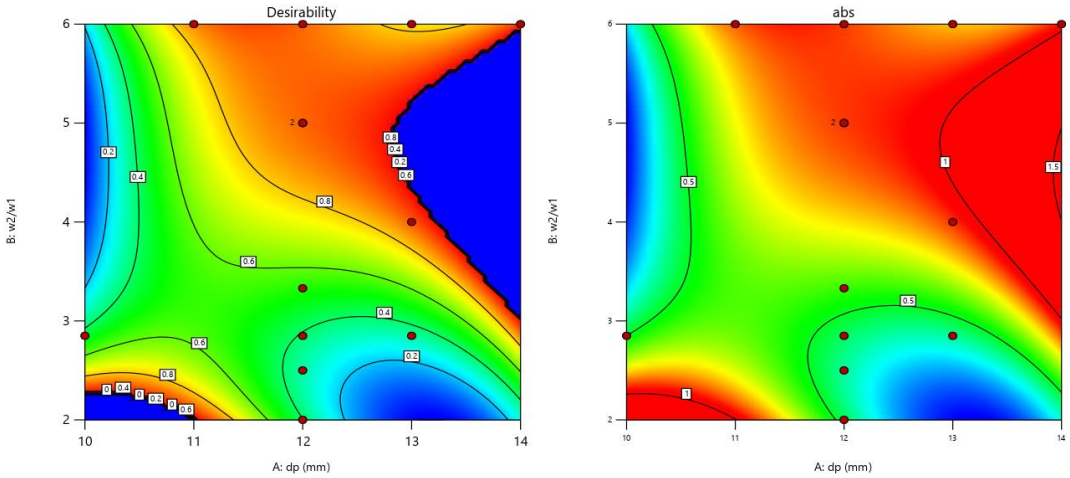

(d)

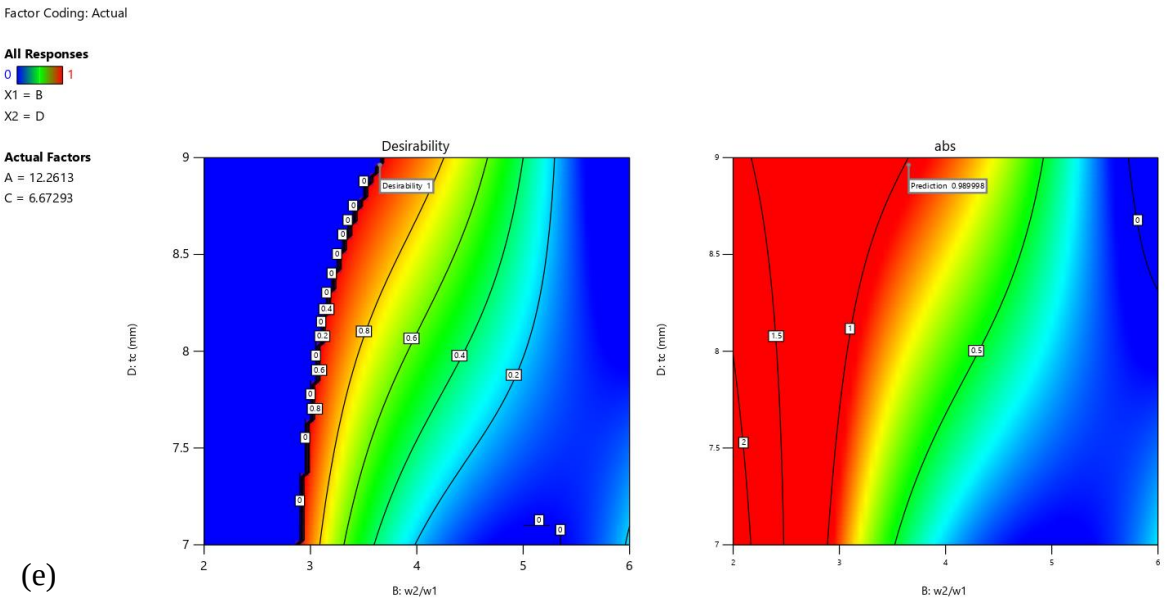

(e)

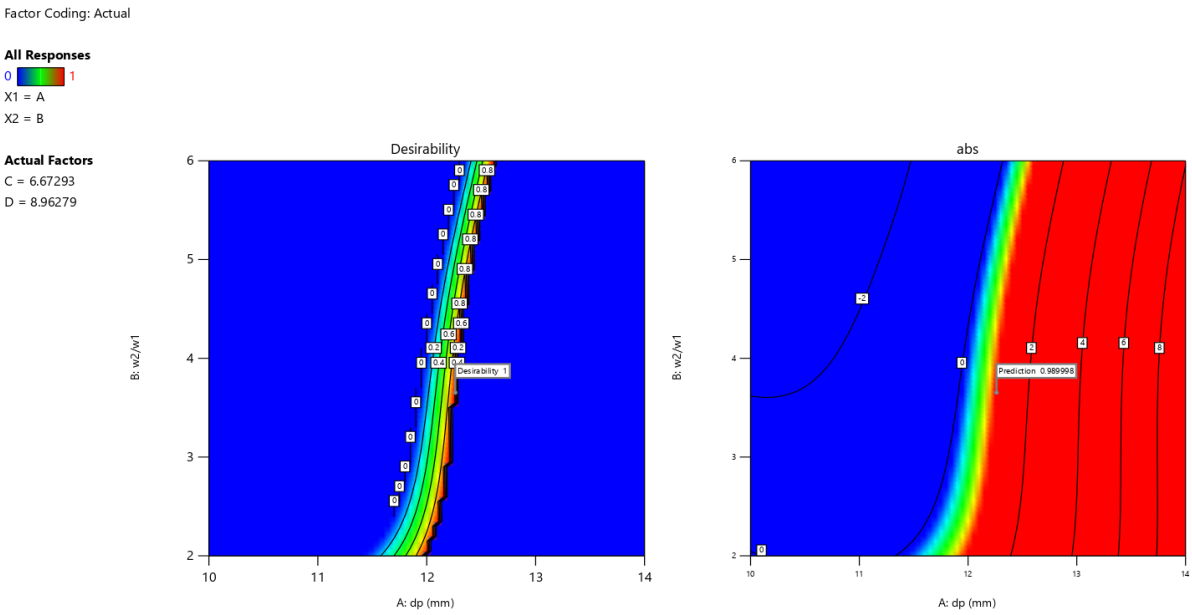

Figure 3.7: (a) Relationship between actual and predicted value **,(b), (c), (d) and (e)**, are the contour plots showing the interaction effects between geometrical parameters on absorption coefficient.

3.3.2 Meta-structure optimization by Response surface methodology

Numerical and graphical optimization algorithm is performed, using design Expert 8.0

To maximize || *sound absorption coefficient*

$$\alpha(f) = -1105.72 + 11979.01 * A - 2661.78 * B + 272.75 * C + 0.6820 * D - 0.2008 * A * B + 11978.56 * A * C + 0.7707 * A * D - 2662.29 * B * C - 0.0236 * B * D + 0.3695 * C * D + 7985.91 * A^2 + 0.2713 * B^2 + 2436.62 * C^2 + 0.0236 * D^2 + 0.6126 * A * B * D - 0.3315 * A^2 * B + 7985.89 * A^2 * C + 0.0348 * A^2 * D - 0.7647 A * B^2 - 0.3227 * A * D^2 - 0.6108 * B^2 * D + 0.5445 * A^3 - 0.2662 * B^3 + + 1057.72 * C^3 - 0.0005 * D^3 + 0.2589 * B^4 \quad (3.26)$$

Subjected to:

$$10 \leq d_p \leq 14$$

$$2 \leq \left(\frac{w2}{w1}\right) \leq 6 \quad (3.27)$$

$$6.67 \leq l_1/l_2 \leq 20$$

$$6 \leq t_c \leq 9$$

Table 3.4: Comparison result of FEM simulation and Design Expert Software

Method	d_p	$\frac{w2}{w1}$	l_1/l_2	t_c	$\alpha\,(f)$
Design Expert numerical optimization	11.68	2	20	8.5	0.99
ANSYS 17.0 Simulation	12	2.4	20	8	0.92

3.3.3 Comparison between new structure and conventional

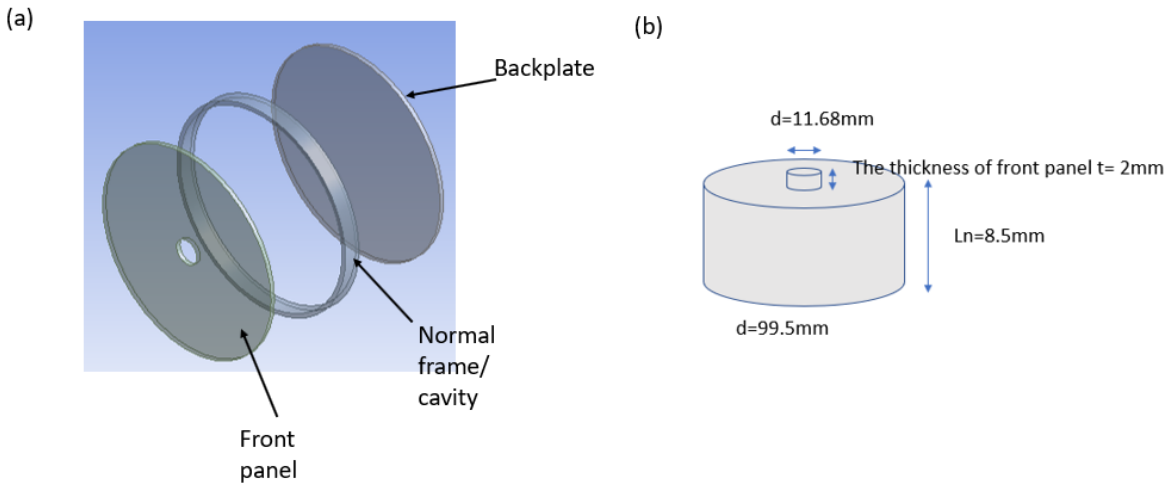

Figure 3.8: (a) Conventional structure without fractal structure (b) Corresponding equivalent Helmholtz resonator. (Equal Volume)

The natural frequency of the given Helmholtz resonators shown in fig 3.8(b) can be calculated by the expression given as [71]

$$f_n = \frac{c}{2\,\pi}\sqrt{\frac{A}{lV}} \tag{3.28}$$

Where f_n is a fundamentals frequency, c is velocity of sound, A is surface of opening area, l is the neck length and V is volume of cavity?

When we put all the value in the above equation, the natural frequency came around $f_n = 1700.24\ Hz$.

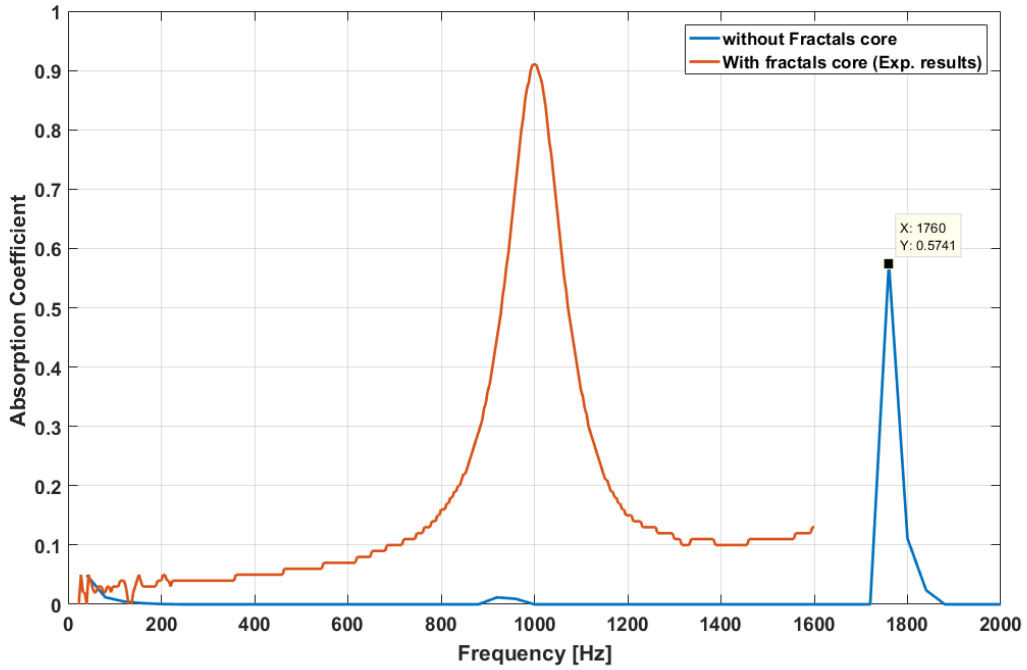

Figure 3.9 :(a) absorption coefficient of a sample with fractal core or without core.

3.4 Numerical simulation, Theoretical and Experimental validation

For understanding the acoustic characteristics of the proposed meta structure, the impedance tube testing has been performed and the results are further validated by the numerical simulation and theoretical modelling approaches [Fig 3.10 (c)].

3.4.1 Numerical simulation (FEM) and geometric optimization

For numerical validation purposes, the FEM acoustic model of fractal absorbers is used in ANSYS 17[15] (Acoustic module). A plane wave with unit amplitude is applied at normal incidence to the sample. Acoustic hard boundary conditions are imposed on all the walls of the acoustic absorber. This is important due to a huge impedance mismatch on the air-wall interface within the structure. Meshing is done using Tetrahedral elements. The largest optimal mesh element size is taken to be dimensionally smaller than $1/6^{th}$ of the shortest incident wavelength and further mesh refinement is carried out in the elements which are in regions of high error.

The sound absorption signature of the structure depends upon various geometric parameters like perforated hole diameter (d_p), neck and cavity width ratio (w2/w1), neck and cavity length ratio (l_1/l_2), back cavity thickness (t_c) etc. Thus, iterating to the most appropriate dimension of the independent variable is difficult for obtaining perfect sound absorption at a pre-defined frequency. For getting the optimized combination of four independent parameters to achieve perfect sound absorption, we have utilized the "Response surface methodology (RSM)" technique (Design Expert 11) for a target frequency of 1000 Hz. In this, we have used a statistical regression analysis tool[72] , and applied response surface methodology for optimizing the independent geometric parameters. The numerical values of the control factors and their different set levels are illustrated in Table 3.1. A number of simulation results are evaluated with the use of different parameters and their respective sound absorption coefficient at 1kHz peak within 0-1.6kHz frequency band are obtained [Table 3.2]. The high value of the coefficient of determination (R^2 =0.9965) of our model indicates the existence of an effective correlation between the experimental and predicted response values. The resulting structure

coming out of this optimization scheme is illustrated in Figure 3.2(d) and contains the geometrical parameters d_p =11.68mm, $^{w2}/_{w1}$ =2, $^{l1}/_{l2}$=20 and t_c=8.5mm. [ANNEXURE B.2}

A sample is further built using 3D printer with a diameter of 100 mm, as shown in Fig. 3.10 (a). The speed of sound and the density of PLA (i.e., the material used for fabrication) are c = 1200 m/s and ρ = 2700 kg/m3, respectively. The sound wave particle velocity flowing inside the structure is estimated, as shown in Fig. 3.10 (b). The absorption coefficient of the fabricated specimen within a range 600–1600 Hz is shown in Fig. 3.10 (c), as measured on a B&K type-4206T impedance tube system.

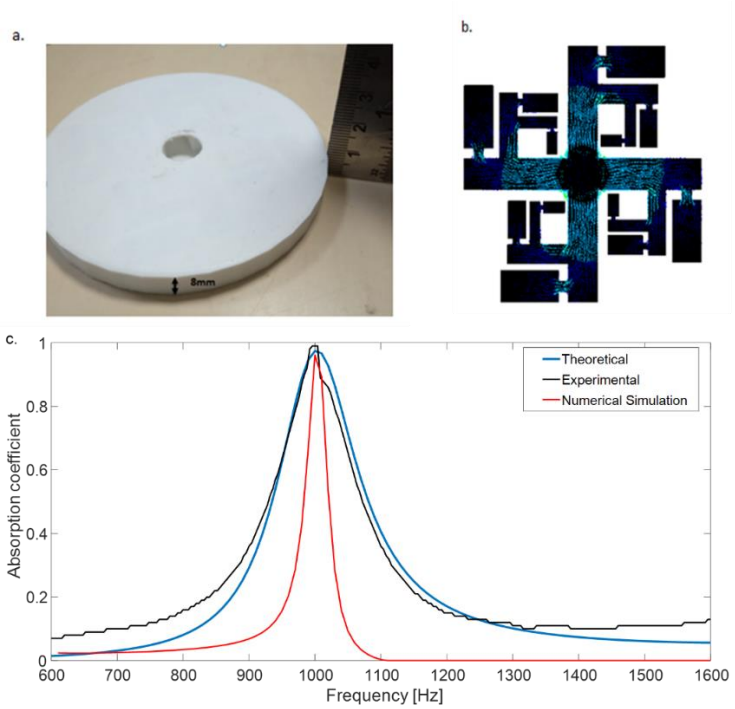

Figure 3.10: (a) Photograph of the experimental sample having thickness of 8mm. (b) Simulated sound velocity vector at 1000 Hz. (c) The absorption coefficient of the proposed fractal metamaterial. The solid black line, blue line and red line represent theoretical results, numerical simulation, and experimental results, respectively.

The acoustic absorption coefficient is measured following the ASTM-E1050-12 standard.4 The following parts are used to make the impedance setup: (a) an impedance tube (an inner size of 10 × 10 cm2), (b) two microphones (1/4-in.-diameter) (labeled M1 and M2), (c) a measuring module “Acoustic Material Testing” that is used to measure the absorption coefficient, etc. The thickness of the waveguide wall is treated as 6 mm. Because the rear of the wall is a hard boundary condition, we can assume that there is no sound transmission through the wall. By placing a structured material block inside the tube, the absorption spectra can be measured for the corresponding meta-surface of this block.

Figure 3.10 (c) shows a comparison of sound absorption coefficient at a target frequency of 1KHz obtained through theoretical analysis, FEM simulation and experimental analysis. The results show good agreement with each other. The experimental and theoretical measurement bandwidths are both large than the FEM simulated data which may intuitively be thought to be coming from viscous-thermal losses which are not considered in the FEM modelling.

Figure 3.10 (a) shows the actual thickness of the optimized FAM sample that is used for the impedance tube experimentation. Figure 3.10 (b) depicts how the sound wave particle velocity flows inside the chamber at the target frequency of 1000 Hz.

3.5 Results and discussion

3.5.1 Fractal order and its simulation

Fractals are generally defined as “an infinitely complex structure with self-similarity at different scales. The repetition of the process at different scales is known as the fractals order. In this paper, we used Helmholtz based fractal’s structure and three order of it as shown in figure 3.11. Helmholtz Resonators (HRs) are generally used in the design of silencers for noise

reduction. Noise reduction in these mostly happens due to impedance mismatch causing a reflection of the incident acoustic energy and attenuation in the resonator neck. Inspired by silencer design and physics we have designed the reported fractal metamaterials (FAM) using multiscale HRs arranged in a fractally reduced order of dimensions (orders signify the scaling down). The acoustical properties of first order, second order and third order fractal acoustic metamaterials have been evaluated. The Helmholtz resonators present in this FAM structure play a vital role in order to get maximum absorption and shifting of the resonance peak. The resonance frequency of HR (four in first order, eight in second order and twelve in third order) is calculated through the relation $f = c/2\pi\sqrt{\frac{A}{l\prime V}}$ where V is the volume of resonance chamber, A is the cross sectional area of the neck, l' is the effective length (including end correction) of the neck can be expressed $l'=l + 0.6a$, here l is the length of the neck and a is the radius of its cross section. The extra length or end correction added to the geometric length of the neck because of an extra volume (both inside and outside) move the air in the neck region. This is approximately 0.6-times the outside radius.

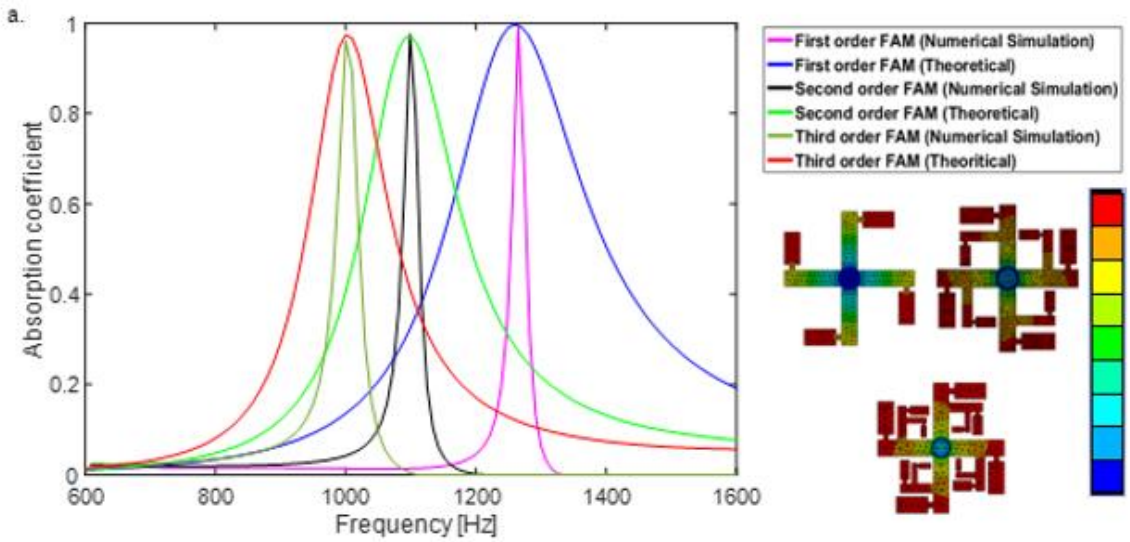

Figure 3.11: Sound absorption signature of first order, second order and third order fractals metamaterials absorbers and cross ponding SPL (sound pressure level) profile.

The characteristic resonant frequencies of three identical HRs present in a single arm of the FAM structure are 3126 Hz ,4967 Hz and 7832 Hz respectively. The comparison of the output of the FEM based numerical and theoretical models for various orders of geometries of the FAM structures are shown in Figure 3.11. As one can see from this plot, the absorption peak shifts towards the left as one goes from first to third order. The shifting of the resonance frequency happens due to an increase in the number of HRs. In the first order FAM there are only 4 identical HRs, in the second order a total of 8 HRs and in the third order a total of 12 HRs are present. This also indicates that as the order of fractals increase (i.e., ‘n’ value is increased) we can get desired acoustic absorbing frequencies whereas the absorption coefficient can peak with a shift towards the lower frequency bands as one increases the ‘n’ value.

3.5.2 Influence of geometrical parameters

We further use the acoustic FEM model to probe the effect of different design parameters of the FAM structures such as perforated hole dia. (d_p), neck and cavity width ratio (w2/w1), neck and cavity length ratio (l_1/l_2) and back cavity thickness (t_c) etc, on the acoustic absorption coefficient of the structures. The results are illustrated in Figure 3.12. With a fixed value of the parameters "d_p", (w2/w1), and (l_1/l_2), and with an increase in the thickness from 5mm (λ/69) ~ 25mm(λ/18), the sound attenuation band is found to move to low frequency domain [Fig. 3.12 (a)]. Moreover, when the ratio of Neck and cavity width ratio (w2/w1) is more than 3.33, two absorption peaks are obtained in the frequency range 600-2000 Hz [Fig. 3.12 (b)]. This happens due to the neck region of the HR narrowing down as we increase the ratio of w2/w1 causing an increase in sound dissipation. When w2/w1 is less than 3.33, we get a single absorption peak with a shift towards the left as we increase the neck and cavity length ratio (l_1/l_2) [Fig. 3.12 (c)]. Since we know that the resonance of HRs is inversely proportional to the neck length and the volume of the cavity, a similar behaviour is observed in Figure 3.12 (d) showing the interaction of neck length and resonators cavity volume on the absorption coefficient.

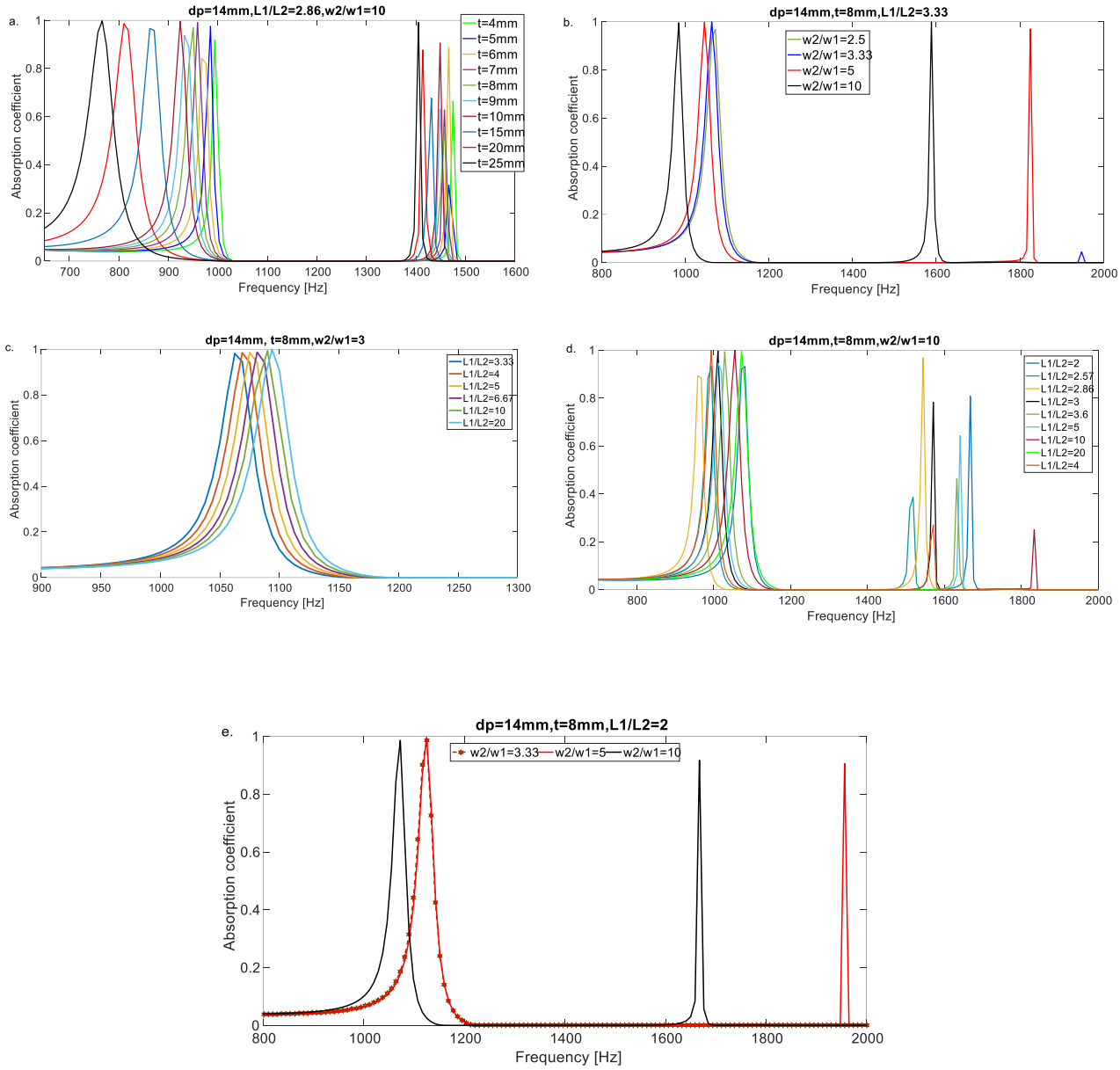

Figure 3.12: Absorption coefficient of the designed metamaterial with different acoustics parameters. (a)- (e) Varying absorption spectra with thickness t, neck and cavity width ratio (w2/w1), neck and cavity length ratio (l_1/l_2) of the Acoustic metamaterials

Figure 3.12 (d) shows the effect on the absorption spectra as we increase the neck and cavity length ratio (l_1/l_2) with other parameters fixed. In this case the resonance frequency $f \propto \frac{1}{\sqrt{l1l2}}$ and the absorption both depend on the combination of neck and cavity length illustrating an

abrupt shift in the resonance frequency due to a change in the energy dissipation rate inside HR regions. The relation between neck and cavity lengths shows a linear dependence. For example, as the cavity length is double of the neck length, and the cross section of the neck is increased in comparison to the cavity cross-section, the two absorption coefficient peaks ($\alpha >$ 0.9) are found to shift towards the left. This signifies a high loss of acoustic energy inside the neck of the resonators as shown [Fig. 3.12 (e)].

3.6 Conclusions

In summary, we have demonstrated a new kind of fractal structure with reducing geometric dimensions that possess properties of acoustic metamaterials. We have also analyzed the absorption behavior of these geometries at low frequencies. Multiple validations have been carried out through closed form analytical solutions (based on equivalent impedance analysis), numerical modelling efforts (FEM simulations) and experimental analysis. In addition, the structure is optimized geometrically to possess a peak absorption at 1 KHz frequency using Response surface methodology (RSM). By altering the internal geometry, the FAM is found to be amenable to tuning at multiple frequencies with narrow band absorptive behaviour and can be eventually used for acoustic cloaking in the low frequency domain.

Acknowledgement

This work was supported by Boeing International Corporation India Private Limited (Grant No. BOEING/ME/ 2016081). A US patent has been filed based on the results reported in this manuscript.

Chapter 4 : Hybrid fractal acoustic metamaterials for low-frequency sound absorber based on cross mixed micro-perforated panel mounted over the fractals structure cavity

4.1 Introduction

Numerous uses for the deep-subwavelength thick broadband low-frequency sound absorber can be found in acoustic cloaking and noise reduction. An acoustic metamaterial is an excellent candidate to tackle all challenges with careful design of structures that may possess extraordinary acoustic properties like broadband noise absorption [73],[74],[75],[76],[59], sound insulation [77],[78],[79], , noise cloaking properties [80],[81] , acoustic jetting properties [82] etc. Acoustic metamaterials are well known as artificial or man-made structures that may be programmed through negative effective density [83],[84], negative effective modulus [9],[85], and simultaneous negative modulus and density [86],[87],[88]. Researchers have recently proposed 2D fractals acoustic metamaterials[89] and 3D labyrinthine fractal acoustic metamaterials [66], which can possess multi-band sound blocking properties in the low frequency domain. Another broadband low frequency sound isolator is designed through a spider web-inspired membrane-type meta-material [90]. Researchers may seek to find the lightweight structures of different material designs to possess excellent sound absorption to solve challenges related to noise control[91],[92],. Further, it has long been a challenge to get broadband sound absorption while keeping thin and light weightedness as structural properties. Metamaterial design like multi-coiled structures [93], can achieve perfect absorption at extreme low frequency of 50 Hz with a thickness of 1.3 but cannot tune once it is fabricated. Researchers have also tried conventional micro-perforated panels(MPP) [94],[95],[96],[97],

with back cavity, Cascade neck-embedded Helmholtz resonators based metamaterials[98], MPP with neck-embedded Helmholtz resonator[99], and successfully achieved an overall good sound absorption level at low frequencies. However, the thickness of the backing cavity is usually more than 5cm for obtaining a broadband sound absorption behavior. Ultrathin membrane metamaterials (MM) [100],[101], are a very good candidate for broadband sound absorption behavior but the problem in MM is membrane loosening effect which may come in due course of time after repeated use.

This article has developed a new type of tunable micro-perforated face-sheet design (with perforation diameter $\leq$ 1mm) backed up by fractal geometry as shown in Figure 4.1, of subwavelength dimensions that demonstrate excellent broadband sound absorption behavior. The thickness of this classical metamaterial design is less than 2cm, and it can be easily programmed/ tuned according to the industrial need and scope in different fields.

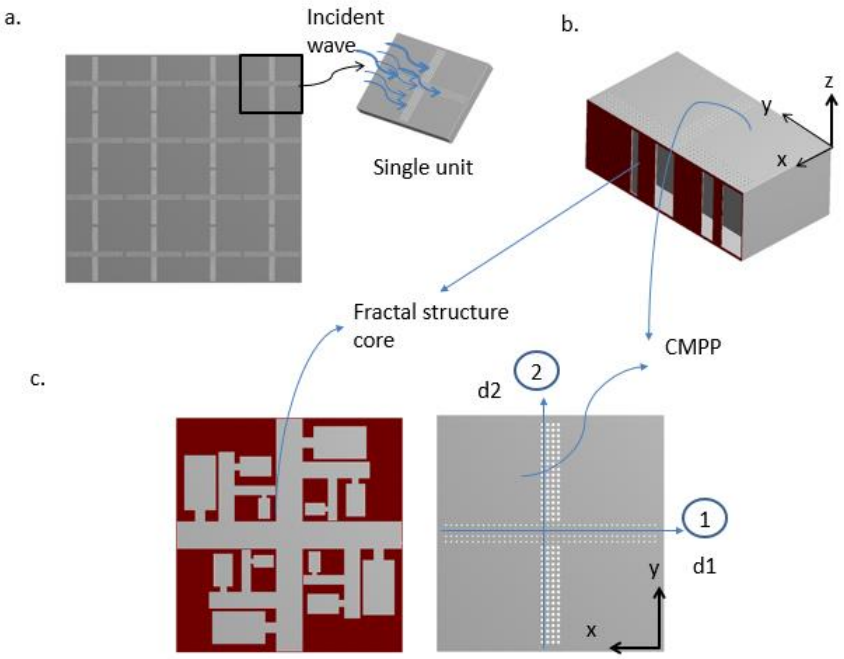

Figure 4.1: (a) Schematic of cross perforated fractal structure hybrid metamaterials panel composed of a cross-micro-perforated top face-sheet, a Helmholtz swastika fractals structure as core, and a back plate as bottom face-sheet. (b) One unit cell, sidewall cut-off vertically to see details inside. (c) CMPP with different perforation sizes in direction one having perforation diameter d1 and direction two is d2 and the back fractals cavity. Courtesy (ANSYS 17.0[45])

The series-parallel circuit analogy is applied to obtain an equivalent impedance method through which a theory to calculate the sound absorption coefficient is established for this new class of fractal designs. This works also experimentally validates and compares with the theoretical model and a finite element model. Perfect sound absorption is achieved around 1000 Hz, together with broadband sound absorption starting from 400~1600Hz, when the thickness of these unique metamaterials is about 20mm. Almost perfect sound absorption has been found around 1000Hz, together with one-octave relative absorption bandwidth starting from 800Hz, when the thickness of the metamaterials is just 20mm with the integration of two-

unit cells. We have also integrated the four-unit cells to achieve broadband sound absorption and successfully achieved 61% higher relative bandwidth and sound absorption coefficient greater than 80%.

4.2 Theoretical Model

The proposed acoustic metamaterial having two face-sheet and a swastika fractal structure core, as shown in Fig. 4.1. The top face-sheet consist of cross perforation having uniform perforation diameter in direction '1' (d_1) and direction '2' as (d_2), in a micro-perforated panel (CMPP). The unique Helmholtz resonator are fractally distributed and act as an acoustic cavity core with the bottom face-sheet in the shape of a rigid backing plate. The fractal core is designed based on novel fractal (卐) shapes and contains multiple Helmholtz resonators along the arms of the fractal shape. In the first level branches, the unit shape (side branched Helmholtz resonator) is rotated by $90°, 180°\ and\ 270°$ respectively to create four arms of the fractal structure and interconnected in a crossroad like manner. As the Helmholtz arm iterates 'n' times to a scaled down geometry connected to the base arm (Helmholtz resonators) at every 90 deg. Rotation angle a scale factor of 0.6 is used for every iteration. The final acoustic meta-structure up to which we investigate corresponds to an "n" value of 3 and the final core structure shown in Fig 4.1 (c).

In general, the absorption coefficient of any acoustic metamaterials with a rigidly backed panel can be estimated through its impedance as

$$\propto = 1 - \left| \frac{{z_s}/{z_0} - 1}{{z_s}/{z_0} + 1} \right|^2 \tag{4.1}$$

where, z_s is known as the surface impedance of the acoustic absorber. $z_0 = \rho_0 c_0$ is the characteristic impedance where ρ_0 and c_0 are mass density and sound speed in air, respectively. The surface impedance of the proposed fractal CMPP have been calculated as:

$$z_s = z_{Mp} + z_{fc} \tag{4.2}$$

where, z_{Mp} and z_{fc} are the acoustic impedance of the CMPP and the fractal structure containing cavity, respectively.

4.2.1 Impedance of the fractal's cavity

We have first calculated the equivalent impedance of one unit cell of the cavity through an electrical analogy[102] developed as shown in Figure 4.2 (c).

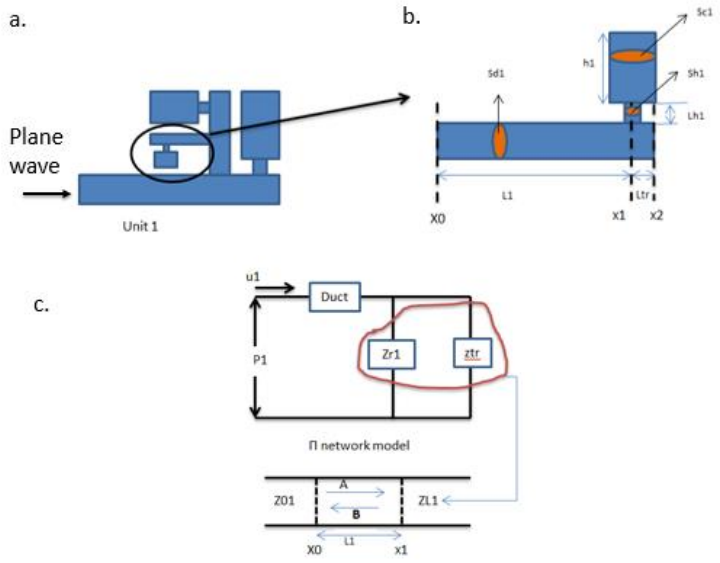

Figure 4.2:(a) One representative branch of the fractal structure core metamaterial which consist of four equal branches. (b) Representative side branch of Helmholtz resonator structure in the fractals. (c) Electrical analogy using network model and their corresponding equivalent impedance

The impedance of the side branch resonator Zr at X_1 as shown in Figure 4.2 (b) ,is expressed as [103],[104],[105]. $zr1$ and $ztr1$ are parallelly connected enabling us to use parallel circuit connection model as below (electrical analogy).

$$\mathrm{Zc1} = \frac{\rho.\,\mathrm{c}}{\mathrm{sc1}} \tag{4.3}$$

$$\mathrm{Zx1} = \frac{\mathrm{zr1}.\,\mathrm{ztr1}}{\mathrm{zr1} + \mathrm{ztr1}} \tag{4.4}$$

$$zr1 = \text{-j.zc1.cot(k.h1)} + Z_h \tag{4.5}$$

$$ztr1 = -j.\,z_{d1}.\cot\,(k.\,Ltr) \tag{4.6}$$

Where $z_{d1} = \rho_0 c_0 / sd1$ characteristics impedance and

$$\mathrm{Zh} = (\frac{\rho.\,c}{sh1})(0.0072 + j.\,k.\,(Lh1 + 0.75) \tag{4.7}$$

Using equations 4.3 to 4.7, we can calculate the impedance of the first side branch Helmholtz resonator [103]

$$\mathrm{Z01} = z_{d1}\frac{\left(\frac{zx1}{zd1}\right) + jtan(k.\,L1)}{1 + j.\left(\frac{zx1}{zd1}\right)\tan\,(k.\,L1)} \tag{4.8}$$

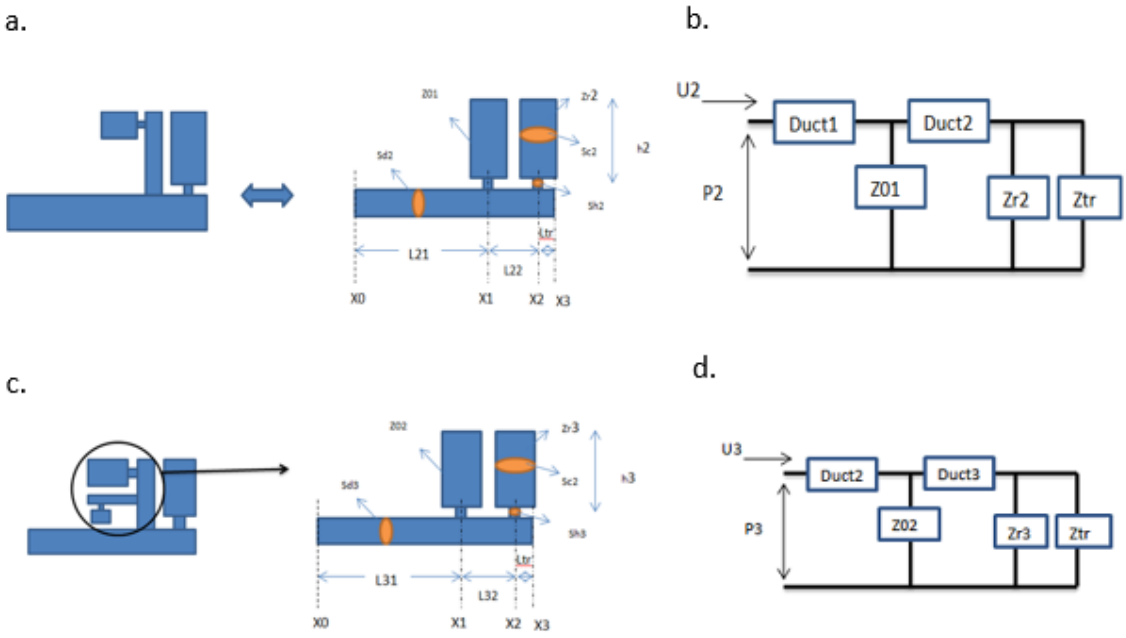

Figure 4.3: (a) Second iteration of fractals geometry and its equivalent side branch resonators model. (b) Electrical analogy or π network model of second iteration. (c) Third iteration of fractals geometry and its equivalent side branch resonators model. (d) cross-ponding Electrical analogy or π network model of the third iteration.

We now calculate the equivalent impedance of the second iteration as shown in fig 4.3 (a, b), with the help of series and parallel electrical circuit analogy and repeat the same procedure as above.

$$\mathrm{Zx2} = \frac{Zr2\,.Ztr2}{Zr2 + Ztr2} \tag{4.9}$$

$$\mathrm{Zx1} = \mathrm{Zd2}\,\frac{\left(\frac{Zx2}{Zd2}\right) + j\,tan(kL22)}{1 + j\left(\frac{Zx2}{Zd2}\right)tan\,(kL22)} \tag{4.10}$$

Where $ztr2 = -j.z_{d2}.\cot(k.Ltr)$ and $z_{d2} = \rho_0 c_0/sd2$

$$Z_{eq} = [\ (1/Z01) + (1/Zx1)]^{-1} \tag{4.11}$$

$$Z02 = Zd2\ \frac{\left(\frac{Zeq}{Zd2}\right) + j\tan(kL21)}{1 + j\left(\frac{Zeq}{Zd2}\right)\tan(kL21)} \tag{4.12}$$

Similarly, we use the same procedure for the third iteration as shown in fig. 4.3 (c, d)

$$Zx2 = \frac{Zr3\ .Ztr3}{Zr3 + Ztr3} \tag{4.13}$$

$$Zx1 = Zd3\ \frac{\left(\frac{Zx2}{Zd3}\right) + j\ tan(kL32)}{1 + j\ \left(\frac{Zx2}{Zd3}\right)tan\ (kL32)} \tag{4.14}$$

Where $ztr3 = -j.z_{d3}.\cot(k.Ltr)$ and $z_{d3} = \rho_0 c_0/sd3$

$$Z_{eq} = [\ (1/Z02) + (1/Zx1)]^{-1} \tag{4.15}$$

Equivalent impedance of the first branch of the fractal acoustic metamaterials as

$$Z03 = Zd2\ \frac{\left(\frac{Zeq}{Zd3}\right) + j\tan(kL31)}{1 + j\left(\frac{Zeq}{Zd3}\right)\tan(kL31)} \tag{4.16}$$

There are 4 identical cavity placed parallelly so the total impedance of the cavity

$$Z_{fc} = \mathrm{Z03/4} \tag{4.17}$$

4.2.2 Impedance of the Cross microperforated plate

Impedance of the micro-perforated plate can be calculated by Maa's Model [106],[107]

MPP impedance

$$z_m = r + j\omega m \tag{4.18}$$

where,

$$r = \frac{32\eta}{\emptyset \rho_0 c_0} \frac{t}{d^2} \left(\sqrt{1 + \frac{x^2}{32}} + \alpha \frac{\sqrt{2}}{8} x \frac{d}{t} \right) \tag{4.19}$$

and

$$m = \frac{t}{\emptyset c_0} \left(1 + \frac{1}{\sqrt{9 + \frac{x^2}{2}}} + 0.85 \alpha \frac{d}{t} \right) \tag{4.20}$$

where $\emptyset$ = Porosity

η = dynamic viscosity

α = perforation constant

d= diameter of hole

t= thickness of the perforated plate

$$x = d\sqrt{\frac{\omega\rho_0}{4\,\eta}}$$

We can now calculate the total impedance of the cross perforated plate of single unit as

$$z_{Mp} = \left(\frac{1}{zm1} + \frac{1}{zm2}\right)^{-1} \tag{4.21}$$

Where $zm1$ is the impedance of the direction 1 and $zm2$ is the impedance of the perforation in direction 2.

We are thus enabled to put the equations 4.21 and 4.17 as inputs to the equation 4.2 and we can thereby theoretically calculate the sound absorption coefficient of the cross micro-perforated fractal acoustic metamaterials with the help of equation 4.1. The absorption coefficient spectrum of the theoretical model is obtained by using MATLAB (R2016a)[46].

Fig. 4.4, depicts the broadband sound absorption in this case. As we can observe clearly that the initial peak of the absorption coefficient of the experimental result is disappeared in the FEM simulation, and the last peak in the theoretical model. Although the experimental, theoretical, and numerical results are overall matching in terms of the amplitude of maximum absorption. In theoretical model, linear superposition principle has been used as shown in equation (8). Thus, the nonlinear coupling effect of perforation and cavity is disappeared in the theoretical spectrum.

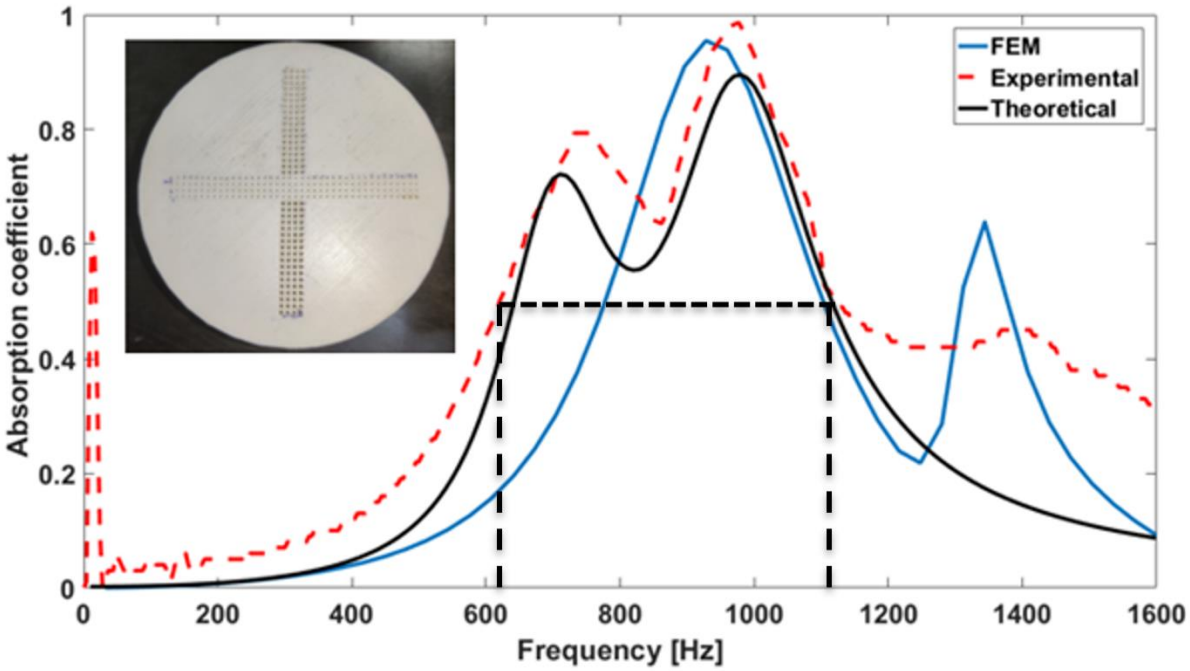

Figure 4.4: Sound absorption coefficient of CMPP predicted by the analytical method, FEM model and Experimental results. *Courtesy (MATLAB R2016a)*[46]

In numerical simulation, MPP converting into porous rigid materials, and considered fractal core as in ideal condition (without visco-thermal losses[108],[109],[110]), thus the first absorption peak shown in simulation results disappear in these conditions. It also observed that the experimental frequency bandwidth is wider than numerical and theoretical prediction due to additional loss of acoustic energy around the rough surface created by 3D printing [111],[112]. A near-perfect absorption peak occurs around 1000Hz with relative bandwidth of 50% for parameters d1=0.5mm and d2=1mm and has a porosity $ø_1$=4.91% and $ø_2$=19.63%, respectively. Here the relative bandwidth is calculated as the ratio of the full width at half the maximum of the absorption coefficient to the resonance frequency. There are two high absorption peaks corresponding to >0.8 absorption coefficient at 700 Hz and >0.95 absorption

coefficient at 1000Hz. The small differences in the results of the FEM and theoretical predictions occur due to neglecting the thermal dissipation at the perforation region and considering only viscous energy dissipation.

4.3 Results

4.3.1 Broadband sound absorption.

We start by varying the thickness of the CMPP fractal acoustic metamaterial to achieve varying sound absorption values in the lower frequency range. Given specific values of fixed cross perforation parameter (d1, d2) and porosity of $\emptyset_1$and $\emptyset_2$ Variable fractal core thickness of 't' the sound absorption bandwidth is obtained at a particular frequency, as shown in fig. 4.5 (a).

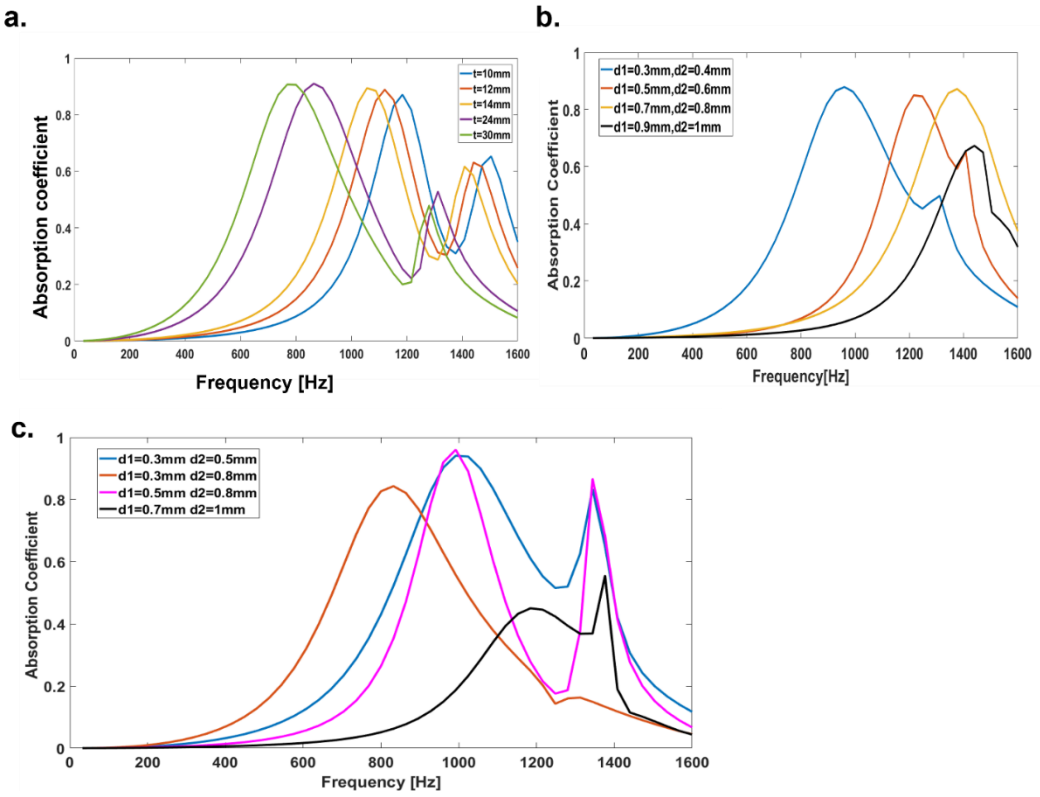

Figure 4.5: Sound absorption coefficient of CMPP with different acoustic parameters (a) Thickness of the fractals core. (b), (c) Porosity of CMPP. Courtesy (MATLAB R2016a)[46]

As the thickness ‘t’ of the fractal core increases, the sound absorption curve gradually shifts from high to low frequency at fixed perforation parameters d1=0.5mm and d2=1mm, respectively. A near-perfect sound absorption peak (96.66%) is obtained at 800 Hz with a relative absorption bandwidth of 50% when t=30mm. Similarly, 95.55% sound absorption at 850 Hz,1150Hz,1100, and 1200Hz with relative bandwidth ($\alpha > 0.5$) of 50% , 30%, 29% and 27.6% is obtained as the thickness “t” becomes =24mm ,14mm,12mm and 10mm respectively.

We have also investigated the effect of cross porosity variation on the broadband sound absorption spectra. In the first sample, A1 we have created a geometry corresponding to d1=0.3mm, $\emptyset_1$=7.07% and d2=0.4mm, $\emptyset_2$=12.56%. Similarly, in the second sample A2, the geometrical parameters are changed to d1=0.5mm, $\emptyset_1$=19.63% and d2=0.6mm, $\emptyset_2$=28.26%, in the third sample A3 the parameters are d1=0.7mm, $\emptyset_1$=38.46% and d2=0.8mm, $\emptyset_2$=50.24%, and in the fourth sample, A4, the parameters are changed to d1=0.9mm, $\emptyset_1$=63.59% and d2=1mm, $\emptyset_2$=78.5% respectively. Further other four samples with different porosity combinations (A5 to A8) with fractals core have been investigated and their acoustic behavior as shown in fig 4.5(c).

The samples are investigated with fixed fractal thickness t=20mm. The sample ‘A1’ shows the maximum sound absorption peak (91.2%) to be at 950Hz with relative bandwidth 58%. Similarly, for the sample A2 and A3 we obtain a similar behavior although as the cross-porosity ratio is increased the resonance frequency is shifted towards the right as shown in fig 4.5 (b). The sample A4 shows a relatively lower value of 65% absorption at the maximum perforation [details shown in table 4.1]. The two samples A1 and A5 shows the higher relative bandwidth of sound absorption with maximum sound absorption of 91% and 95%. So, we can tune the novel sound absorbers with a combination of different cross perforation diameters ($\leq$ 1mm) in

each unit cell. For brevity, we have only shown eight combinations here as shown in fig. 4.5 (b) and 4.5 (c).

Table 4.1: Fractals CMPPs metamaterials parameters and its acoustic absorption behavior of a unit cell

S.no.	Samples	Cross porosity	Frequency at maximum absorption coefficient	Relative bandwidth
1	A1	$\emptyset_1$=7.07%, $\emptyset_2$=12.56%.	@950 Hz (α > 91%)	58%
2	A2	$\emptyset_1$=19.63%,$\emptyset_2$=28.26%	@1200 Hz (α > 90%)	45%
3	A3	$\emptyset_1$=38.46%,$\emptyset_2$=50.24%	@1300 Hz (α > 91%)	50%
4	A4	$\emptyset_1$=63.59%,$\emptyset_2$=78.5%	@1450 (α > 65%)	40%
5	A5	$\emptyset_1$=7.07%,$\emptyset_2$=19.63%	@1000Hz (α > 95%)	60%
6	A6	$\emptyset_1$=7.07%,$\emptyset_2$=50.24%	@800Hz (α > 81%)	37.5%
7	A7	$\emptyset_1$=19.63%,$\emptyset_2$=50.24%	@1000Hz (α > 98%)	25%
8	A8	$\emptyset_1$=38.46%,$\emptyset_2$=78.5%	@1200 Hz (α > 40%)	0%

In order to expand the relative absorption bandwidth, we have further integrated two-unit cells with different cross porosities into one resonator as shown in fig.4.6 (b). Unit 1 and unit 2 have the same thickness and fractals cores but with different top CMPP geometries having perforation diameter d1,d2 of unit 1 and d3 and d4 for unit 2. We have also investigated a core containing a pair of unit cells integrated to CMPP and developed six samples S1,S2,S3,S4,S5 and S6 with different geometrical parameters having various combinations of perforation diameters (d1,d2 and d3, d4) and porosity ratios (φ_1 , φ_2 and φ_3 and φ_4).[Details in Table 4.2]

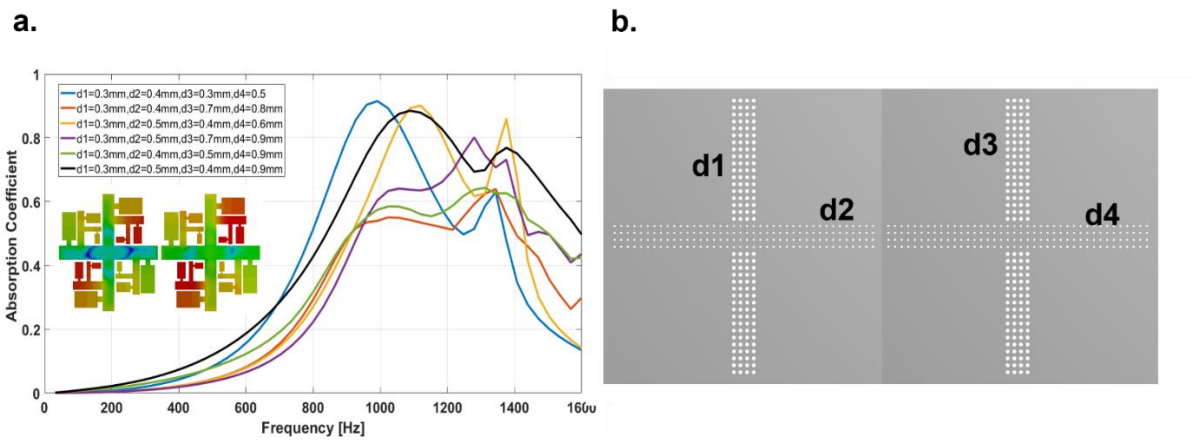

Figure 4.6: Two-unit cells with different cross perforation (a) Sound absorption coefficient of combined two-unit cells with different cross porosity. (b) Top view of the samples of two-unit cells. *Courtesy (ANSYS 17.0[45] and MATLAB R2016a[46])*

Sample S1, shows higher sound absorption coefficient (92%) at 1000 Hz and 60% relative bandwidth, sample S2 has a 76% absorption coefficient with approximately one-octave sound absorption bandwidth, t thickness 20mm as shown in fig.4.6 (a).All the samples show broader relative sound absorption bandwidth within the range 39-76% and the approach shown here demonstrates the ability to customize the sound absorption bandwidth as per requirements by careful consideration of the correct combination of the core with various CMPP geometries.

Table 4.2: Fractals CMPPs metamaterials parameters and its acoustic absorption behavior of a two-unit cells

S.no	Samples	Cross porosity	Frequency at maximum absorption coefficient	Relative bandwidth
1	S1	φ_1=7.07% , φ_2 =12.56 % and φ_3=7.07% and φ_4=19.63	1000Hz (α > 92%)	60%
2	S2	φ_1=7.07% , φ_2 =12.56% and φ_3=38.46% and φ_4=50.24%	1300 Hz (α > 60%)	39%
3	S3	φ_1=7.07% , φ_2 =19.63 %and φ_3=12.56% and φ_4=28.26%	1100 Hz (α > 90%)	47.27%
4	S4	φ_1=7.07% , φ_2 =19.63 %and φ_3=38.46% and φ_4=63.59%	1250 Hz (α = 80%)	40%
5	S5	φ_1=7.07% , φ_2 =12.56 %and φ_3=19.63% and φ_4=63.59%	1250 Hz (α >70%)	41%
6	S6	φ_1=7.07% , φ_2 =19.63 %and φ_3=12.56% and φ_4=63.59%	1050 Hz (α =90%)	76% (800-1600Hz) One octave

We have further integrated 4 different unit cells reported in fig.4.7 (b), to get a broader sound absorption response from these geometries. The porosity of the cross MPPs is optimized numerically to get suitable combinations to achieve a maximized sound absorption bandwidth. The perforation dimensions are d1=0.3mm, d2=0.4mm, d3=0.5mm, d4=0.6mm, d5=0.7mm,d6=0.8mm,d7=0.9mm and d8=1mm.

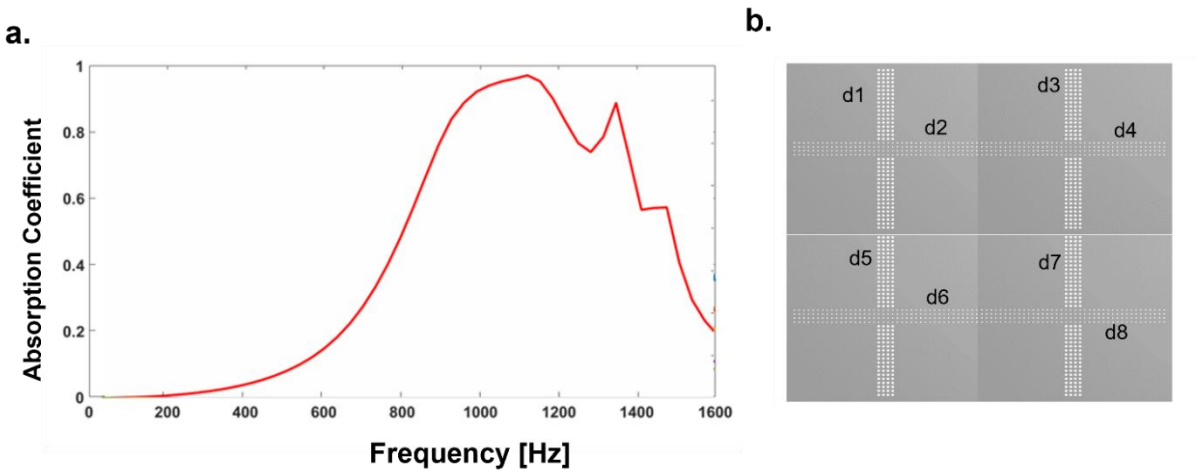

Figure 4.7: Four-unit cells with different cross perforation (a) Sound absorption coefficient of combined four-unit cells with different cross porosity. (b) Top view of the samples of four-unit cells. Courtesy (ANSYS 17.0[45] and MATLAB R2016a[46])

As we can see from the fig. 4.7 (a) that the sound absorption bandwidth from 800-1400Hz demonstrates an absorption coefficient of greater than 80% and the average relative bandwidth of 61%.

4.4 Discussion

Effective and efficient Attenuation of noise requires limited thickness, light weightiness and perfect sound absorption performance in broadband frequencies, especially in the lower frequency range. We have proposed a novel class of cross micro-perforated hybrid acoustic metamaterial with Helmholtz fractal cores that possess outstanding sound absorption over broadband low frequency range with excellent tunability. Using electrical analogy methods the equivalent impedance to sound propagation within the fractal core is evaluated in combination with the classical improved Maa Model [94],for the CMPPs. We have developed a theoretical approach to calculate the equivalent sound absorption coefficient for a bunch of geometric

combinations. This theory is then validated through a numerical approach (FEM) as well as experimentally. The results show that novel sound absorbers 20mm thickness can achieve near perfect absorption around 1000Hz, with a broadband absorption bandwidth. Approximately 1 octave band sound absorption coefficient > 0.5 have been achieved with single unit cell and more than 0.8 has been achieved within the frequency range 700~1100Hz. Maximum relative sound absorption bandwidth of 76% has been achieved with an integrated two unit cell configuration and 61% with 4 unit cell combination. The sound absorption coefficient have been increased by integrating the unit cells.

4.5 Methods

4.5.1 Numerical Simulations

The sound absorption coefficient of CMPP is carried out using ANSYS 17, [113] with its acoustic module. We have approached the problem by first converting the MPPs into rigid porous materials and used equivalent fluid model in numerical analysis FEM simulation to obtain the final estimate [Figure 4.8]. The equivalent fluid CAD model of CMPPs as shown in fig.4.9(b).

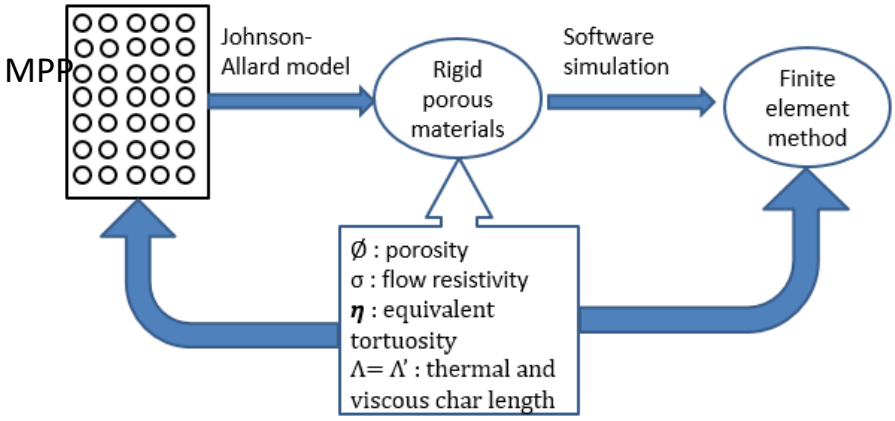

Figure 4.8:Equivalent fluid model conversion of MPP to rigid porous materials using the parameters of Ø, σ, $\boldsymbol{\eta}$, Λ and Λ'.

The equivalent fluid model is defined with the parameters that can be calculated by the equations below. These calculated values have been used in FEM simulations as shown in Figure 4.9 below.

$$\Lambda = \Lambda' = \frac{d}{2} \tag{4.20}$$

$$\sigma = {}^{32\tau}/_{\emptyset d^2} \tag{4.21}$$

where τ is dynamic viscosity and d is the diameter of the perforation.

$$\eta = 1 + \frac{2 * 0.48\sqrt{\pi r^2}(1 - 1.14\sqrt{\emptyset})}{t} \tag{4.22}$$

where r is the radius of the perforation and t is the thickness of the CMPP.

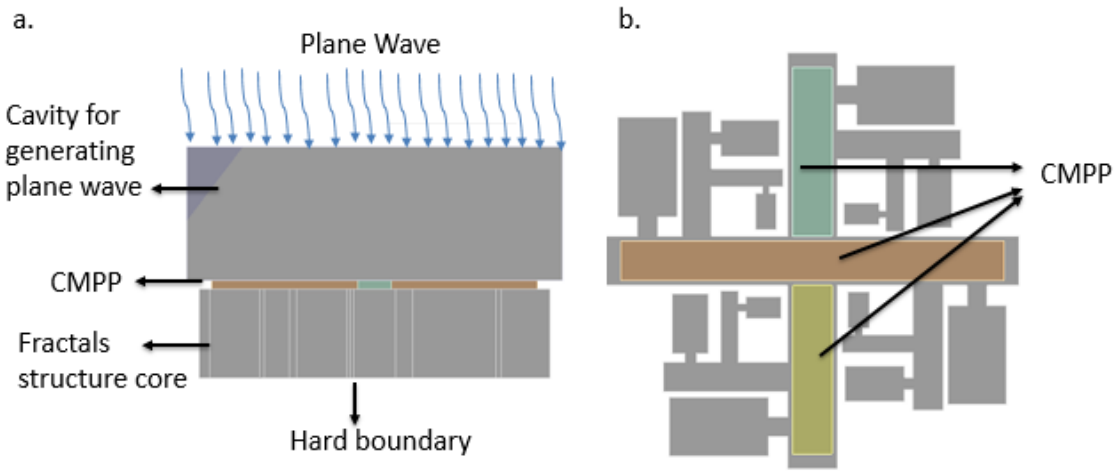

Figure 4.9: FEM simulation setup to analyze the sound absorption coefficient. (a) Simulation setup. (b) Equivalent fluid model of proposed CMPP fractals acoustic metamaterials.

The 3D model of CMPP acoustic metamaterials shown in fig. 4.9 (a) created in the DesignModeler of ANSYS 17.0.[45] A plane wave with unit amplitude is applied normally and hard boundary conditions is applied on all the walls of the interface between air and the surface at the subsurface levels of the structure.

4.6 Conclusion

The proposed work enumerates a hybrid thin, deep-subwavelength (2 cm) acoustic metamaterials acting as a completely new type of sound absorber, showing multiple broadband sound absorption effects. Based on the fractal distribution of Helmholtz resonator (HRs) structures, integrated with careful design and construct hybrid cross micro-perforated panel (CMPP) that demonstrate broad banding approximately one-octave low-frequency sound absorption behavior. To determine the sound absorption coefficient of this novel type of metamaterial, the equivalent impedance model for the fractal cavity and the micro-perforated Maa's model for CMPP are both used. We validate these novel material designs through

numerical, theoretical, and experimental data. It is demonstrated that the material design possesses superior sound absorption which is primarily due to the frictional losses of the structure imposed on acoustic wave energy. The peaks of different sound absorption phenomena show tunability by adjusting the geometric parameters of the fractal structures like cavity thickness '*t*', cross perforation diameter of micro perforated panel, etc. The fractal structures and their perforation panel are optimized dimensionally for maximum broadband sound absorption which is estimated numerically. This new kind of fractals cavity integrated with CMPP acoustic metamaterial has many applications as in multiple functional materials with broad-band absorption behavior etc.

Data Availability

The datasets generated during and/or analyzed during the current study are available from the corresponding author on reasonable request.

Code Availability

The FEM simulations were performed using ANSYS 17(Academic)[45] and for plotting of all the graph, and theoretical coding, used MATLAB (R2016a)[46] (License no. 40765629). The code is available from (bhattacs@iitk.ac.in) on reasonable request

Chapter 5 : Design and development of one dimensional acoustic ventilated metamaterial

5.1 Abstract

The recent emergence of acoustic metamaterials presents unparalleled possibilities for sound control across diverse scenarios. However, achieving both broadband sound absorption and unrestricted airflow concurrently in a one-dimensional scenario poses a challenge. In many scenarios there is an acute need to naturally ventilate spaces and structures to make them livable. Acoustic solutions which promote ventilation through intelligent design leading to attenuation/ confinement of acoustic signals within designated places are a critical need of the industry. In response to this design challenge, we present a subwavelength (7 cm) one-dimensional acoustic meta-structured blanket, demonstrating broadband sound absorption bandwidth of one octave with 0.5-0.9 absorption within the 500-1600Hz range. In this study, we theoretically (through transfer matrix method), numerically (through FEM), and experimentally (through Impedance tube method) have showcased that this challenge can be surmounted by employing various configurations of kink fiber-based metamaterials. Broadband absorption has been obtained by dissipating incident propagating sound waves inside an array of kinked hollow fibers with differently configured unit cells making up the meta-structure. Additionally, the meta-structures' simple distinctive design enables a simultaneous air circulation promoting natural ventilation and sound absorption at the same time. Whereas simultaneous natural ventilation and noise mitigation are very important features which have been integrated into the same architecture, the proposed novel solution may find use in a lot of architectural acoustic modulation related to building spaces. Following

the concept developed in this article there has been efforts to develop blankets using hand layup method which can be deployed in real world setup based on one-dimensional acoustic damping concept introduced in this work.

5.2 Introduction

Acoustic metamaterials have advanced quickly over the past 20 years in a variety of domains, including acoustic cloaking,[114],[115] subwavelength imaging,[116],[117] topological acoustics,[118],[119], and sound insulation and absorption,[21],[59],[120] offering hitherto unheard of means of controlling sound waves, which have essential theoretical and practical values.[121],[122] However, free fluids like air cannot be used with these acoustic metamaterials. Another significant issue in acoustic engineering is acoustic absorption and insulation by acoustic metamaterials in vented structures. This issue has numerous potential applications in real-world settings, including noise control for air conditioners, cars, and building ventilating ducts etc. Acoustic metamaterials [123],[124],[125],[126],[127],[128] synthetic subwavelength unit structures having dynamical features not found in nature, have been used to design acoustic insulation ventilated channels (AIVC) in earlier research. Additionally, the vast majority of acoustic metamaterials with air circulation developed and demonstrated during the past years have two dimensional meta-surface geometries [37],[129],[130] and three dimensional.[131],[132] Most of the sound is reflected back by these metamaterials, not all the sound passes through, which is their fundamental flaw. Additionally, it is a constant goal to simultaneously attenuate noise and provide ventilation in a variety of locations, including stations, cabins for large machines, and buildings. However, sound-insulating effectiveness and ventilation capacities have always had to be compromised when creating conventional acoustic barriers.[133],[134],[135] To address these issues, one-

dimension acoustic ventilated metamaterials absorber (ODVAM) is proposed and experimentally and numerically demonstrated.

5.3 Design strategies

In this chapter, we present a vented metamaterial absorber (ODVMA) that can absorb incident energy with great efficiency (>80%). The ODVMA, as its name suggests, does not require any reflectors, allowing fluids to flow in both directions. Additionally, the ODVMA can operate in both waveguides and free space, opening up a multitude of operational possibilities. We firstly propose a fabrication method to realize the ventilated panel and then numerically and experimentally investigate the acoustic behavior of the proposed metamaterial. As depicted in fig.5.1(a), shows the fabrication method (Hand layup method) to designed ODVAM panel. The glass hollow tube placed on the glass mat with adhesive in x direction as shown in fig 5.1(a) and the gap is filled with the adhesive. This process is repeated in y direction with several layers of glass fiber mat and hollow fiberglass insulation sleeves to get the ventilated panel as shown in fig 5.1(b). The hollow glass fiber permits the flow of air passing through the absorber as well absorb the sound as shown in fig.5.1(c).

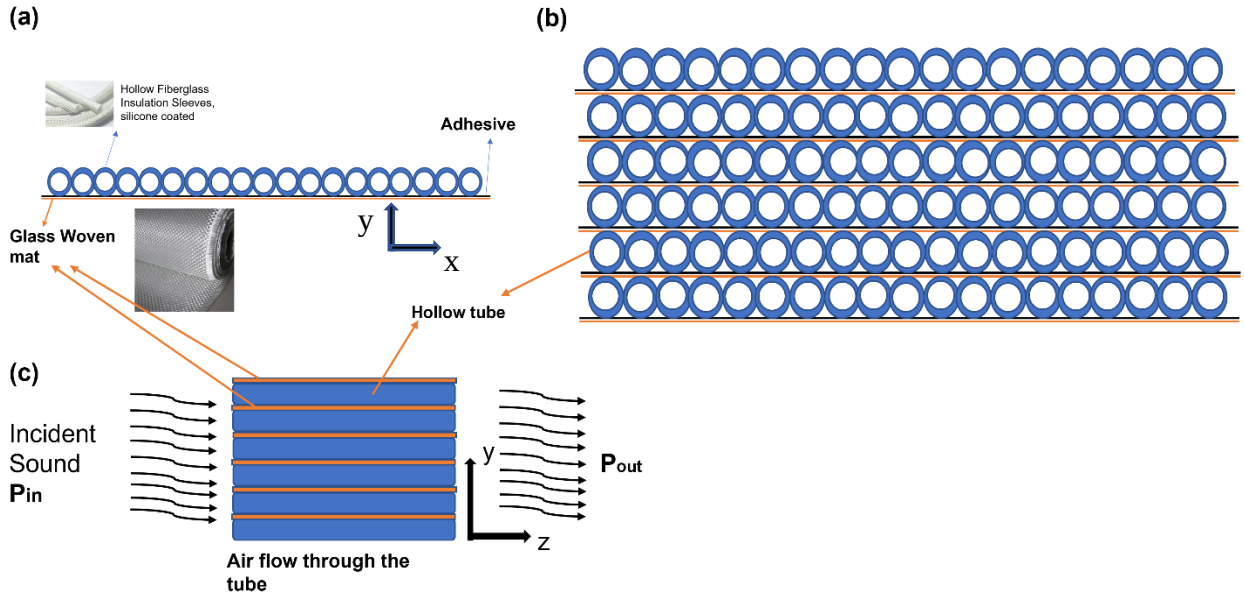

Figure 5.1:(a) Fabrication process and materials use for designing one dimensional ventilated metamaterial. (b) Proposed acoustic ventilated panel. (c) The schematic diagram of the ventilation and sound insulation of ODVAM.

Now we proposed five different kinds of hollow glass fiber tube unit cell to design and developed the ODVAM panel. The geometric parameters for the ventilated panel as shown in Table1. The length of each tube is 7cm. The first sample (A) is built entirely of glass mat, which restricts the panel's ability to breathe freely. The sample (B) made of the hollow straight fiber that allow to flow air freely. Sample (C), (D), (E)and (F) is fabricated with different kink design at the center to shift the absorption peak toward left and allow air to flow through. The kinking diameter of the unit cell (C), (D) and (E) is around 0.5 and for sample (F) is around 1mm.

Table 5.1:Geometric parameter of the all the unit cell of the proposed ODVAM.

Sample No.	Name of the unit Cell	Design strategy of unit cell
(A)	GMM (Glass Woven Mat)	 The thickness of mat (t) = 0.2mm
(B)	SHF (Straight Silicon Hollow Fiber)	 D=1mm
(C)	KF (Kink Fiber)	 D=1mm D=0.5 D=1mm
(D)	YAM (“Y” Type kink Fiber)	 D1=2m D=0.5 D2 and D3=1mm
(E)	CDAM (Converging Diverging Kink Fiber)	 D1=2m D=0.5 D2=1m
(F)	IRAM (Internal Resonator Kink Fiber)	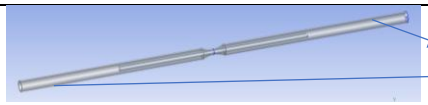 D1=D2=2m 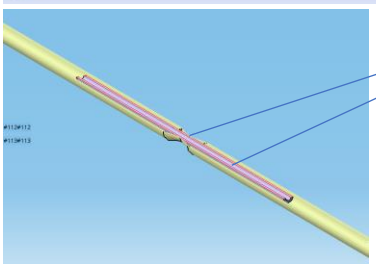 Internal straight resonator having D= 1mm (kinking dia.=1mm)

For the acoustic impedance tube test, we made a sample as per circular impedance tube standard. The dimeter of each sample is 100mm and length is 7cm. The different kinking hollow fibers are fabricated by using silicone coated fiberglass sleeve and the heat shrinking tube made up of thermoplastic (Polyethylene terephthalate (PET)) that shrinks when exposed to heat. Shrinking temperature is approximately $70℃(158°F) - 190℃(374°F)$ and density 1.38 g/cm^3.The fabrication process of the sample as shown in fig.5.2(a). In order to experimentally verify the acoustic performance of the proposed concept in term of sound attenuation, an experimental sample is fabricated as shown in Figure 5.2(b). The outer cylinder case is fabricated by using 3D printer using PLA, with the accuracy of 0.1mm. The sample has kink channels and a circular cross section, designed as a ventilation structure with a diameter of 10 cm, which is in accordance with the size of a typical acoustic impedance tube.

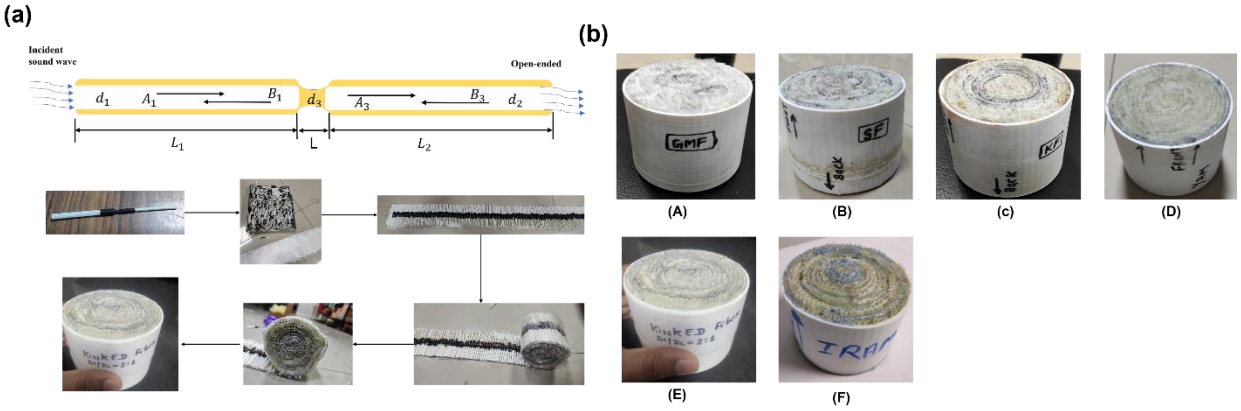

Figure 5.2: (a)The sample fabrication hand layup method, the dimension of the kink dia. approximately d1=0.5 to 1mm, L1 and L2 =35mm. (b) Created samples for acoustic impedance testing.

5.4 Theoretical modeling

The kink channels are greatly improving the sound insulation performance of the structure, while retaining the opening part to ensure its ventilation performance. The resonance frequency of the channel's length determines the first-order resonance frequency, and their relationship can be defined as follows[16]:

$$f_i = {}^{c_0}/_{4L_i} \tag{5.1}$$

$$L_i = L_T + 0.6\,D \;\; (as\ long\ as\ \lambda \gg D\ ) \tag{5.2}$$

The equation (5.1) is valid for the unform cross section open tube geometries, where c_0 is the speed of sound in the air, $L_i$is the effective length of the tube, L_T is the total length of the tube, f_i is the resonance frequency corresponding to the tube length and D is the diameter of the uniform pipe.And the first fundamental frequency of the straight hollow fiber from the equation (5.1) is $f_1 = 1193.4Hz$ .Particularly at resonant frequencies, thermal viscous effects in the channels need to be considered. The channel's attenuation coefficient α is provided by (5.3) [16]

$$\alpha \approx \frac{1}{dc_0}\sqrt{\frac{\mu\omega}{2\rho_0}} \tag{5.3}$$

where ω is the angular frequency, d is the diameter of the hollow pipe, μ and ρ_0 are the viscosity coefficient and mass density of air, respectively. Resonance causes a significant increase in the thermal viscous loss in the channel, and the coupling of these two processes improves the structure's capacity for sound insulation.

The kink hollow fibers are composed of three parts, two identical parts having the length of L_1 and $L_2$and the middle is the kinking having a diameter d_3 as shown in Figure 5.6. An investigation of resonance conditions for pulsating air flow through an aperture in a duct pipe with an orifice of practical length L.

All wavefronts are taken to be planar, and any distortions that may occur as the wavefronts converge or diverge at junctions are disregarded. Displacement at any section:

$$\delta = A_j e^{i(\omega t - kx)} + B_j e^{i(\omega t + kx)} \tag{5.4}$$

And excess pressure:

$$p = ik\rho c^2 (A_j e^{i(\omega t - kx)} + B_j e^{i(\omega t + kx)}) \tag{5.5}$$

where $k = {}^{\omega}/_{c}$ and $\omega = 2\pi f$

Boundary conditions: at x=0, $l = L_1 + L + L_2$, for complete reflection at the open end, excess pressure is zero. At x=L_1,($L_1 + L$), there is a continuity of excess pressure and volume displacement.

The following equations, with complex coefficients to allow for any phase shifts, can be obtained from the aforementioned conditions:

$$A_1 = -B_1 \text{ , @ (x=0)} \tag{5.6}$$

$$A_3 = -e^{2ikl} B_3 \text{ ,@ (} l = L_1 + L + L_2) \tag{5.7}$$

$$A_1 e^{-ikL_1} + B_1 e^{ikL_1} = A_2 e^{-ikL_1} + B_2 e^{ikL_1}\text{, @ (X=}L_1\text{)} \tag{5.8}$$

$$A_1 e^{-ikL_1} - B_1 e^{ikL_1} = m1(A_2 e^{-ikL_1} - B_2 e^{ikL_1} \text{ ,}$$

$$\text{(Where } m1 = {}^{d_3{}^2}\Big/_{d_1{}^2}\text{) (area ratio)} \tag{5.9}$$

$$A_2 e^{-ik(L_1+L)} + B_2 e^{ik(L_1+L)} = A_3 e^{-ik(L_1+L)} + B_3 e^{ik(L_1+L)}\ , \qquad (5.10)$$

$$(\text{x}=L_1 + L)$$

$$m2\left(A_2 e^{-ik(L_1+L)} - B_2 e^{ik(L_1+L)}\right) = A_3 e^{-ik(L_1+L)} - B_3 e^{ik(L_1+L)}, \qquad (5.11)$$

$$(\text{Where } m1 = {d_3}^2 \Big/ {d_2}^2)$$

For m1=m2 =m

here we use k=K_d to include the viscus thermal loss

After manipulation of the above equation

$$\frac{A_1}{A_3} = \frac{e^{-iK_d L_1}\left(\left(1 - e^{-2iK_d L_2}\right) + \dfrac{1 + e^{-2iK_d L_2}}{m}\right)}{\left(\left(e^{-iK_d L_1} - e^{iK_d L_1}\right) + \dfrac{e^{-iK_d L_1} + e^{iK_d L_1}}{m}\right)} \qquad (5.12)$$

The modulus $\left|A_1 / A_3\right|$ is referred to as the sound absorption coefficient. The following equation can be derived to get the resonance frequency of the kink hollow fiber.

$$m \tan K_d L_1 + \tan K_d L + m \tan K_d L_2 - m^2 \tan K_d L_1 \times \tan K_d L \times \tan K_d L_2 = 0 \qquad (5.13)$$

And solving for k =$2\pi f/c$, we can calculate the fundamental resonance frequency.

The first fundamental frequency of kink fiber calculated from the equation (5.13) is around f_{K1} =995.23 Hz. Over time, it has been noted that thermo-viscous boundary layer effects can have a major impact on the propagation of sound along small, rigid-walled channels, giving air substantial acoustic absorption in the audio frequency range.

5.4.1 Visco-thermal losses inside the tube

When a plane wave travels through a pipe/duct having uniform cross section, the complex frequency dependent density and bulk modulus are evaluated to account for viscothermal losses in the pipe. [136] In the case of an r-radius circular duct:

The equivalent complex density ρ_d and equivalent bulk modulus K_d of the central through-hole air can be expressed as [47]

$$\rho_d = \rho_0 \left[1 - \frac{2}{rG_p}\frac{J_1(rG_p)}{J_0(rG_p)}\right] \tag{5.14}$$

$$K_d = k_0 \left[1 - \frac{2(\gamma-1)}{rG_k}\frac{J_1(rG_k)}{J_0(rG_k)}\right] \tag{5.15}$$

where $G_p = \sqrt{\frac{-i\omega\rho_0}{\tau}}$, $G_k = \sqrt{\frac{-i\omega p_r\rho_0}{\tau}}$, and the air bulk modulus $k_0 = \gamma p_0$. r is the radius of the pipe,J_n is the Bessel function of the first kind and order n. The normalized acoustic impedance is given by $z_f{}' = \sqrt{K_d\rho_d}\Big/_{\pi r^2}$

The medium is air with mass density $\rho_0 =$ 1.213kg/m3, sound speed $c_0 =$ 343 m/s, atmospheric pressure p_0 =101 325 Pa, dynamic viscosity τ =1.79 × 10−5 kg/(m · s), specific heat ratio $\gamma =$ 1.4, Prandtl number Pr =0.7167.

5.4.2 The Transfer Matrix Method (TMM)

The transfer matrix method (TMM) shows the relationship between the initial sound pressure “p” and the volume flow rate V. Assuming that the wave flowing inside the tube is the plane

wave and according to the continuity boundary conditions of sound pressure and velocity flux, we can get

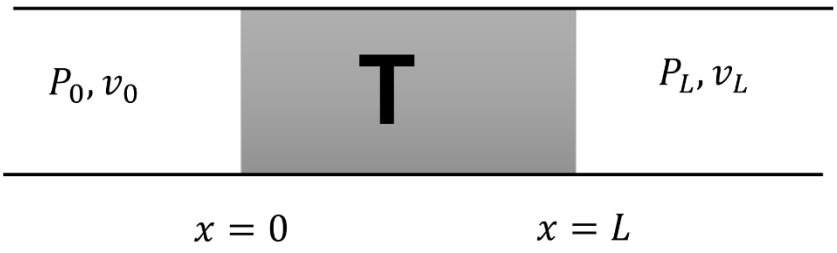

Figure 5.3: Schematic diagram of hollow glass fibre.

$$\begin{bmatrix} p \\ v \end{bmatrix}_{x=0} = T \begin{bmatrix} p \\ v \end{bmatrix}_{x=L} = \begin{bmatrix} T_{11} & T_{12} \\ T_{21} & T_{22} \end{bmatrix} \begin{bmatrix} p \\ v \end{bmatrix}_{x=L} \tag{5.16}$$

Where T is the system transfer matrix.

5.4.2.1 Obtained the acoustic properties of straight, kink and IRAM fiber using the TMM.

Straight hollow fiber

Figure 5.4: Schematic diagram of hollow glass fibre

The hollow glass fibers are shown in fig.5.4. The sound wave incident at one end flows through the pipe and comes out from the second end. The transfer matrix of the hollow pipe

$$T = \begin{bmatrix} \cos(K_d L) & i z_f{}' \sin(K_d L) \\ i \frac{1}{z_f{}'} \sin(K_d L) & \cos(K_d L) \end{bmatrix} \tag{5.17}$$

The pipe is surrounded by air on both sides. Then, the acoustic impedance at both of the end is $Z_0 = \rho_0 c_0$. S is the cross-section area of the pipe, and the normalized acoustic impedance is given by $z_f{}' = \sqrt{K_d \rho_d} \Big/ \pi r^2$

The transmission coefficient is given by[137]

$$Trs = \frac{2e^{iK_d L}}{T_{11} + \frac{T_{12}}{Z_0} + T_{21} Z_0 + T_{22}} \tag{5.18}$$

$$R = \frac{T_{11} + \frac{T_{12}}{Z_0} - T_{21} Z_0 - T_{22}}{T_{11} + \frac{T_{12}}{Z_0} + T_{21} Z_0 + T_{22}} \tag{5.19}$$

The absorption coefficient can be calculated as

$$\alpha = 1 - |R|^2 - |Trs|^2 \tag{5.20}$$

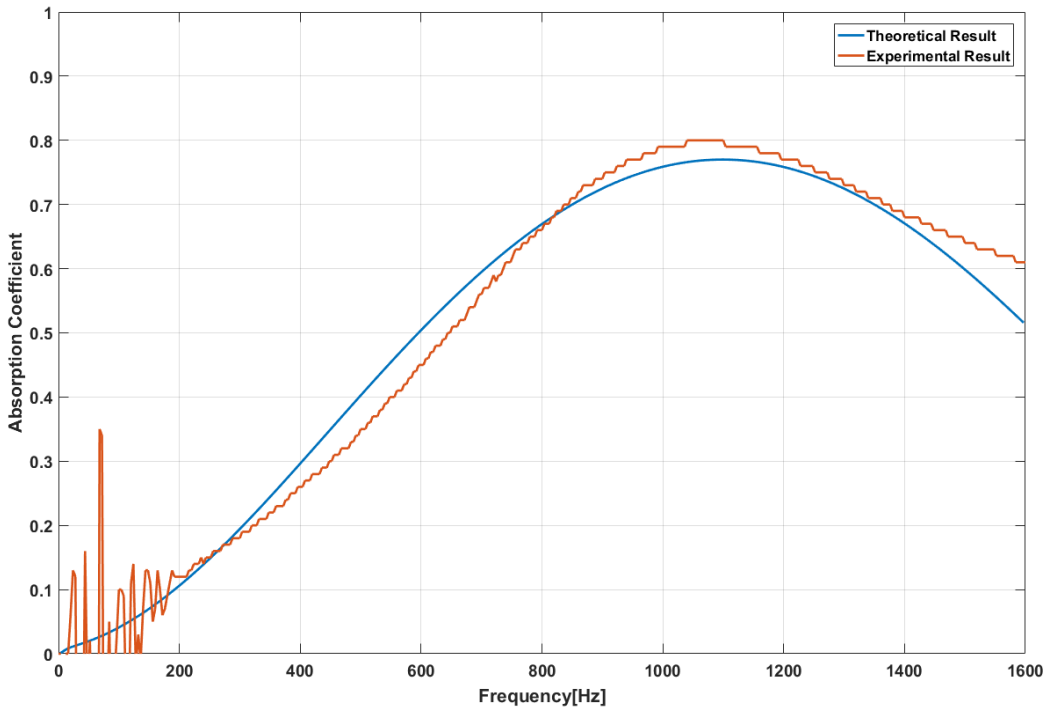

Figure 5.5: Validation of theoretical model with the experimental result of straight hollow fibre.

Kink hollow fiber

The kink hollow fibers are composed of three parts, two identical parts having the length of L_1 and $L_2$and the middle is the kinking having a diameter d_3. An investigation of resonance conditions for pulsating air flow through an aperture in a duct pipe with an orifice of practical length L.

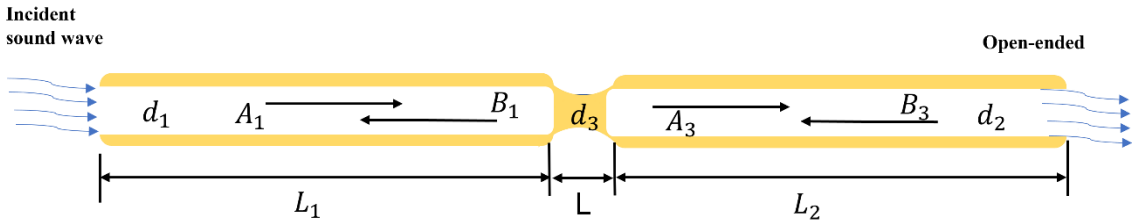

Figure 5.6: Schematic diagram of kink hollow glass fibre

The hollow kink fiber can be divided into a four segments or elements and each element represented by a transfer matrix. Then, the transfer matrix can be combined to obtain the system matrix in order to evaluate the acoustical performance for the hollow tube metamaterial. The Figure 5.7, illustrated the dimensions of the kink fiber and the basic elements, labeled 1-5, indicated by dash line. Elements 1,3 and 5 are simple pipes of constant cross section. Element 2 is an area contraction and element 4 is area expansion with extended outlet pipe.

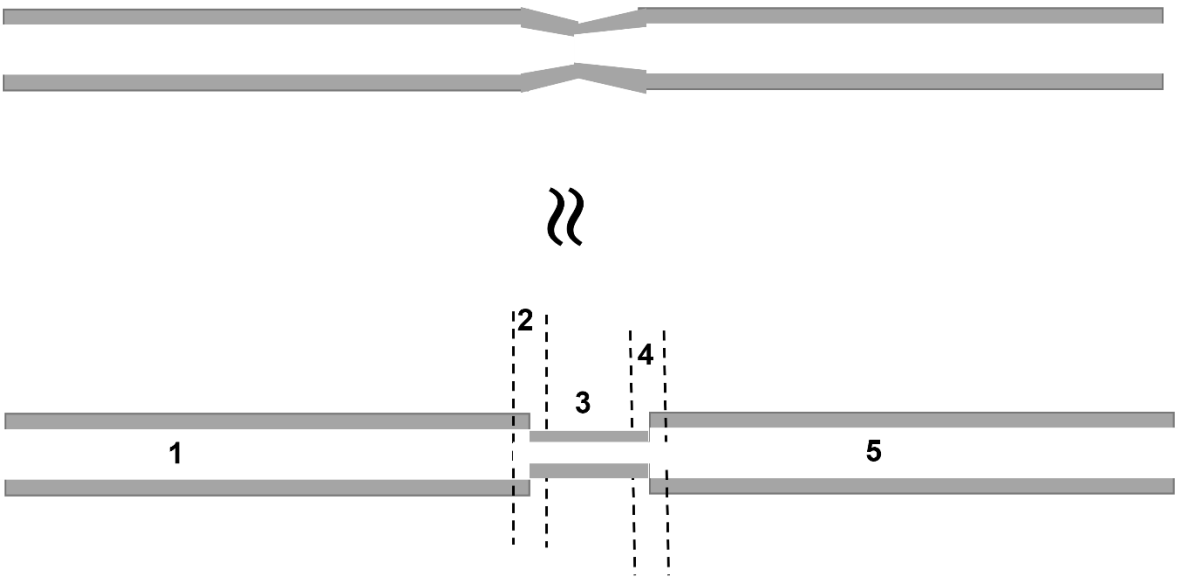

Figure 5.7: kink fiber and its equivalent straight tube combination and it Segmentate into basic element.

The four elements are characterized by the transfer matrix $T^{(1)}$ through $T^{(4)}$, therefore the system matrix $T^{(s)}$ can be obtained by matrix multiplication.

$$\mathrm{T}^{(\mathrm{s})} = \mathrm{T}^{(1)}\mathrm{T}^{(2)}\ \mathrm{T}^{(3)}\mathrm{T}^{(4)}\mathrm{T}^{(5)} \tag{5.21}$$

All wavefronts are taken to be planar, and any distortions that may occur as the wavefronts converge or diverge at junctions are disregarded. Here cross-sectional area of element 1 and 4 is same and it is "s1=s2=s4=s5" and the average or equivalent area is "s3=s=πr_i" where r_i is the radius of the fiber.

The transfer matrix of element 1 ,2,3, and 4 are.

$$T^{(1)} = \begin{bmatrix} \cos(K_d L_1) & i(z_f{}'/\mathrm{S1})\sin(K_d L_1)) \\ i\dfrac{S1}{z_f{}'}\sin(K_d L_1)) & \cos(K_d L_1)) \end{bmatrix} \tag{5.22}$$

$$T^{(2)} = \begin{bmatrix} 1 & 0 \\ 0 & s3/s2 \end{bmatrix} \tag{5.23}$$

$$T^{(3)} = \begin{bmatrix} \cos(K_d L) & i(z_f{}'/\mathrm{S3})\sin(K_d L)) \\ i\dfrac{S3}{z_f{}'}\sin(K_d L)) & \cos(K_d L)) \end{bmatrix} \tag{5.24}$$

$$T^{(4)} = \begin{bmatrix} 1 & 0 \\ 0 & s4/s3 \end{bmatrix} \tag{5.25}$$

$$T^{(5)} = \begin{bmatrix} \cos(K_d L_2) & i(z_f{}'/\mathrm{S5})\sin(K_d L_2)) \\ i\dfrac{S5}{z_f{}'}\sin(K_d L_2)) & \cos(K_d L_2) \end{bmatrix} \tag{5.26}$$

$$T^{(s)} = \begin{bmatrix} T_{11} & T_{12} \\ T_{21} & T_{22} \end{bmatrix} \tag{5.27}$$

Put all the value of transform matrix in the equation 5.21 and we will get.

$$T = \frac{2e^{iK_d L}}{T_{11} + {}^{T_{12}}/_{\rho c} + \rho c T_{21} + T_{22}} \tag{5.28}$$

$$R = \frac{T_{11} + \frac{T_{12}}{\rho c} - \rho c T_{21} - T_{22}}{T_{11} + \frac{T_{12}}{\rho c} + \rho c T_{21} + T_{22}} \tag{5.29}$$

R is the complex acoustic reflection coefficient in the situation. This absorption coefficient can be estimated using hard-backed impedance tubes.

$$\alpha = 1 - |R|^2 - |T|^2 \tag{5.30}$$

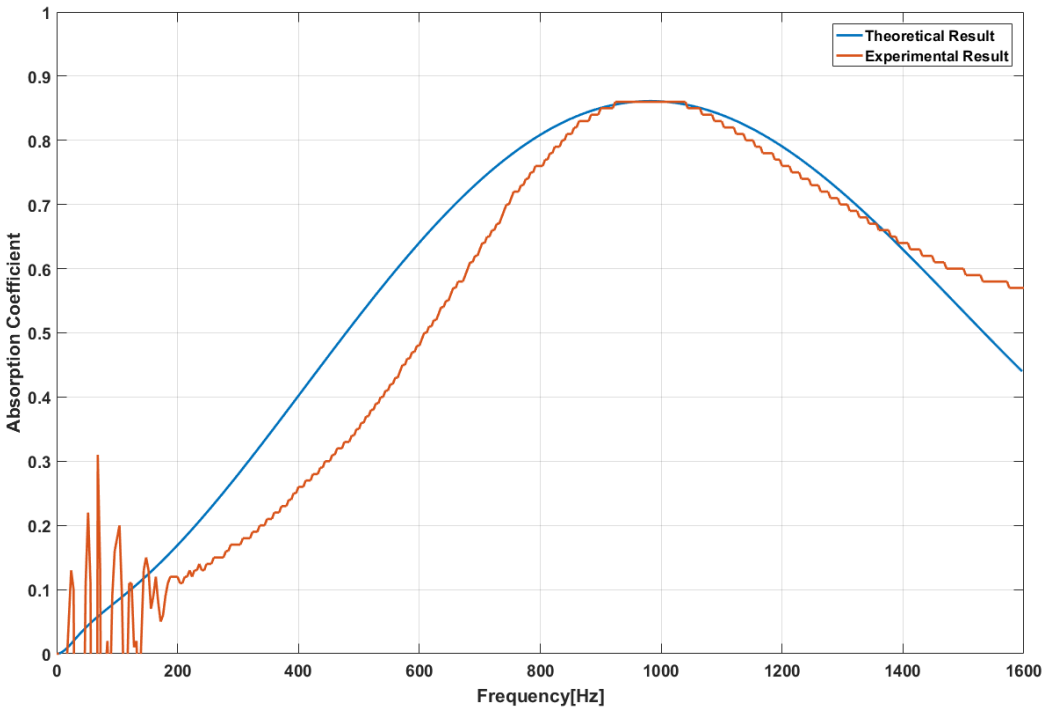

Figure 5.8: Validation of theoretical model (TMM) with the experimental result of kink hollow fibre.

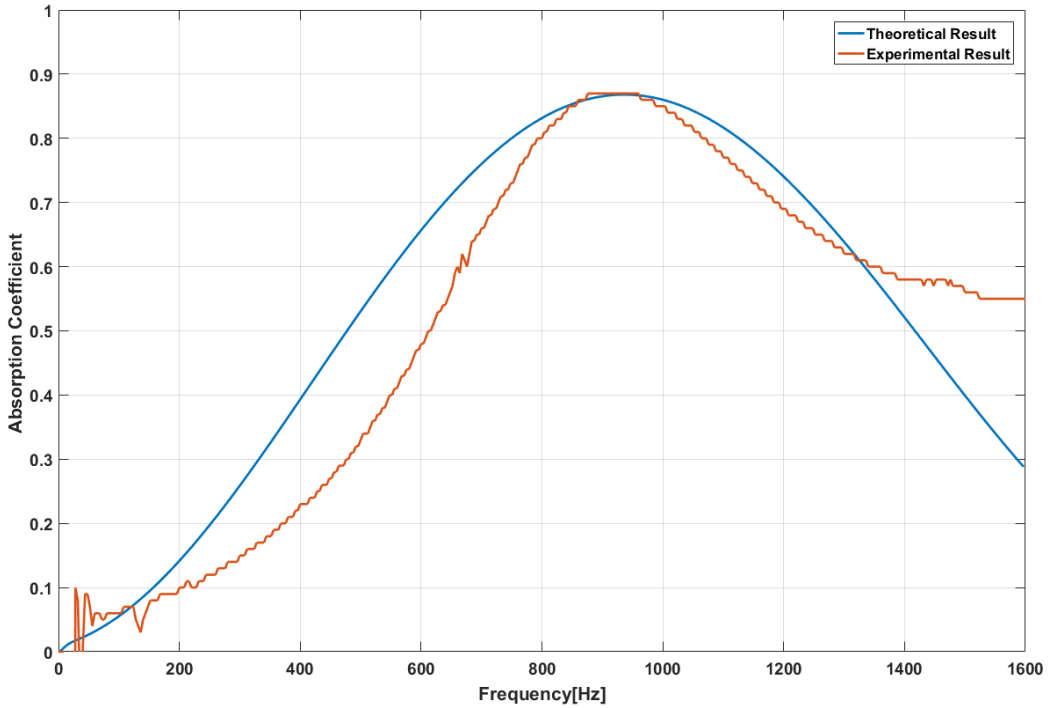

Figure 5.9: Validation of theoretical model (TMM) with the experimental result of CDAM hollow fibre.

IRAM hollow fiber

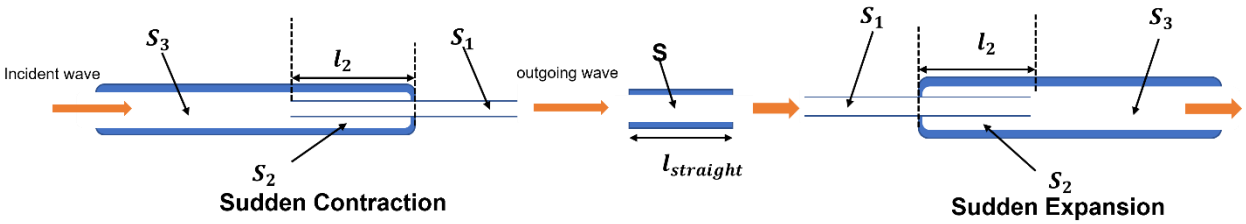

Figure 5.10: Schematic diagram of IRAM hollow glass fiber with section view

The 4-pole transmission matrix for the IRAM can be calculated as the sequence of the segment (starting from the left as shown in Figure 5.10): (1) sudden contraction, (2) straight chamber in the middle, (3) sudden expansion.

The transmission matrix for these expansion and contraction chambers is given by[138]

$$T_i = \begin{bmatrix} 1 & KM_1Y_1 \\ \dfrac{C_2S_2}{C_1S_2Z_2 + S_2M_3Y_3} & \dfrac{C_2S_2Z_2 - M_1Y_1(C_1S_1 + S_3K)}{C_2S_2Z_2 + S_3M_3Y_3} \end{bmatrix} \tag{5.31}$$

$$Z_2 = -j\frac{c}{S_2}\cot K_d l_2 \tag{5.32}$$

$$Y_i = \frac{c}{S_i} \tag{5.33}$$

$$M_i = {}^{V_i}/_{c} \tag{5.34}$$

Table 5.2 :expansion and contraction cross-section parameter

Type	C_1	C_2	K
Expansion	-1	1	$\left(\frac{S_3}{S_1} - 1\right)^2$
Contraction	-1	-1	$\frac{1}{2}\left(1 - \frac{S_1}{S_3}\right)$

where V_i is the mean flow velocity through the cross-section of the area S_i and M_i is the Mach number through cross-section S_i. There is no mean flow ($M_i = 0$). K is the wave number $k = \frac{\omega}{c}$, and the constants C1 and C2 are selected to satisfy the compatibility of the cross-sectional areas across the transition.

Then the equation (5.31) turns out

$$T = \begin{bmatrix} 1 & 0 \\ \frac{C_2}{C_1 Z_2} & 1 \end{bmatrix} \tag{5.35}$$

The 4-pole matrices for each of these segments are,

$$\text{Contraction: } T_1 = \begin{bmatrix} 1 & 0 \\ \frac{S_2}{-jc \cot K_d l_2} & 1 \end{bmatrix} \tag{5.36}$$

$$\text{Straight pipe: } T_2 = \begin{bmatrix} \cos(K_d l_{straight}) & \frac{jc}{s}\sin\left(K_d l_{straight}\right) \\ \frac{js}{c}\sin\left(K_d l_{straight}\right) & \cos(K_d l_{straight}) \end{bmatrix} \tag{5.37}$$

$$\text{Expansion: } T_3 = \begin{bmatrix} 1 & 0 \\ \frac{S_2}{jc \cot K_d l_2} & 1 \end{bmatrix} \tag{5.38}$$

$$T_{IRAM} = T_1\, T_2 T_3 \tag{5.39}$$

$$T_{IRAM} = \begin{bmatrix} T_{11} & T_{12} \\ T_{21} & T_{22} \end{bmatrix} \tag{5.40}$$

Comparing equations (5.39) and (5.40), we can obtain, [139],[140]

$$T = \frac{2e^{iK_d L}}{T_{11} + {T_{12}}/{\rho c} + \rho c T_{21} + T_{22}} \tag{5.41}$$

$$R = \frac{T_{11} + \frac{T_{12}}{\rho c} - \rho c T_{21} - T_{22}}{T_{11} + \frac{T_{12}}{\rho c} + \rho c T_{21} + T_{22}} \tag{5.42}$$

R is the complex acoustic reflection coefficient in the situation. This absorption coefficient can be estimated using hard-backed impedance tubes.

$$\alpha = 1 - |R|^2 - |T|^2 \tag{5.43}$$

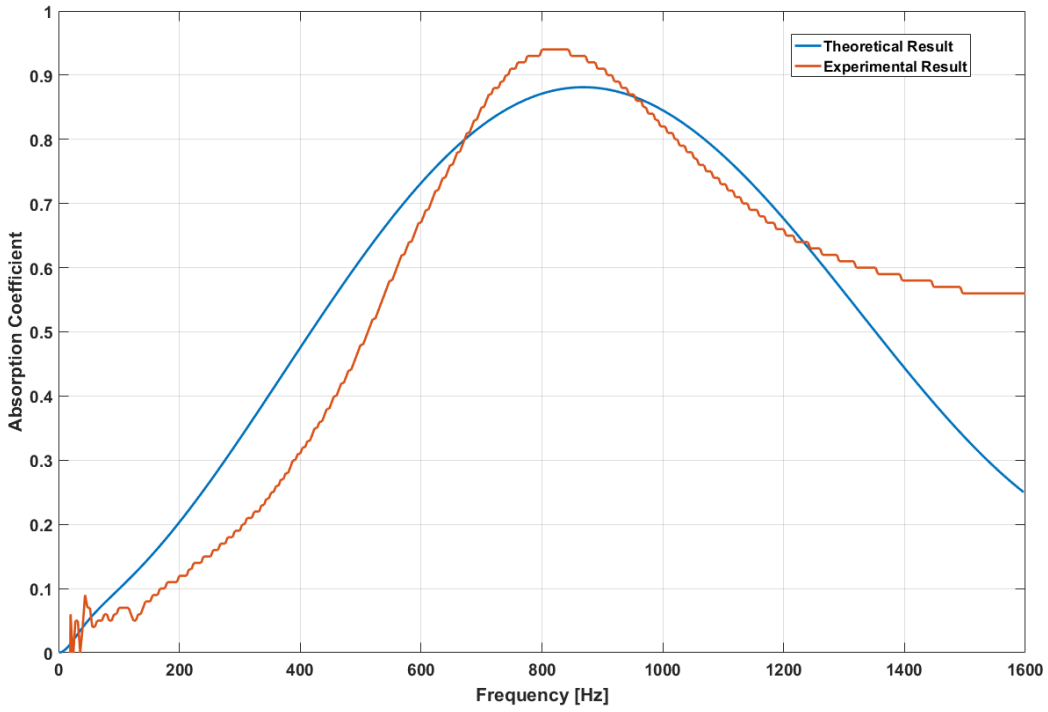

Figure 5.11: Validation of theoretical model (TMM) with the experimental result of IRAM hollow fibre.

5.5 Setup of simulations in ANSYS 2021 R1 Acoustic module

The sound absorption coefficient of ODVAM is carried out using ANSYS 2021 R1, [113] with its acoustic module. The 3D model of ODVAM acoustic metamaterials shown in fig. 3(a). A plane wave with unit amplitude is applied normally and hard boundary conditions is applied on all the walls of the interface between air and the surface at the subsurface levels of the structure.

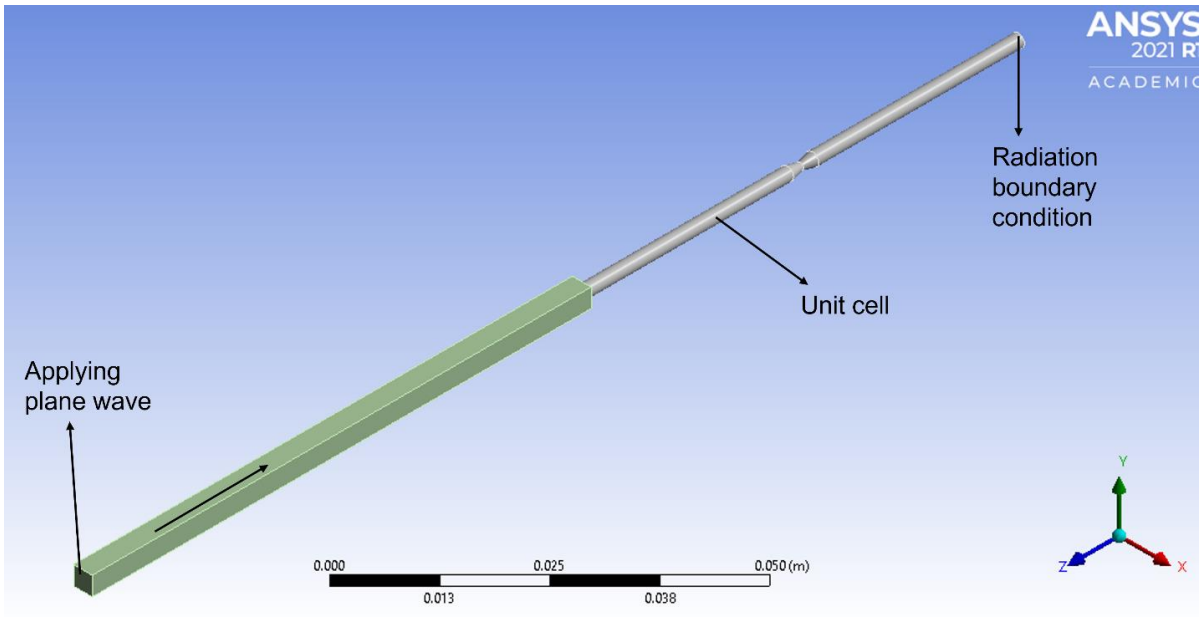

Figure 5.12: 3D CAD model setup for FEM simulation in ANSYS (Harmonic ACOUSTIC)

5.6 Physical properties of the 1D metamaterials

Table 2 shows the physical properties of all the sample made of the six different unite cells. The weight of each sample, weight penalty and packing density and the corresponding frequency range of higher sound absorption coefficient shown in table 5.3. Weight of all samples kept nearly equal to the glass woven mat sample (GWM). The weight reduction of the sample as compared to GWM, ranging from 3.9% to 14.47%, the higher weight reduction is in the KFAM and the lowest is in the IRAM. The open area for the ventilation is varying 49% to 68% as compared to GWM, which is sufficient for the air circulation through the sample. The highest ventilation is in SFAM and lowest in the IRAM. The sample volume of each sample is around 501411.83 mm^3. The benchmark sample is in our case is straight hollow fiber based, which have the density=678 $^{kg}/_{m^3}$,number of fibers is around 9000 and the total void volume is around 494800.84mm^3.

Table 5.3. Physical properties of the all the test sample made of the proposed ODVAM**.**

S. No.	Type of fiber arrangement	Weight of each sample (Kg)	Weight penalty w.r.t. glass woven mat fiber (% reduction)	Packing density (Solid volume / (solid + void volume)	Bandwidth (Hz)
1	Glass woven mat fiber (GWM)	0.380	NA	NA	500-700 Hz $0.9 < \alpha < 0.92$
2	Straight glass fiber (SHF)	0.340	10.52%	0.65	1000-1200Hz $0.78 < \alpha < 0.8$
3	Kink glass fiber	0.325	14.47%	0.60	900-1100Hz $0.82 < \alpha < 0.88$
4	YAM fiber	0.355	6.57%	0.56	1000-1400Hz $0.7 < \alpha < 0.79$
5	CDAM Fiber	0.330	13.15%	0.49	800-1000Hz $0.8 < \alpha < 0.88$
6	IRAM	0.365	3.9%	0.68	700-950 Hz $0.9 < \alpha < 0.95$

5.7 Results and discussion

We then use ANSYS 2021 R1 acoustic module to analysis the acoustic performance of ODVAM. The setup details of the FEM simulation are shown in FIG 5.12. To assess the acoustic performance of the meta-structure in the frequency domain (0-1600Hz), a typical inbuilt pressure acoustic module has been chosen. We take the single hollow fiber for the FEM simulation for study the acoustical properties of proposed different hollow fiber based one dimensional ventilated metamaterial. The frictional resistance at the boundary between the air and the kink walls causes the sound waves to dissipate inside the channels. Fig. 5.13 (a-d) shows the matching experimental data in addition to the numerical simulation. According to ASTM E1050–12 standard, the acoustic absorption coefficient is measured in the tests using

the standard B&k type-4206T impedance tube system. The experimentally measured absorption peak exhibits excellent agreement with the predictions from simulations. Simulation results shows narrow band as compared to experimental results because of visco-thermal losses which is not considered in the acoustic silencer simulation run. Additionally other factor like manufacturing and the rough surface of the hollow glass fiber and glass mat show additional losses, resulting widening of the absorption spectrum.

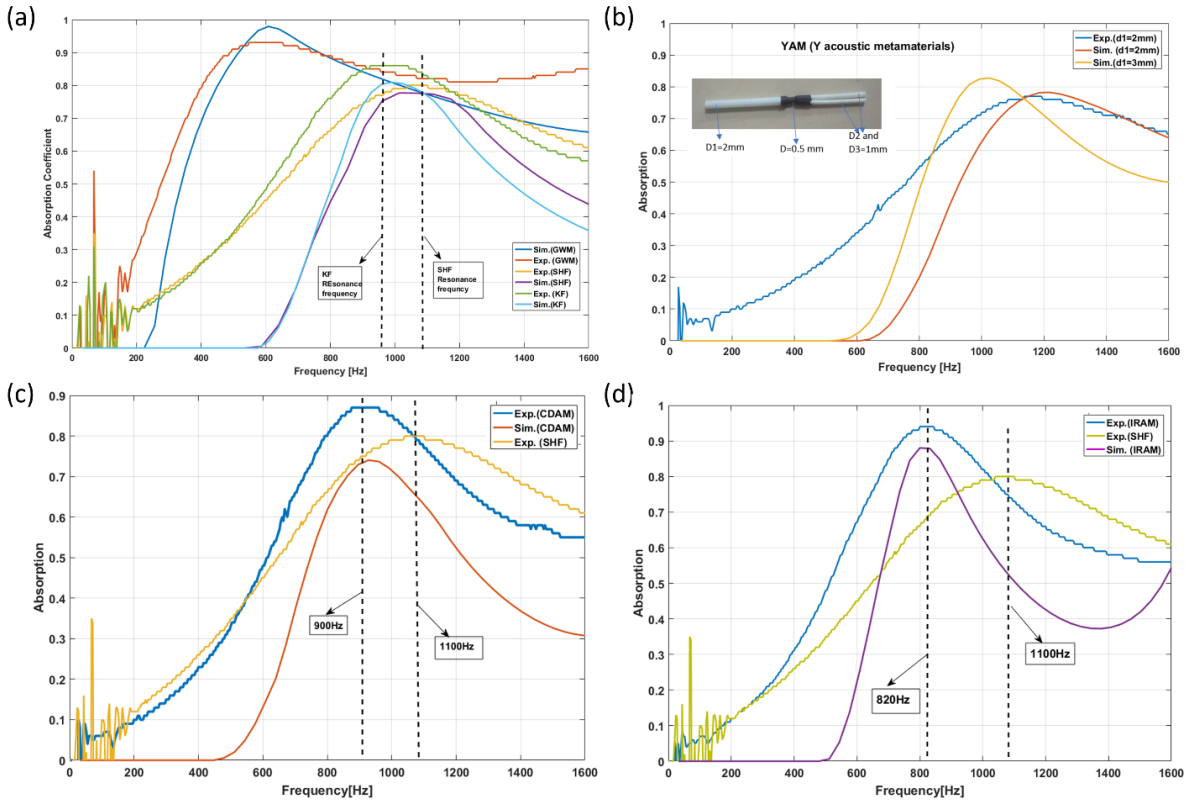

Figure 5.13: Sound absorption spectrum of experimental and numerical simulation of the four different sample with respect to frequency. (a) GWM, SF and KF sample absorption spectrum. (b) YAM sound absorption spectrum signature. (c) CDAM metamaterials absorption spectrum signature. (d) IRAM metamaterials sound absorption spectrum signature.

Figure 5.13(a), show the influence of kinking of hollow glass fiber on the acoustic performance of the metamaterials. Its shows the absorption signature of the glass mat, hollow straight fiber and the kink fiber having the same length. The glass mat shows excellent relative sound absorption (higher than 50% over a wide frequency range) in the range of 300Hz to 1600Hz but it hinders the flow of air through the structure. Moreover, it also limits the application where air circulation is needed. For providing the defined path for air flow and getting maximum incident sound go through the structure (not possible in 2D and 3D structure), we proposed kinking method at the center of the hollow tube. The absorption signature of the hollow straight tube and kinking tube as shown in Figure 5.13(a). The results show that the highest maximum sound absorption around 0.87, occur at 1100Hz in straight hollow fiber, but when we kink at the center, the absorption peak shift towards the left and achieved around 970Hz. The % of the shifting peak is around 11.82% calculated as $\% \, shift = \frac{(f_{Sf} - f_{kF})}{f_{Sf}} \times 100$.

The absorption signature of another design within the shape of "Y" and the kink at the center, reported in the Figure 5.13(b). There is no absorption peak shift as compared to the straight fiber as proposed in table 1. The straight fiber has the diameter of 1mm, and the "Y" type has the maximum diameter is 2mm. But changing the larger diameter to 3mm, absorption peak shift toward the left and it came around 9%. The absorption signature (numerical and experimental) of CDAM design reported in table 1, sample (E), shown in Figure 5.13(c). The maximum sound absorption has been achieved at 900Hz and the sound absorption is 87%. The sifting of sound absorption peak was around 18.18% and the sound absorption coefficient is higher than the straight hollow fiber. The last design is IRAM as shown in table 1, sample (f), designed based on internal open resonator and kinking at the center have been reported. It can be tuned as per the requirement in the range of 750 to 900 Hz without changing its height. The

absorption spectrum of the IRAM sample shown in Figure 5.13(d). The sound absorption is higher than all the samples and it is more the 91%. The shifting of the resonance peak around 25.45%. as compared to straight hollow fiber. The detail physical configuration and dimensions are shown in Figure 5.14.

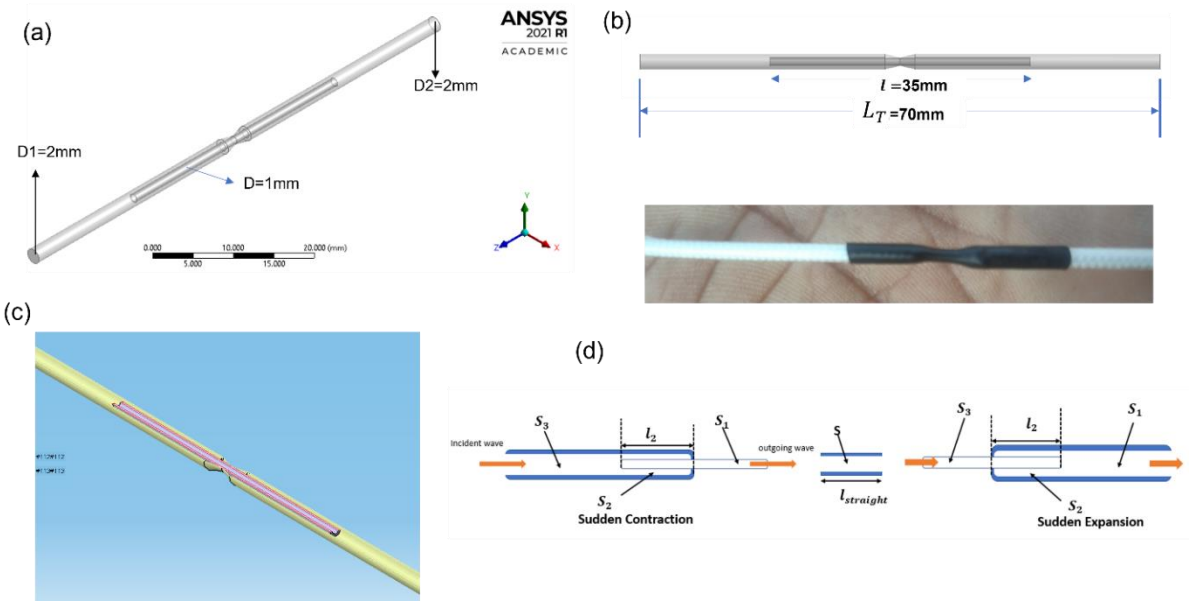

Figure 5.14: Geometric parameter and design of IRAM ventilated metamaterials. (a) isometric CAD view of IRAM and its dimensions, D1=D2=d. (b) The CAD model and the fabricated unit sample. (c) Horizontally cut section of the IRAM unit cell. (d) Detailed view of IRAM

Figure 5.14(a) and 5.14(c) shows the schematic view of the unit IRAM cell, in which the internal resonators have been clearly seen. Figure 5.14(b) shows the CAD model and the real unit cell of the IRAM sample. To demonstrate the notion, a thorough pilot simulation using several geometrical parametric sweeps was carried out to establish the parametric range of each variable for the desired frequency range (0–1600 Hz). Figure 5.15 (a) shows the cross-ponding sound absorption spectrum with internal pipe resonators that range in length from 10

mm to 60 mm while maintaining a fixed main kink hollow resonators length of 70 mm. As we increase the internal resonators length, the sound absorption peak begins to move to the left while also becoming lower sound absorption, as seen in Figure 5.15 (a). Around 830 Hz, with l=20 mm, the maximum amount of sound is absorbed, with 90% efficiency. The sound absorption coefficient of the two extreme cases, one at l=10 mm the absorption coefficient is around 87% at 850 Hz and second case when $l = 60mm$, the absorption coefficient is around 82% at 750Hz. As we can absorb that as l_2 is inversely proportional to the natural frequencies. as length of the internal resonators increases the resonance frequency going to be shift left. Figure 5.15(b) shows the influence of the kink resonators length on the overall sound absorption signature of the proposed structure. As the length of the kink resonators increases the absorption peak start shifting left. The resonance peak shifts by around 25%, when the length ranges from 70 to 100 mm.

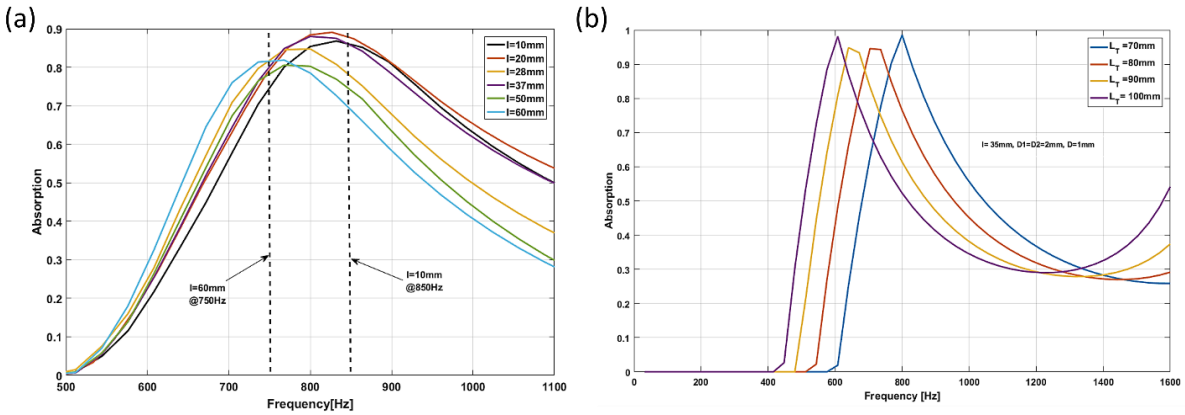

Figure 5.15: (a) Sound absorption signature of the metastructure (IRAM) under different internal resonator length. (b) Sound absorption spectrum with varying external diameter of the IRAM.

5.8 Analysis of ventilation characteristics

GMM exhibits no ventilation, whereas SHF features 100% ventilation. The remaining four samples showcase almost complete airflow (nearly 100%) air flow through the structure with minimal reflection as shown in table 3. In order to demonstrate the efficacy of the proposed models, it is crucial to not only assess their acoustic performance but also to incorporate CFD simulations. These simulations provide analyzing essential parameters such as pressure drop and velocity to further validate their effectiveness.

Table 5.4: Ventilation characteristics of the all-unit cell of the proposed ODVAM.

Sample No.	Name of the unit Cell	Ventilation $({}^{A_i}/_{A_0}) \times 100$ % (A_i inlet area and A_0 outlet area of the unit fiber
(A)	Glass woven mat fiber (GWM)	0
(B)	Straight glass fiber (SHF)	100
(C)	Kink glass fiber	100
(D)	YAM fiber	100
(E)	CDAM Fiber	25
(F)	IRAM	25

To analyzing airflow performance of the ventilated one-dimensional structure, a Computational fluid dynamic (CFD), ANSYS workbench module was used. A pressure of 110 kPa ($P_{atm} = 101.32$ kPa) pressure was used at one end of the fiber, while the opposite end was subjected to the gauge pressure 0 kPa pressure, and then performed the FEM simulation. The pressure and velocity variation across the fiber as shown in Figure 5.16 (a) and 5.16 (b).

Based on the results, it becomes evident that as the velocity increases, there is a corresponding rise in pressure drop. Contour plots of ODAMs show how the air flows inside the fibers. All contour plots depict the inlet pressure of 110 kPa and corresponding velocities variations. The straight fiber and YAM fiber exhibited positive pressure drops, whereas the other fibers demonstrated negative pressure drops at the kinking point, resulting in enhanced absorption coefficient.

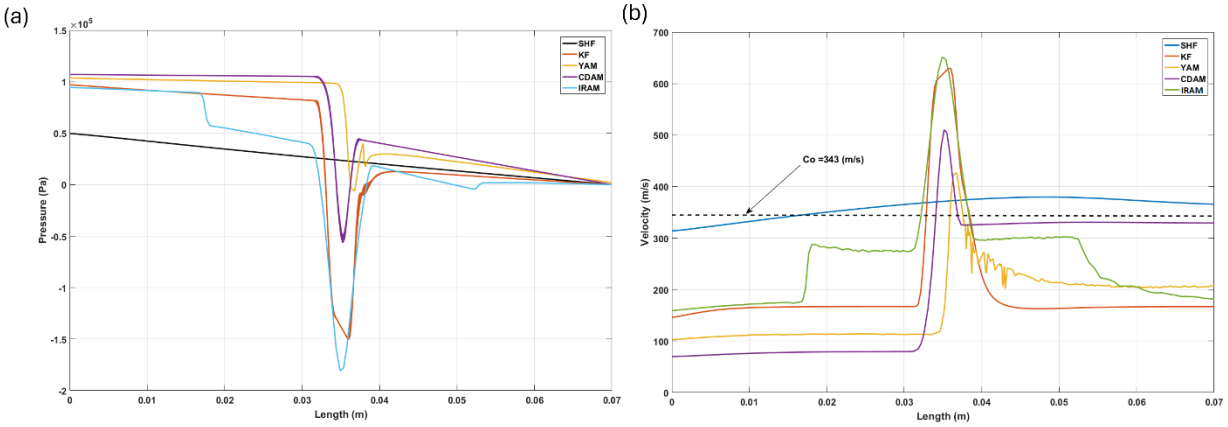

Figure 5.16 : (a) Air pressure signature across the fibre length. (b) Air velocity signature across the fiber length.

(c)

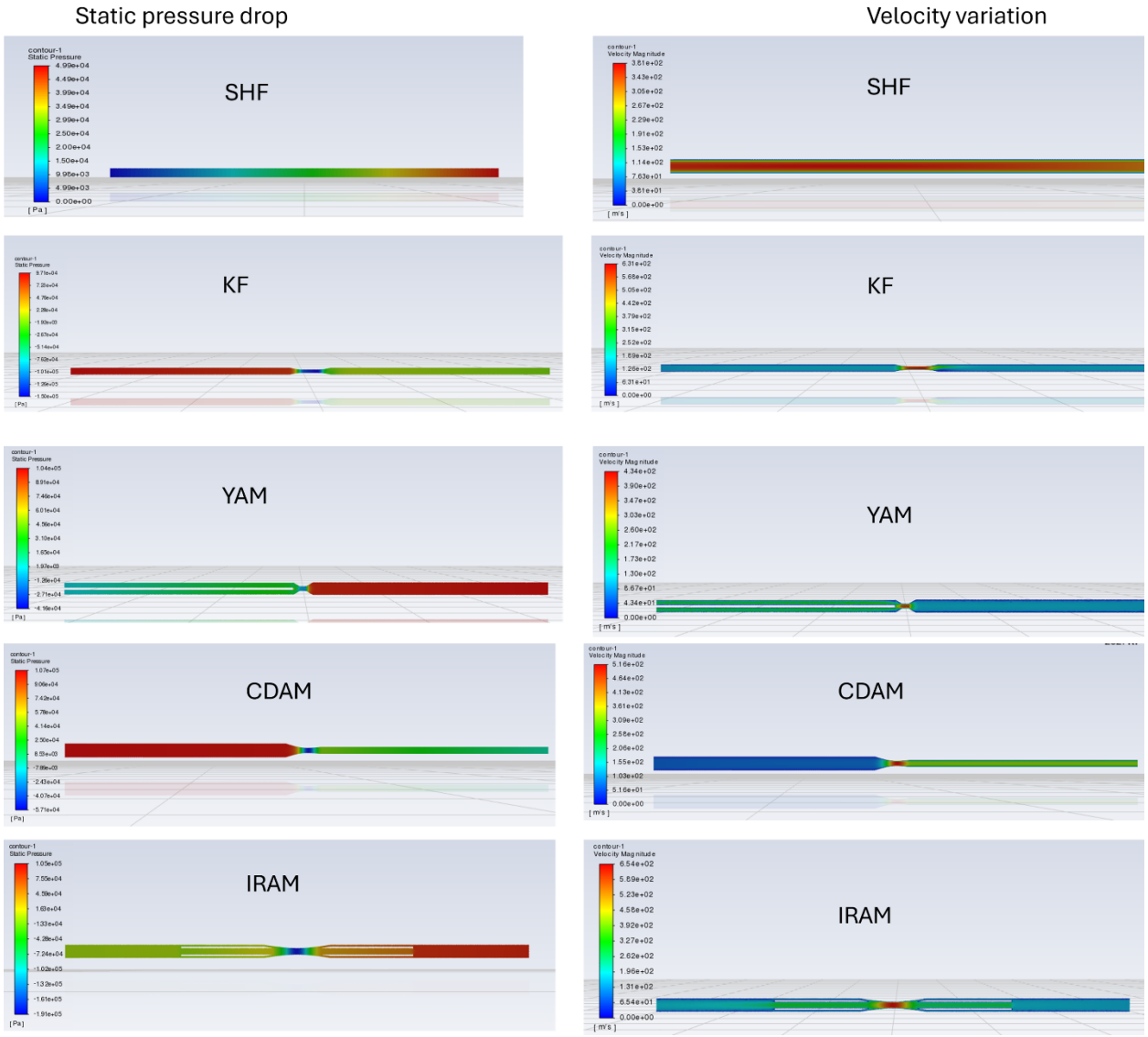

Figure 5.17: (c) Contour plots of ODAM: pressure drop and velocity variation inside the fibers

5.9 Conclusion

In conclusion, we numerically and experimentally verify a one-dimensional acoustic ventilated metastructure that exhibits robust broadband sound absorption in the low- to mid-frequency range (500–1600 Hz). According to the experimental findings, a higher relative bandwidth results in almost complete sound absorption. It has also been demonstrated that by altering the various geometrical parameters, the acoustical performance of the suggested metastructure

design could be customized over a broad frequency range. Additionally, high absorption from the suggested metastructure over broadband frequencies is accomplished by experimenting with various kinking method configurations and hollow fiber dimensions. The suggested concepts also showed how they might be used in engine shielding and architectural acoustics, both of which demand vented windows with good noise-isolating qualities. Finally, our suggested plan might work well for low- to mid-frequency noise suppression in small spaces that need adequate ventilation and very little sound refraction.

Acknowledgement

This work was supported by Boeing International Corporation270India Private Limited (Grant No. BOEING/ME/2016081).

DATA AVAILABILITY

The data that support the findings of this study are available from the corresponding author upon request.

Chapter 6 : Noval flat spiral ventilated metamaterials with low frequency and broadband sound absorption

6.1 Abstract

The new development of acoustic metamaterials opens up previously unimaginable possibilities for sound management in a variety of contexts, however it is still difficult to achieve simultaneous free air movement and broadband high sound absorption specially in the low frequency regime. This article introduces two types of ventilated novel subwavelength device VAM (ventilated acoustic metamaterials) and RTVAM (Rainbow trapping ventilated acoustic metamaterials) with a thickness of 14 mm (or 1.4 cm) to 78mm (or 7.8cm). It has the potential to provide air ventilation and noise reduction at the same time. We demonstrated a novel ventilated metamaterials which is consisting of many disks and each disk has four spiral channels in a one plane can resolve the problems of very low frequency sound (around 200Hz) and broadband more than on octave while maintaining the air circulation of 12% to 5%. In this work, a miniature prototype that is based on a multi-armed spiral shape was designed and constructed. In order to ascertain the suggested ventilated metamaterial's acoustical characteristics in terms of sound absorption, numerical, theoretical and experimental research were conducted. We report near perfect sound absorption at nearly four frequencies extending from 200 to 1600Hz for panel made up of 10 discs with a total thickness of 7.8cm, which is 22times smaller than the wavelength at 300Hz. The experimental examination reveals strong sound absorption with high bandwidth (more than an octave), acoustic qualities that may have uses in reducing low- and mid-frequency noise in metropolitan areas. The proposed

metastructure can enable airflow to effectively dissipate heat and stop noise from continuing to spread, which can better address the issues with noise and heat dissipation.

6.2 Introduction

Using sound insulation or absorption while maintaining the air flow through the structure, to control low frequency and broadband noise is a crucial scientific challenge in acoustic engineering. Due to their physical properties, shape controllability, and small volume/size, acoustic metamaterials[141],[121],[21] and acoustic metasurfaces [142] have emerged as the most promising candidates for noise control engineering and advanced acoustic material design and manufacture in recent years. Ultra-broadband working bandwidth[99],[143],[144],[145], ultrathin efficient tunable metastructure,[146],[59] has been designed for acoustic metamaterial/metasurface absorbers. which aid in the creation of the theoretical acoustic device known as the acoustic meta-absorber.

Another significant issue in acoustic engineering is acoustic absorption and insulation by acoustic metamaterials in ventilated structures. This issue has a wide range of potential practical applications, including noise control for air conditioners, vehicles, and building ventilating ducts. In some cases, it is also necessary to simultaneously transfer heat and absorb noise. Recent developments have shown a number of ventilated meta-material absorbers.[37],[110], typically containing labyrinth-like structures,[147],[148],[149],[21] and meta surfaces made up of Helmholtz resonators[150],[151]. However, certain recent developments in the field of metamaterials offer a fresh perspective on the prospect of unconventional wave management in ventilated spaces. Ghaffarivardavagh et al. [148] proposed a spiral-coiling metamaterial with roughly 60% of its surface area accessible to airflow. By using the narrow band Fano-like interference spectrum, this structure was shown

to be effective at reducing harmonic industrial noise. Reducing structural complexity, lowering and enlarging sound shielding bands, and even expanding multifunctional applications are all ongoing goals in noise control engineering.[125],[152] Despite the reported advancements, the majority of current attempts are still restricted to a particular function and have either a small bandwidth, high thickness , or highly restricted functionality.

In light of this, this work describes a carefully built sound barrier that not only has the thinnest construction but also permits broadband sound insulation at very low frequencies. It was inspired by the space-coiling method in one plane. Furthermore, we investigated the sound absorption acoustic characteristics with the help of the transfer matrix method. Through changing the size of the coiled channels and a disk, it is possible to tune a particular frequency and at the same time the broadband sound absorption, which may facilitate multifunctional applications beyond sound proofing realm, such as tunable sound absorption and air ventilation. The type 1 VAM (Ventilated acoustic metamaterials) was intent to design the thinnest metamaterial to produce a broadband sound absorption mid and higher frequency while RTVAM was design to exhibit low frequency specially around 200Hz and broadband perfect absorption.

6.3 Ventilated absorber design strategy

To create spiral-shaped subwavelength metamaterial structure with a ventilation capability for broadband sound modification at low frequencies. Four spiral channels make up the construction, which also has a vented aperture in the middle that lets air travel through. These spiral tubes decrease the propagation of the acoustic wave by rotating it around the center opening. In order to overcome problems with broadband sound absorption and transmission caused by facades and acoustic barriers, the construction consists of linking an array of four

identical spiral arm resonators. The current study concentrated on the noise attenuation brought on by the connection of four spiral resonators with a broad bandwidth and a thickness that was subwavelength in size. The author proposed two types of acoustic ventilated panel ,1) uniform cross section central hole ventilated metamaterials and 2) the converging center cross section hole metamaterials as shown in Figure 6.1. The unit cells of each panel are shown in Figure 6.1 (b, e). we chose the spiral resonator as a basic structure to design the noise absorber. Because the sound absorption performance of the ventilated meta-structure of the spiral resonators is only related to the side length of the cross section and the resonance frequency is only related to the length of the resonators, which is easily tuned as per requirement.[153]

The color path as shown in Figure 6.1(c, f), depicts the lateral flow of noise path in each channel. In one plane there are 4 channels placed at $0°, 90°, 180°$ and $270°$ as shown in Figure 6.2 (b). Each channel has the cross-section dimensions is 6mm× 3mm. The length of each channel of the uniform ventilation metamaterials is around 408.96mm. The convergent cross section ventilated metamaterials of each disk have the spiral length are around 398.18mm,383.07mm, 355.01mm and 319.22mm.

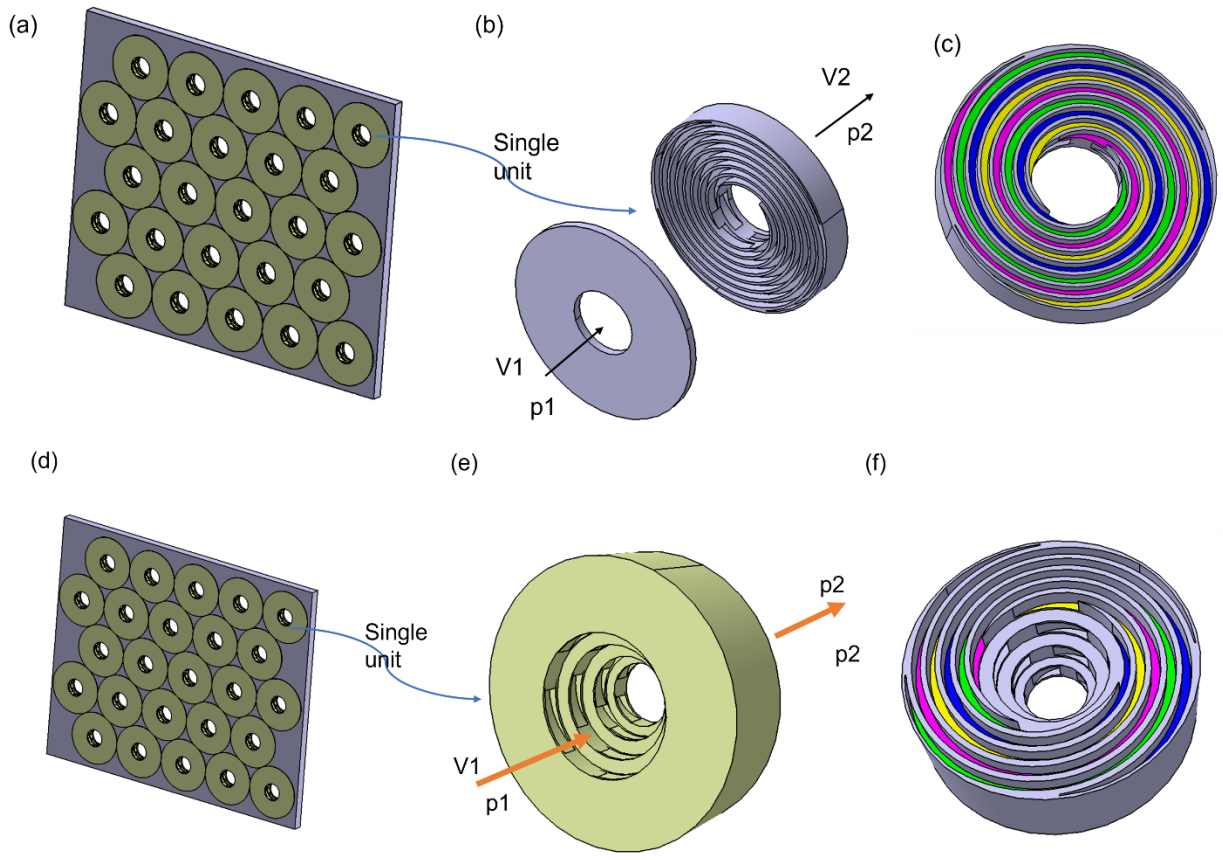

Figure 6.1: Type 1: (a) Broadband ventilation barrier consisting of periodically arranged unit cells with uniform ventilated cross section (VAM). (b) shape of the unit cell composed of set of eight spiral resonators (2 disks) coupled around the air passage hole having the thickness of 15mm. (c) Colored channels show the acoustic wave flow path inside the spiral chambers. Type 2: Rainbow trapping ventilated acoustic metamaterials (RTVAM) (d) low frequency and broadband barrier absorber consisting of periodically arranged unit cells with diverging ventilated cross section. (e) The unit cell of the absorber (4 disks). (f) Colored channels show the acoustic wave flow path inside the spiral chambers.

The ventilated diameter of the disk D as shown in Figure 6.2 (a) is d_4=23mm, disk "c" is d_3=30mm, disk "B" is d_2= 40mm and the disk "A" is d_1=50mm as shown in Figure 6.2 (d).

In the Figure 6.2(b) shows the 4 channels in one disk and the red spiral line shows the path of the acoustic wave flow direction. The diameter of outer disk D_0=100mm and D_i = 23mm. The thickness of the partition between the units is 1mm. The total thickness of single unit is $a + 2t$.

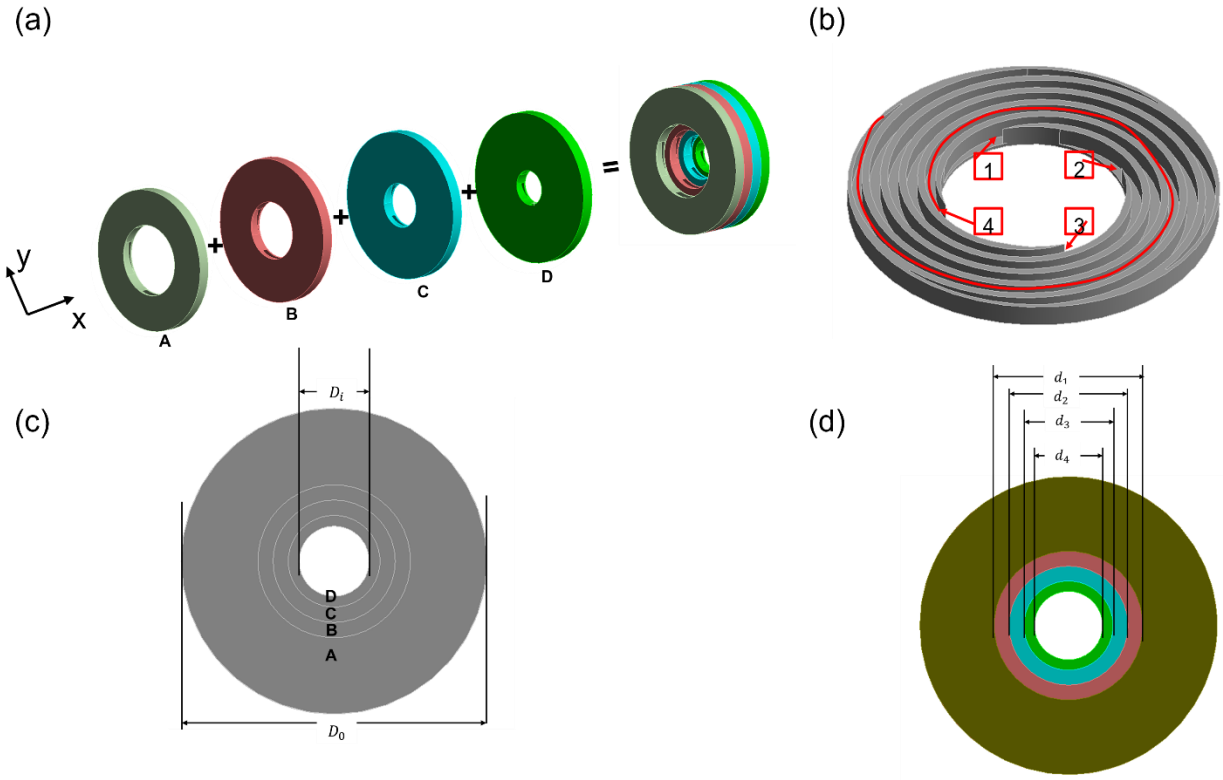

Figure 6.2: (a)Type 2: The exploded view of the ventilated metamaterials. (b) showing the path of the spiral channel. (c), (d) Front view of the metamaterials

6.4 Theoretical modeling

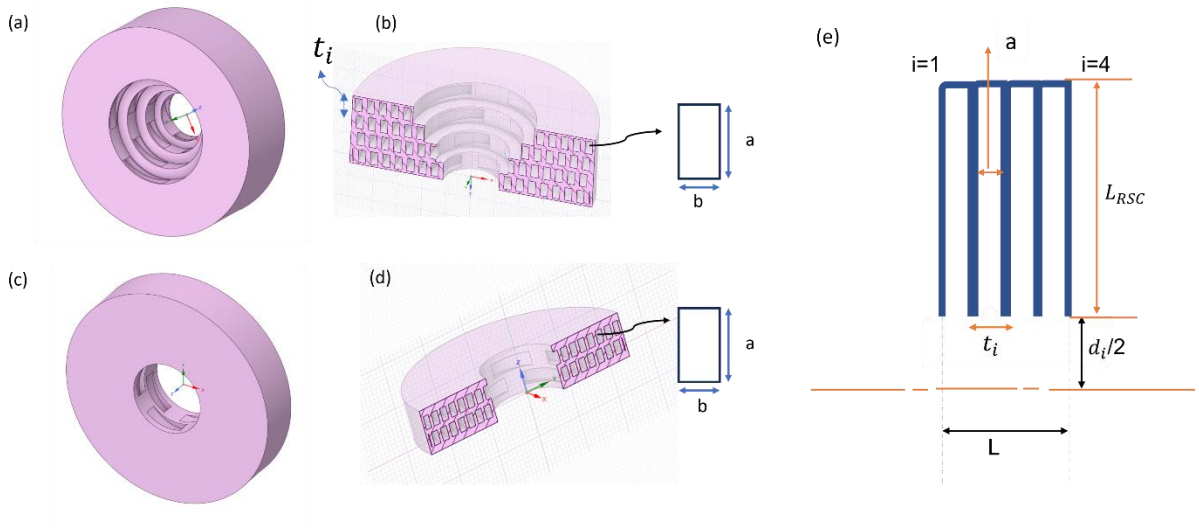

Figure 6.3: (a-d) UVAM and RTVAM cross sectional view and the channels dimensions; (e) Sectional view of the ventilated metamaterials x-y plane.

The transfer matrix method (TMM) is employed for conducting theoretical analyses on the suggested metamaterials. We designate the sound pressure of the sound wave as $'p'$ "and the normalized sound velocity in the horizontal direction as v_x. Assuming the presence of solely plane waves in the waveguide, based on the continuous boundary conditions of sound pressure and velocity, we derive the following:

$$\begin{bmatrix} p \\ v_x \end{bmatrix}_{x=0} = T \begin{bmatrix} p \\ v_x \end{bmatrix}_{x=L} = \begin{bmatrix} T_{11} & T_{12} \\ T_{21} & T_{22} \end{bmatrix} \begin{bmatrix} p \\ v_x \end{bmatrix}_{x=L} \tag{6.1}$$

Here, 'T' represent the system transfer matrix. which can be obtained by deriving it from the transfer matrix of 'N' central through holes of varying sizes and the spiral tubes coiled around them. This is demonstrated in the subsequent formula:[154]

$$T = M_{\Delta s}^{1} \prod_{i=1}^{i=4} M_{s}^{i} M_{sc}^{i} M_{\Delta s}^{i+1} \tag{6.2}$$

Where $M_s^i$is the transfer matrix of the central through hole of the i-th unit, M_{sc}^i is the transfer matrix of the spiral coil tubes of the i-th unit, $M_{\Delta s}^i$is the modified transfer matrix item of the central through hole of the i -th unit considering the radiation effect.

For visual display of the proposed meta-structure, we replace the coiled channels with long straight tubes as shown in Figure 6.3 (e). Due to the small cross-sectional area of the central through hole and the S-C tube, we should consider the visco-thermal losses. So, we introduce the equivalent complex index. The medium is air with mass density $\rho_0 = 1.213$kg/m3, sound speed $c_0 = 343$ m/s, atmospheric pressure p_0 =101 325 Pa, dynamic viscosity τ =1.79 × 10−5 kg/(m · s), specific heat ratio $\gamma = 1.4$, Prandtl number Pr =0.7167. The equivalent complex density ρ_d^i and equivalent bulk modulus k_d^i of the central through-hole air can be expressed as [47]

$$\rho_d^i(\omega) = \rho_0 \left[1 - \frac{2}{r_i G_p} \frac{J_1(r_i G_p)}{J_0(r_i G_p)}\right] \tag{6.3}$$

$$k_d^i(\omega) = k_0 \left[1 - \frac{2(\gamma - 1)}{r G_k} \frac{J_1(r_i G_k)}{J_0(r_i G_k)}\right] \tag{6.4}$$

where $G_p = \sqrt{\frac{-i\omega\rho_0}{\tau}}$, $G_k = \sqrt{\frac{-i\omega p_r \rho_0}{\tau}}$, and the air bulk modulus $k_0 = \gamma p_0$. J_n is the Bessel function of the first kind and order n. The normalized acoustic impedance is given by ${z_d}^i = \sqrt{k_d^i \rho_d^i} \Big/ \pi r^2$

Next, we can get the transfer matrix of the central through hole of the i -th unit M_s^i ,

$$M_s^i = \begin{bmatrix} \cos(k_d^i L_i) & \mathrm{i} Z_d^i \sin(k_d^i L_i) \\ \frac{i}{Z_d^i} \sin(k_d^i L_i) & \cos(k_d^i L_i) \end{bmatrix} \tag{6.5}$$

Where k_d^i is the equivalent complex wave number of the central through hole of the i-th unit,

Let's now calculate the impedance of the spiral tube.

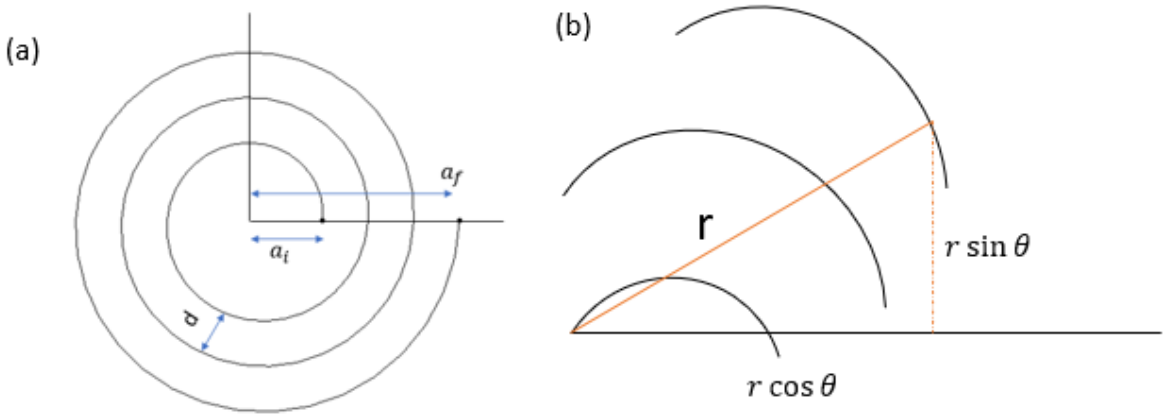

Figure 6.4 : Schematic diagram of the (a) Archimedes spiral. (b) Parameters in polar coordinates

The spiral curve can be expressed as

$$r = a_i + b\theta \tag{6.6}$$

Where a_i is the initial radius of the spiral with its final angle θ.

Whose x and y component in polar coordinates are,

$$x = r\cos\theta = (a + b\theta)\cos\theta \tag{6.7}$$

and

$$y = r\sin\theta = (a + b\theta)\sin\theta \tag{6.8}$$

Where parameter b is the spiral growth ratio, which is calculated as

$$b = \frac{a_f - a_i}{2\,\pi\,n} \tag{6.9}$$

Where n is number of turns of the spiral

The spiral depicted in Figure 6.4 (a) is one dimensional curve. This one-dimensional curve used to create the 3D acoustic wave rectangular spiral channels (RSC). The dimension of the channels having the width w and a height h.

The final angle of the spiral can be calculated as

$$\theta_f = \frac{a_f - a_i}{b} \tag{6.10}$$

The total length of the 2D RSC is then calculated as

$$L_{RSC} = \int_{\theta_i}^{\theta_f} \sqrt{r^2 + (dr/d\theta)^2 \; d\theta} \tag{6.11}$$

$$L_{RSC\,eff} = \; L_{RSC} + \delta \tag{6.12}$$

let's consider the one-dimensional visco-thermal plane wave propagates in the rectangular cross-section pipe. We assuming that only plane waves propagate inside the RST.

The propagation can be modelled with effective density and bulk modulus given by [96],[140]

$$\rho_{RST}(\omega) = \rho_0 \frac{a^2 b^2}{4{G_p}^2 \sum_{m=0}^{N} \sum_{n=0}^{N} \left[{\alpha_m}^2 {\beta_n}^2 ({\alpha_m}^2 + {\beta_n}^2 - {G_p}^2)\right]^{-1}} \tag{6.13}$$

$$K_{RST}(\omega) = K_0 \frac{1}{\gamma + \frac{4(\gamma-1){G_k}^2}{(\frac{a}{2})^2 (\frac{b}{2})^2} \sum_{m=0}^{N} \sum_{n=0}^{N} \left[{\alpha_m}^2 {\beta_n}^2 ({\alpha_m}^2 + {\beta_n}^2 - {G_k}^2)\right]^{-1}} \tag{6.14}$$

Where a is width and b is the height of the rectangular SRT, $\alpha_m = \frac{(2m+1)\pi}{a}$ and $\beta_n = \frac{(2n+1)\pi}{b}$ .The infinite sums are numerically calculated for a variety of duct dimensions with a truncation number of 100 and an accuracy of 5 significant figures. The characteristic impedance and acoustic wavenumber for a fluid layer can then be determined using these expressions.

Then the acoustic impedance of the SRT can be calculated as ${Z^i}_{SRT} = \sqrt{K_{RST}(\omega)\rho_{RST}(\omega)}\,/ab$

Similarly, the transfer matrix of the S-C tube of the i -th unit

$$M_{SC}^{i} = \begin{bmatrix} 1 & 0 \\ 1/Z_R & 1 \end{bmatrix} \tag{6.15}$$

Where Z_R =-iZ^i_{SRT}cot ($K_{RST}(\omega)L_{RSC\,eff}$)

End corrections

When there are discontinuities in the waveguides owing to section changes, radiation correction must be implemented.

Therefore, we can get the radiation correction impedance of each unit $Z^i_{\Delta d}$, then, the central through-hole radiation correction transfer matrix of the i -th unit $M^i_{\Delta d}$, can be obtained.

$$Z^i_{\Delta d} = -i\omega\Delta l^i_d \rho_0 \emptyset_i / s_i \tag{6.16}$$

$$M^i_{\Delta s} = \begin{bmatrix} 1 & Z^i_{\Delta d} \\ 0 & 1 \end{bmatrix} \tag{6.17}$$

where $\emptyset_i = {d^{n-1}}/{d^n}$ and $s_i = \pi({d_i}/{2})^2$

The discontinuity happened, when the duct is loaded in parallel to principal waveguide as shown in Figure 6.2. The length of the end correction Δl^i_d is given by [155]

$$\Delta l^i_d = 0.82[1 - 0.235\frac{r_n}{r_t} - 1.32\left(\frac{r_n}{r_t}\right)^2 + 1.54\left(\frac{r_n}{r_t}\right)^3 - 0.86\left(\frac{r_n}{r_t}\right)^4]r_n \tag{6.18}$$

After obtaining M^i_s , M^i_{SC} and $M^i_{\Delta s}$ it is easy to get the system transfer matrix and then the system equivalent wavenumber K_e, equivalent impedance Z_e, equivalent sound velocity c_e, sound energy transmission coefficient T, reflection coefficient R and sound absorption coefficient A can be calculated from equation (6.19) to(6.24).

$$k_e = \frac{a}{L} cos\left(\frac{T_{11} + T_{22}}{2}\right) \tag{6.19}$$

$$Z_e = \frac{\sqrt{T_{11}/T_{21}}}{Z_0} \tag{6.20}$$

$$C_e = Re\left[\frac{w}{k_e}\right] \tag{6.21}$$

$$T = \left|\frac{T_{11} + T_{12}}{Z_0} + (T_{21} + T_{22})Z_0\right|^2 \tag{6.22}$$

$$R = \left|\frac{\frac{T_{11} + T_{12}}{Z_0} - T_{21}Z_0 - T_{22}}{\frac{T_{11} + T_{12}}{Z_0} + T_{21}Z_0 - T_{22}}\right|^2 \tag{6.23}$$

$$A = 1 - T - R \tag{6.24}$$

where the free space air impedance $Z_0 = \rho_0 C_0$.

Table 6.1: Geometrical dimensions of the type 1 (UAVM) acoustic metamaterials of N=2 disks

i	Cross section of channel $(a \times b)mm^2$	t_i (mm)	${d_i}/{2}$ mm	Ventilation $({d_i}^2/{D_0}^2) \times 100\%$
1-2	6× 3	7mm	17mm	12%

Table 6.2: Geometrical dimensions of the type 2 (RTAVM) acoustic metamaterials of N=4 disks

i	Cross section of channel $(a \times b)mm^2$	t_i (mm)	$d_i/_2$ mm	Ventilation $(d_i{}^2/_{D_0{}^2}) \times 100\%$
1	6× 3	7	25	25.25%
2	6× 3	7	20	16%
3	6× 3	7	15	9%
4	6× 3	7	11.5	5.3%

Table 6.3: Geometrical dimensions of type 2 (RTAVM) acoustic metamaterials of N=10 disks

i	Cross section of channel $(a \times b)mm^2$	t_i (mm)	$d_i/_2$ mm	Ventilation $(d_i{}^2/_{D_0{}^2}) \times 100\%$
1	6× 3	7	25	25.25%
2	6× 3	7	22.5	22%
3	6× 3	7	21	18.24%
4	6× 3	7	20	16%
5	6× 3	7	18.75	14.2%
6	6× 3	7	17.5	12.37%
7	6× 3	7	16.25	10.67%
8	6× 3	7	15	9.09%
9	6× 3	7	13.75	7.638%
10	6× 3	7	12.5	6.31%

6.5 Results and discussion

6.5.1 Sound Absorption measurement

Figure 6.5 shows the sound absorption spectra of the proposed metamaterials. Three samples UVAM (two disks) ,RTVAM (four disks) and RTVAM (ten disks) have been tested in acoustic impedance tube.[156] Blue curve shows the results of the sound absorption coefficient for the proposed UVAM metamaterial (thickness is 14mm) whose geometry parameters are listed in table 6.1. Experimental measurements were performed, and the maximum sound absorption coefficient reached 0.91 at 1344 Hz and 0.6 at 992Hz. The relative broadband sound absorption (>50%) was obtained in the frequency range of more than one octave (880Hz to >1600 Hz)

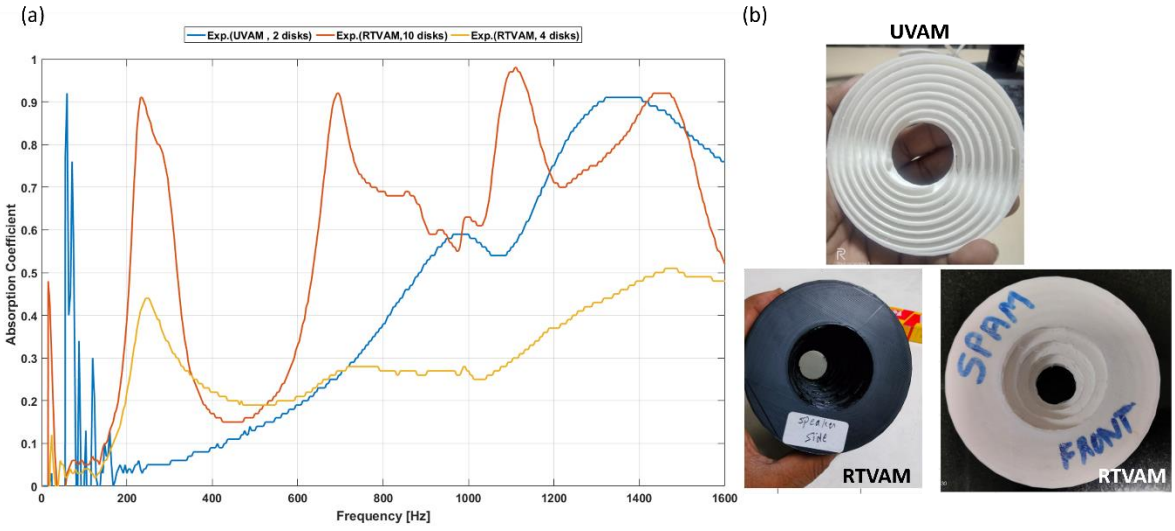

Figure 6.5 : (a) Impedance tube test of the sample UVAM, RTVAM And RTVAM. (b) 3D printed samples

The sound absorption characteristics of RTVAM, with a thickness of 28mm and its listed geometry parameters in Table 6.2, demonstrate broad-spectrum sound absorption, reaching a

maximum absorption of 0.44 at 240Hz. To enhance the absorption coefficient, we employed 10 disks with a total thickness of 70mm, subjected to testing in an impedance tube. The sound spectra of RTVAM with 10 disks is illustrated by the orange curve in Figure 6.5. The geometry parameters of type 2 (RTAVM) listed in Table 6.3. The spectra reveal multiple absorption peaks at distinct frequencies—236 Hz, 696 Hz, 1108 Hz, and 1140 Hz—with corresponding sound absorptions of 0.91, 0.92, 0.98, and 0.92, respectively. Notably, two instances of relatively broad sound absorption (>50%) were achieved within the frequency ranges of 200 Hz to 320 Hz and spanning more than one octave in the band from 630 Hz to 1600 Hz.

6.5.2 Acoustic FEM based Simulation and theoretical validation.

6.5.2.1 FEM, TMM and Experimental verification of UVAM

A theoretical model, a numerical simulation model, and experiments were employed to verify the acoustic performance of the proposed ventilated type 1 metamaterials. In MATLAB, the theoretical model was created. ANSYS workbench 2021 R1 (Acoustic module) [42] ,commercial finite element software was used to create the numerical simulation mode. At the source end, the radiation boundary condition was applied for non-reflecting field. A plane wave boundary condition was used to simulate the incident sound wave. In our study, the element size of the mesh was taken less than the $1/6$ of the shortest incident simulated sound wavelength.

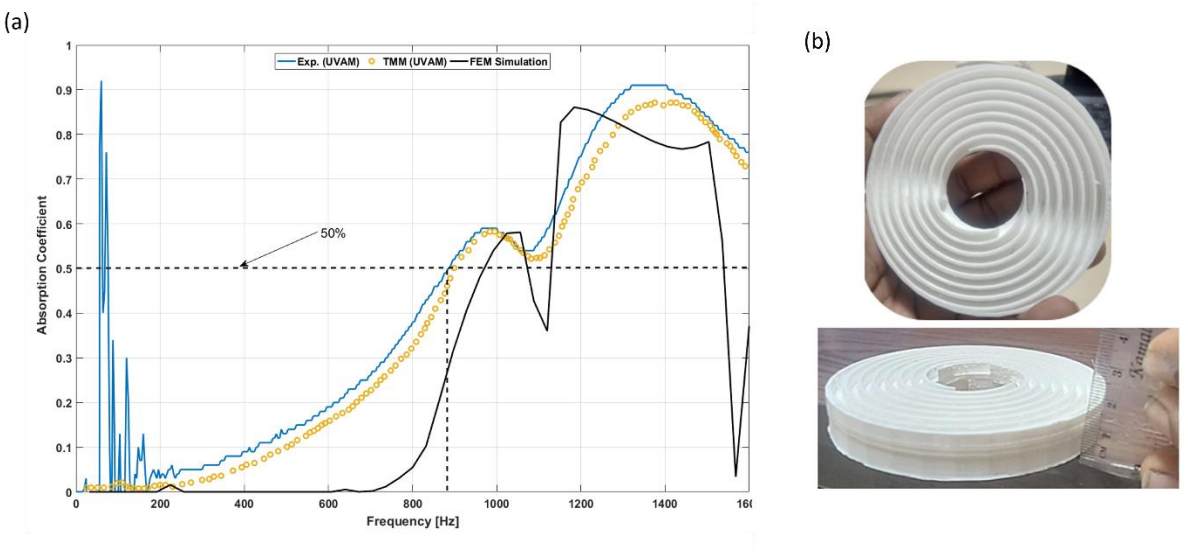

Figure 6.6 : Air ventilated UVAM meta unit cell, (a) Sound absorption spectrum of unit cell . (b)Photograph of 3D printed Meta unit, composed of eight spiral resonators assembled in-parallel hole.

The experimental results, TMM results, and numerical prediction are compared with good agreement. Other factors that affect the resonance are sometimes known as non-ideal effects, like viscos-thermal effects, form factors, effects on edges, manufacturing imperfections, etc.[108]

Given the possibilities of axial coupling of eight spiral resonators in different axial orientations, the next two different design will be performed in order to understand the cases of low frequency broadband (1) Increasing the number of spiral resonators and (2) The effect of geometry configuration without changing of the thickness of the structure.

6.5.2.1.1 Increasing the number of spiral coupled resonators

The design of a thin, broadband acoustic absorber with multiple frequencies and air ventilation is a sought-after advancement in noise control engineering. we achieved narrow and broadband

sound absorption by interconnecting spiral resonators. Each disk consists of four spiral resonators of the same length. Initially, the absorption spectra of two disks, totaling eight resonators, were reported (see Figure 6.6). Subsequently, now we explored the impact of coupling more than eight spiral resonators on the sound absorption spectrum, as depicted in Figure 4b.

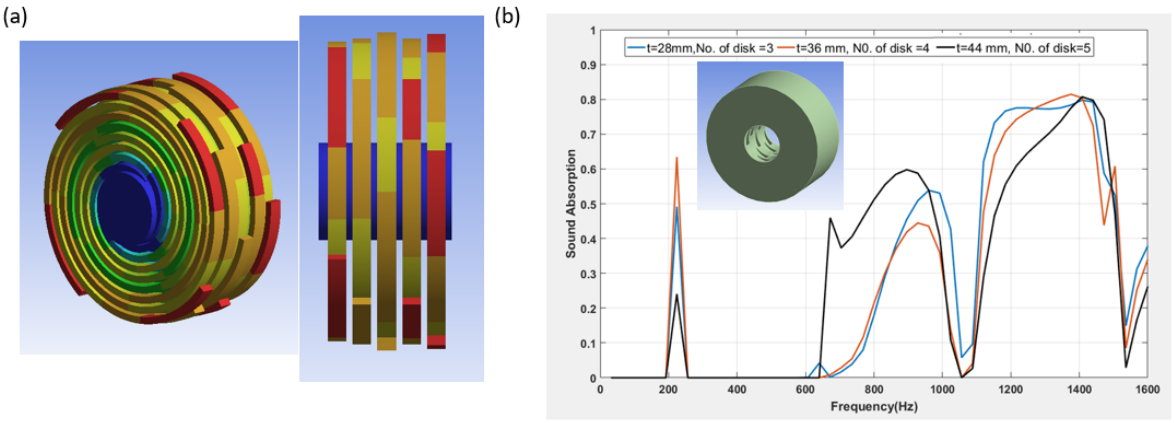

Figure 6.7: Sound pressure level (SPL) distribution of ventilated acoustic meta-structure. (b) Variation of sound absorption spectrum concerning the increasing number of disks or resonators.

We designed three samples with varying configurations: (1) Three disks comprising 12 resonators and a thickness of 21mm; (2) four disks with 16 resonators and a thickness of 28mm; (3) five disks with 20 resonators and a thickness of 35mm. Figure 6.7 (a) illustrates the sound pressure level (SPL) in dB for the third sample.

The sound absorption spectrum of all three proposed meta-structures is presented in Figure 6.7(b). With an increase in the number of disks, a distinct sound absorption peak emerges at 224 Hz, accompanied by two broad sound absorption bands around 850 Hz and approximately 1300 Hz. As the number of disks increases, the structure demonstrates broadband sound

absorption, with maximum absorption values of 0.65, 0.6, and 0.8 at 224 Hz, 900 Hz, and 1300 Hz, respectively. However, within a frequency range of 600 Hz to 1600 Hz, the absorption drops to zero around 1000 Hz due to the omission of viscothermal losses in the FEM simulation.

6.5.2.1.2 Effect of geometry configuration without changing the thickness

In this section, we explore three distinct meta-structures, each sharing a constant thickness of 14 mm and comprised of two disks. The geometric parameters for the first Acoustic Ventilated Metamaterial (UVAM) are set as follows: b=2mm, a=6mm, and the number of spiral revolutions N=3. The second UVAM features parameters b=1mm, a=6mm, and N=3, while the third AVM is characterized by a=1mm, b=6mm, and N=4.

This meta-unit demonstrates an expanded sound absorption bandwidth, exhibiting multiple absorption peaks spanning from 950 Hz to 1600 Hz, with absorption amplitudes ranging from 0.6 to 0.85, as depicted in Figure 6.8(b). Upon increasing the number of turns, as observed in the third sample, a new narrow absorption peak emerges in addition to broadband sound absorption. These results underscore the influence of the geometric configuration of the spiral channels in adjusting both multiple sound absorption peaks and broadband sound absorption.

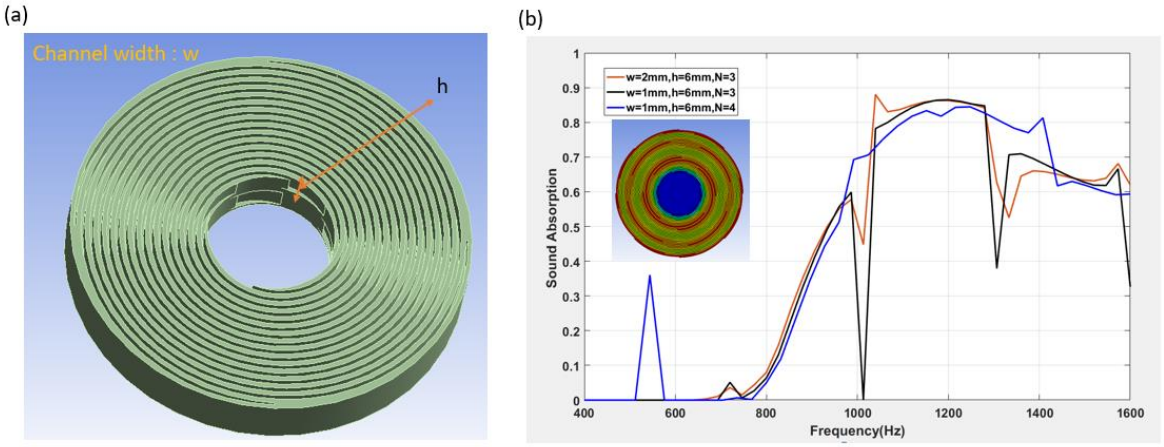

Figure 6.8: (a) Designed meta-structure of N=4 turn spiral ventilated sound absorber. (b) Variation of sound absorption spectrum with respect to changing the geometric configuration of spiral channel.

6.6 Conclusions

To conclude, we proposed a planner-profile meta-unit and subwavelength thickness acoustic air-ventilated barrier, which allows passing the airflow while prohibitive for sound in a broad range. The reported acoustic metamaterials here consist of N spiral resonators' axial coupling to obtain greater bandwidth and multiple sound absorption peaks, which can be possibly used where air-permeable is required. Such design effectively blocks the 90% of the incident energy in the range of 200 -1600 Hz, while its structure thickness is varying from 14mm to 78 mm. We showed how a unique ventilated metamaterial made up of several discs, each of which contains four spiral channels in a single plane, may handle the issues of broadband more than an octave and very low frequency sound (around 200 Hz) while keeping the air circulation between 12% and 5%.

Chapter 7 : Conclusions and future scope

7.1 Conclusions

The objectives of this thesis were to explore and create broadband low-frequency and multiple sound absorption acoustic metamaterials designed for absorbing and attenuating noise, where the sample thickness is significantly smaller than the manipulated wavelength. Additionally, the aim was to construct analytical models to derive straightforward expressions for the effective material properties of metamaterial structures, providing insight into the fundamental physics involved. Furthermore, the thesis sought to design an acoustic metamaterial structure tailored for effectively attenuating very low-frequency noise in waveguides by leveraging innovative acoustic phenomena.

In chapter 2, designing Ashok Chakra acoustic meta-structures for airplanes involves addressing the noise generated by the engine and turbulent airflow around the fuselage, primarily responsible for low-frequency excitations during flight. Cabin noise is notably attributed to these sources, with an average sound pressure level in the 10-500 Hz frequency range reaching around 90 dB(A) for turbojet aircraft. Turbofan-powered aircraft, on the other hand, produce noise in the range of 800 Hz to 12,000 Hz. Thus, our research primarily focused on developing the thinnest acoustic metamaterial to mitigate sound in the low and medium-frequency bands. To tackle these challenges, we initially created thin Ashok Chakra tunable metamaterials with turnability independent of thickness.

In chapter 3, designing tunable fractal structure acoustic meta-structures requires a meticulous choice of structural parameters in the early phases to achieve nearly perfect sound absorption at the desired frequency. Complex geometries, while capable of displaying single-frequency

sound absorption, present challenges in terms of easy manufacturability. Overcoming these challenges involves creating thin sound absorbers that can simultaneously reduce both vertical and lateral dimensions while attaining multiple narrow-band absorption peaks. In response to these difficulties, the objective was to develop a design capable of achieving multiple narrow-band low-frequency sound absorption.

In chapter 4, proposed designing of a Hybrid Fractal broadband acoustic meta-structure involves exploring various approaches. Previous research has explored conventional micro-perforated panels (MPP) with a back cavity, Cascade neck-embedded Helmholtz resonators-based metamaterials, and MPP with neck-embedded Helmholtz resonators. However, achieving broadband sound absorption in these cases often requires a backing cavity thickness exceeding 5 cm. While ultrathin membrane metamaterials (MM) show promise for broadband sound absorption, they face challenges such as membrane loosening over time with repeated use. To overcome these obstacles, we proposed a novel type of tunable micro-perforated face-sheet design backed by fractal geometry. This design features a thickness of less than 2 cm and offers easy programmability and tuning to meet industrial requirements in various fields.

In chapter 5, discuss about designing one-dimensional acoustic metamaterials with ventilation presents a notable departure from the prevalent trend observed in recent years, where the majority of developed acoustic metamaterials with air circulation feature two-dimensional meta-surface geometries, and in some instances, three-dimensional geometries. However, a fundamental flaw in these designs is that most of the sound is reflected back rather than allowing it to pass through, compromising the overall effectiveness. Traditional acoustic barriers have faced challenges in balancing sound-insulating effectiveness with ventilation capacities.

In response to these issues, we proposed a one-dimensional metamaterial design that addresses the limitations by enabling the passage of all incident sound waves (minimizing reflection) while simultaneously absorbing sound.

In chapter 6, In the development of ventilated 2D acoustic metamaterials, researchers incorporated a Fano-like interface to enhance overall ventilation throughout the structure. This approach aimed to attenuate low-frequency sound within a narrow working frequency range centered around each destructive interface frequency. However, this strategy-imposed limitations on the broad applicability of the metamaterial in various engineering fields. The challenge persisted in designing thin, ventilated metamaterials capable of achieving both broadband coverage and exceptional sound absorption.

To overcome these challenges, we introduced a novel solution—a subwavelength-thin metamaterial structure with dimensions ranging from 1.4 cm to 3.5 cm. Inspired by a flat Fresnel spiral, this design not only maintains ventilation capacity but also achieves multiple sound absorption peaks across a broad frequency range from 0 to 1600 Hz.

7.2 Future Scope

The findings outlined in this research highlight the considerable potential of employing additively manufactured acoustic metamaterials for aerospace applications. However, there exist several areas that warrant further exploration and expansion to enhance the concept's performance and render it more practical for real-world applications. The acoustic metamaterials hold promising prospects across various domains.

1. As technology advances, the refinement of metamaterial designs and manufacturing processes is expected to lead to more efficient and versatile

solutions. In the realm of noise control, acoustic metamaterials may find extensive applications in creating sound barriers with unprecedented effectiveness, allowing for tailored acoustic environments in urban settings, transportation, and industrial facilities.

2. Additionally, the integration of smart and adaptive materials into acoustic metamaterials could open avenues for dynamic control of sound absorption and transmission, enabling real-time adjustments to changing environmental conditions.
3. As research continues, acoustic metamaterials may also find applications in novel fields, such as medical imaging and communication, revolutionizing the way we manipulate and control sound waves for diverse purposes.

Ventilated acoustic metamaterials represent a specific subset with a unique potential for addressing challenges in noise control and ventilation simultaneously. Looking ahead, the future scope of ventilated acoustic metamaterials involves:

1. Advancements in the design of structures that seamlessly balance sound absorption and ventilation across a broad frequency spectrum. Researchers are likely to explore new materials and fabrication techniques to enhance the efficiency of these metamaterials, making them applicable in diverse environments.
2. The integration of smart technologies and sensors may also play a role in developing adaptive ventilated acoustic metamaterials that can autonomously respond to varying acoustic conditions. Beyond traditional applications in aerospace and industrial settings, the future may see these materials being employed in architectural designs,

where they can contribute to the creation of acoustically pleasant and well-ventilated spaces in buildings and urban landscapes.

The proposed study can be used for programming acoustic metamaterials. The advancement of intelligent materials and acoustic metamaterials presents effective approaches for mitigating low-frequency acoustic waves. Unlike passive acoustic materials with fixed characteristics, programmable acoustic metamaterials offer the flexibility to alter their working frequency band within a specified range, although this capability is currently limited and costly to produce. The incorporation of intelligent materials introduces new properties such as a wide absorbing frequency band and real-time programmable performances, enabled by innovative energy dissipation mechanisms and adaptive structural changes in response to external stimuli.

Looking ahead, the exploration of reconfigurable 4D-based metamaterials for sound absorption is a promising yet relatively unexplored area. These materials, coupled with artificial intelligence or learning systems, may usher in a new generation of "auto reconfigurable" AMMs capable of outperforming current standards and enabling novel wave functionalities. While the complexity of four-dimensional metamaterials increases due to active components with time-varying parameters, their implementation in acoustics, operating on slower time scales than electromagnetics, may prove more feasible. A notable research avenue involves the development of multifunctional active piezoelectric acoustic metamaterials, where a single structure can exhibit various metamaterial effects under external electrical control. The integration of piezoelectric and polymer materials, facilitated by additive manufacturing technology, provides a pathway for constructing intricate structures with advantageous qualities. As this field progresses, the consideration of factors such as temperature, humidity, external flow, structure curvature, and material qualities becomes

crucial in designing future active piezoelectric AMs. The evolution of alternative materials and fabrication methods will further enhance the capabilities of acoustic metamaterials, playing an increasingly significant role in computational material science, additive manufacturing technology, and various aspects of production and human existence.

ANNEXURE A: MATLAB Code (Fractal metamaterials)

```
clear all
%thickness of 9mm
ro=1.21;
c=343;
f=400:10:1600;
k=(2*pi*f)/c;

L12=1.988*(10)^-3;
L11=10.67*(10)^-3;
sd1=28.8*(10)^-6;
zd1=(ro*c)/sd1;
sc1=28.8*(10)^-6;
h1=7.2*(10)^-3;
sh1=9.5904*(10)^-6;
d1=sqrt(((4*sh1)/pi));
%delt1=0.82*sh1*(1-(1.33*(sh1/sc1)));
Lh1=((1.1988)*(10)^-3)+(1.4*(d1/2));
zc1=(ro*c)/sc1;
zh1=(((ro*c)/sh1)*((0.042+(1i*k*(Lh1+0.75*d1)))));
Zr1=(-1i*zc1*cot(k*h1))+(zh1);
ztr=(-1i*zd1*cot(k*L12));
zx1=(Zr1.*ztr)./(Zr1+ztr);
p1=(zx1/zd1);
w=(p1+(j*tan(k.*L11))./(1+(j*p1.*tan(k.*L11)));
z01=(zd1.*w)*(ro*c);
%y1=abs((z01-1)./(z01+1));
%alpha1=(1-((y1).^2));
%plot(f,alpha1)


Ltr=3*(10)^-3;
L22=6.229*(10)^-3;
L21=11.79*(10)^-3;
sc2=48*(10)^-6;
h2=12*(10)^-3;
sh2=15.984*(10)^-6;
sd2=48*(10)^-6;
d2=sqrt(((4*sh2)/pi));
%delt2=0.82*sh2*(1-(1.33*(sh2/sc2)));
Lh2=((1.998)*(10)^-3)+(1.4*(d2/2));
zd2=(ro*c)/sd2;
zc2=(ro*c)/sc2;
zh2=(((ro*c)/sh2)*((0.042+(j.*k*(Lh2+0.75*d2)))));
Zr2=(-j*zc2*cot(k.*h2))+(zh2);
ztr1=(-j*zd2*cot(k.*Ltr));
zx2=(Zr2.*ztr1)./(Zr2+ztr1);
p2=(zx2/zd2);
w2=(p2+(j*tan(k.*L22)))./(1+(j*p2.*tan(k.*L22)));
zx21=zd2.*w2;
zduct=(ro*c)/sd2;
zeq2=((1./zduct)+(1./zx21)).^-1;
p21=(zeq2/zduct);
w21=(p21+(j*tan(k.*L21)))./(1+(j*p21.*tan(k.*L21)));
```

```
z02=(zduct.*w21)*(ro*c);
%y2=abs((z02-1)./(z02+1));
%alpha2=(1-((y2).^2));
%plot(f,alpha2)


L31=12.026*(10)^-3;
L32=19.644*(10)^-3;
Ltr3=5*(10)^-3;
sc3=80*(10)^-6;
h3=20*(10)^-3;
sh3=26.64*(10)^-6;
sd3=80*(10)^-6;
d3=sqrt(((4*sh3)/pi));
%delt3=0.82*sh3*(1-(1.33*(sh3/sc3)));
L3h=((3.33)*(10)^-3)+(1.4*(d3/2));
zd3=(ro*c)/sd3;
zc3=(ro*c)/sc3;
zh3=(((ro*c)/sh3)*((0.023+(j.*k*(L3h+0.75*d3)))));
Zr3=(-j*zc3*cot(k.*h3))+(zh3*2.67);
ztr3=(-j*zd3*cot(k.*Ltr3));
zx3=(Zr3.*ztr3)./(Zr3+ztr3);
p3=(zx3/zd3);
w3=(p3+(j*tan(k.*L32)))./(1+(j*p3.*tan(k.*L32)));
zx31=(zd3.*w3);
zeq3=((1./zx31)+(1./z02)).^-1;
p31=(zeq3./zd3);
w31=(p31+(j*tan(k.*L31)))./(1+(j*p31.*tan(k.*L31)));
z03=(zd3.*w31)/(ro*c);
%y3=abs((z03-1)./(z03+1));
%alpha3=(1-((y3).^2));
%plot(f,alpha3)

%zoo=(ro*c)/(pi*(0.007)^2);
%L321=9*(10)^-3;
%z=(-j*zoo*cot(k.*L321));
%zfinal=((z.*z03)./((4*z)+z03));
zfinal =(z03/4);
zmeta=(zfinal);
%ztotal=real(zmeta);
%zmeta=(z03/(4*ro*c));

%%perforated plate
d=0.012;
A=pi*(0.012/2)^2;
c=343;
enta=1.814e-5;
t=0.002;
Ro=1.22;
sigma=(d^2)/(4*(0.05^2));
omega=6.283*f;
k=d*sqrt((omega*1.22)/(4*enta));
r=((32*enta*t)/(sigma*Ro*c*d^2))*((sqrt(1+(k.^2/32)))+((sqrt(2)/32))*((k.*
d)/t));
xp=(((omega*t)/(sigma*c)).*(1+((1+(k.^2)/2).^(-0.5))+(0.85*(d/t))));
zs=(r+(j*xp))/A;
```

```
%Zsp=abs(zs);
%zs=(r+(j*xp));
Z=zmeta+(zs/(ro*c));
y=abs((Z-(ro*c))./(Z+(ro*c)));
t=y.^2;
%y=abs((Z-1)./(Z+1));
alpha=(1-t);

plot(f,alpha)
```

ANNEXURE B: Fractal Acoustic Metamaterials

B.1: Origine of Fractal Structure

Fractals, intricate geometric shapes characterized by self-similarity at different scales, find their origins in the pioneering work of mathematician Benoit Mandelbrot in the 1970s. Mandelbrot coined the term "fractal" to describe these structures, which can be found abundantly in nature-ranging from coastlines and mountain ranges to snowflakes and fern leaves. Fractal geometry provides a framework to understand irregular and complex phenomena through simple iterative processes. At the heart of many fractal images lies the Mandelbrot Set, a visual representation of complex numbers and their behavior under iteration. This iconic image, with its infinite intricacies and mesmerizing detail, serves as a gateway to exploring the boundless complexity inherent in the universe.

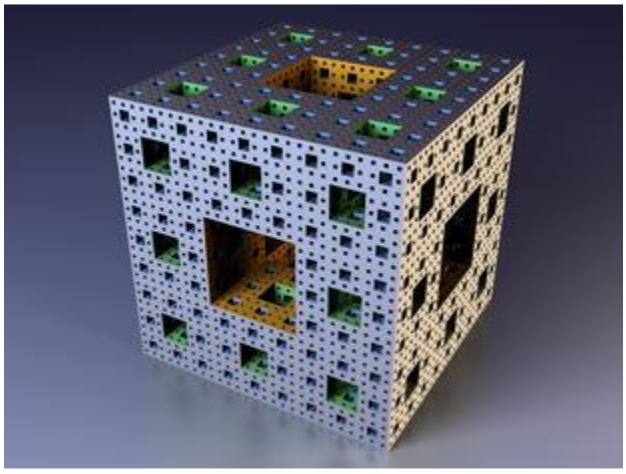

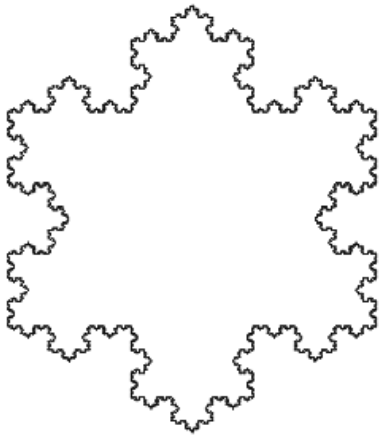

Fractal geometry,[157]

B.2: Analysis of Variance (ANOVA) table of the quadratic regression model.

DF: degree of freedom, Adj SS: adjusted sum of squares, Adj MS: adjusted mean square.

Source	Sum of Squares	df	Mean Square	F-value	p-value	
Model	2.26	27	0.0835	20.88	0.0467	significant
A-dp	0.1507	1	0.1507	37.66	0.0255	
B-w2/w1	0.1506	1	0.1506	37.65	0.0255	
C-l1/l2	0.1527	1	0.1527	38.16	0.0252	
D-tc	0.0111	1	0.0111	2.77	0.2381	
AB	0.0006	1	0.0006	0.1532	0.7333	
AC	0.1507	1	0.1507	37.65	0.0255	
AD	0.0124	1	0.0124	3.11	0.2201	
BC	0.1507	1	0.1507	37.66	0.0255	
BD	0.0003	1	0.0003	0.0625	0.8259	
CD	0.0101	1	0.0101	2.52	0.2530	
A^2	0.1507	1	0.1507	37.65	0.0255	
B^2	0.0008	1	0.0008	0.2101	0.6917	
C^2	0.1506	1	0.1506	37.63	0.0256	
D^2	0.0004	1	0.0004	0.1028	0.7789	
ABC	0.0000	0				
ABD	0.0067	1	0.0067	1.69	0.3237	
ACD	0.0147	1	0.0147	3.69	0.1949	

BCD	0.0000	0				
A^2B	0.0043	1	0.0043	1.07	0.4088	
A^2C	0.1507	1	0.1507	37.65	0.0255	
A^2D	0.0003	1	0.0003	0.0739	0.8112	
AB^2	0.0118	1	0.0118	2.94	0.2283	
AC^2	0.0000	0				
AD^2	0.0091	1	0.0091	2.28	0.2704	
B^2C	0.0000	0				
B^2D	0.0079	1	0.0079	1.96	0.2962	
BC^2	0.0000	0				
BD^2	0.0000	0				
C^2D	0.0000	0				
CD^2	0.0000	0				
A^3	0.0083	1	0.0083	2.08	0.2857	
B^3	0.0263	1	0.0263	6.57	0.1245	
C^3	0.1500	1	0.1500	37.50	0.0256	
D^3	3.793E-07	1	3.793E-07	0.0001	0.9931	
ABCD	0.0000	0				
A^2B^2	0.0000	0				
A^2BC	0.0000	0				
A^2BD	0.0000	0				

A^2C^2	0.0000	0				
A^2CD	0.0000	0				
A^2D^2	0.0000	0				
AB^2C	0.0000	0				
AB^2D	0.0000	0				
ABC^2	0.0000	0				
ABD^2	0.0000	0				
AC^2D	0.0000	0				
ACD^2	0.0000	0				
B^2C^2	0.0000	0				
B^2CD	0.0000	0				
B^2D^2	0.0000	0				
BC^2D	0.0000	0				
BCD^2	0.0000	0				
C^2D^2	0.0000	0				
A^3B	0.0000	0				
A^3C	0.0000	0				
A^3D	0.0000	0				
AB^3	0.0000	0				
AC^3	0.0000	0				
AD^3	0.0000	0				

B^3C	0.0000	0				
B^3D	0.0000	0				
BC^3	0.0000	0				
BD^3	0.0000	0				
C^3D	0.0000	0				
CD^3	0.0000	0				
A^4	0.0000	0				
B^4	0.0021	1	0.0021	0.5225	0.5449	
C^4	0.0000	0				
D^4	0.0000	0				
Residual	0.0080	2	0.0040			
Lack of Fit	0.0080	1	0.0080			
Pure Error	0.0000	1	0.0000			
Cor Total	2.26	29				

B.3: Geometrical outlays (dimensioned), Performance and Potential application

S. No.	Proposed Metamaterials Structure	Dimensions (Thickness)	Performance	Potential Applications
1	Ashok Chakra meta-materials	7mm	This structure was design for the targeted frequency at 1000Hz and it can be tuned by altering the other dimensions	• Interior Cabin Noise Reduction: • Engine Noise Reduction
2	Fractal Meta-structure	5mm (λ/69) to 25 mm (λ/18)	Getting multiple sound absorption peaks at different-different frequency which made him suitable candidate for multiple sound absorber	These alternate structures are light in weight and effective as sound absorbers and serve in many modern industrial applications, such as within aircrafts, automotives, and vibrating machinery.
3	Hybrid cross-microperforated fractal structure	2cm	Demonstrate broad banding sound absorption approximately one-octave low-frequency sound absorption behaviour	• Architectural Acoustics • Aerospace • Industrial setting • Medical imaging

4	One-dimensional ventilated meta-materials	70mm Ventilation is (25-100%)	Demonstrating broadband sound absorption bandwidth of one octave with 0.5-0.9 absorption within the 500-1600 Hz range	• Architectural Acoustics • Industrial noise control • Entertainment spaces
5	2D thin ventilated Meta-materials	14 mm (or 1.4 cm) to 78mm (or 7.8cm).	Very low frequency sound absorption more than 90% (around 200Hz) and broadband more than on octave while maintaining the air circulation of 12% to 5%.	• Motor Shielding • Transformer shielding • Aerospace application • Drone noise control

REFERENCES

[1] F. Monteghetti, “Analysis and Discretization of Time-Domain Impedance Boundary Conditions in Aeroacoustics,” 2018, [Online]. Available: https://tel.archives-ouvertes.fr/tel-01910643.

[2] G. Petrone, G. Melillo, A. Laudiero, and S. De Rosa, “A Statistical Energy Analysis (SEA) model of a fuselage section for the prediction of the internal Sound Pressure Level (SPL) at cruise flight conditions,” *Aerosp. Sci. Technol.*, vol. 88, pp. 340–349, 2019, doi: 10.1016/j.ast.2019.03.032.

[3] L. May, K. Byers-Heinlein, J. Gervain, and J. F. Werker, “Language and the newborn brain: Does prenatal language experience shape the neonate neural response to speech?,” *Front. Psychol.*, vol. 2, no. SEP, pp. 1–9, 2011, doi: 10.3389/fpsyg.2011.00222.

[4] D. Ouis, “Annoyance from road traffic noise: A review,” *J. Environ. Psychol.*, vol. 21, no. 1, pp. 101–120, 2001, doi: 10.1006/jevp.2000.0187.

[5] M. S. Thesis, “A SYSTEM PROPOSAL FOR FAÇADE APERTURES TO PREVENT ACOUSTIC PROBLEMS OF NATURALLY VENTILATED BUILDINGS Department of Architecture Environmental Control and Construction Technologies Programme,” no. January 2012, 2012.

[6] G. Müller and M. Möser, *Handbook of engineering acoustics*. 2013.

[7] Y.-H. Kim, *Sound propagation outdoors*. 2013.

[8] H. H. Huang, C. T. Sun, and G. L. Huang, “On the negative effective mass density in acoustic metamaterials,” *Int. J. Eng. Sci.*, vol. 47, no. 4, pp. 610–617, 2009, doi: 10.1016/j.ijengsci.2008.12.007.

[9] N. Fang, D. Xi, J. Xu, M. Ambati, and W. Srituravanich, “Ultrasonic metamaterials with negative modulus,” vol. 5, no. June, 2006, doi: 10.1038/nmat1644.

[10] D. Zhehua, “Research Progress of Locally Resonance Acoustic Metamaterials,” *E3S Web Conf.*, vol. 248, pp. 4–7, 2021, doi: 10.1051/e3sconf/202124801041.

[11] T. Lee and H. Iizuka, “Bragg scattering based acoustic topological transition controlled by local resonance,” *Phys. Rev. B*, vol. 99, no. 6, pp. 1–11, 2019, doi: 10.1103/PhysRevB.99.064305.

[12] M. Cenedese, E. Belloni, and F. Braghin, “Interaction of Bragg scattering bandgaps and local resonators in mono-coupled periodic structures,” *J. Appl. Phys.*, vol. 129, no. 12, 2021, doi: 10.1063/5.0038438.

[13] Y. Jin *et al.*, “Design of vibration isolators by using the Bragg scattering and local resonance band gaps in a layered honeycomb meta-structure,” *J. Sound Vib.*, vol. 521, no. December 2021, p. 116721, 2022, doi: 10.1016/j.jsv.2021.116721.

[14] P. A. Deymier, *Acoustic Metamaterials and Photonic Crystals*. 2013.

[15] C. Q. Howard and B. S. Cazzolato, *Acoustic Analyses Using Matlab® and Ansys®*. 2017.

[16] J. V. S. Lawrence E. Kinsler, Austin R. Frey, Alan B. Coppens, “Fundamentals of Acoustics,” *Fundamentals of Acoustics*. 2010, doi: 10.1002/9780470612439.

[17] J. V. S. Lawrence E. Kinsler, Austin R. Frey, Alan B. Coppens, “Fundamentals of Acoustics by Lawrence E. Kinsler, Austin R. Frey, Alan B. Coppens, James V. Sanders (z-lib.org).pdf.” p. 567, 2000.

[18] J. Babu, A. Ramacahndran, J. Philip, and C. S. Chandran, “Development of Noise Reduction

Panel Using Piezoelectric Material," *Procedia Technol.*, vol. 25, no. Raerest, pp. 1022–1029, 2016, doi: 10.1016/j.protcy.2016.08.202.

[19] D. Molla, M. Płaczek, and A. Wróbel, "Multiphysics modeling and material selection methods to develop optimal piezoelectric plate actuators for active noise cancellation," *Appl. Sci.*, vol. 11, no. 24, 2021, doi: 10.3390/app112411746.

[20] N. Cselyuszka, M. Sečujski, and V. Crnojević Bengin, "Compressibility-near-zero acoustic metamaterial," *Phys. Lett. Sect. A Gen. At. Solid State Phys.*, vol. 378, no. 16–17, pp. 1153–1156, 2014, doi: 10.1016/j.physleta.2014.02.022.

[21] S. Kumar, P. Bhushan, O. Prakash, and S. Bhattacharya, "Double negative acoustic metastructure for attenuation of acoustic emissions," *Appl. Phys. Lett.*, vol. 112, no. 10, 2018, doi: 10.1063/1.5022602.

[22] X. Wang, X. Luo, H. Zhao, and Z. Huang, "Acoustic perfect absorption and broadband insulation achieved by double-zero metamaterials," *Appl. Phys. Lett.*, vol. 112, no. 2, 2018, doi: 10.1063/1.5018180.

[23] homas L. Szabo, "Time domain wave equations for lossy media obeying a frequency power law," vol. 500, no. October 1985, pp. 491–500, 2000.

[24] J. Mei, G. Ma, M. Yang, Z. Yang, W. Wen, and P. Sheng, "Dark acoustic metamaterials as super absorbers for low-frequency sound," *Nat. Commun.*, vol. 3, 2012, doi: 10.1038/ncomms1758.

[25] T. D. R. (Ed.), *Springer handbook of acoustics*. 2008.

[26] X. Cai, Q. Guo, G. Hu, and J. Yang, "Ultrathin low-frequency sound absorbing panels based on coplanar spiral tubes or coplanar Helmholtz resonators," *Appl. Phys. Lett.*, vol. 105, no. 12, 2014, doi: 10.1063/1.4895617.

[27] M. Yang *et al.*, "Sound absorption by subwavelength membrane structures: A geometric perspective," *Comptes Rendus - Mec.*, vol. 343, no. 12, pp. 635–644, 2015, doi: 10.1016/j.crme.2015.06.008.

[28] C. Fu, X. Zhang, M. Yang, S. Xiao, and Z. Yang, "Hybrid membrane resonators for multiple frequency asymmetric absorption and reflection in large waveguide," *Appl. Phys. Lett.*, vol. 110, no. 2, 2017, doi: 10.1063/1.4973821.

[29] H. Long, Y. Cheng, and X. Liu, "Asymmetric absorber with multiband and broadband for low-frequency sound," *Appl. Phys. Lett.*, vol. 111, no. 14, 2017, doi: 10.1063/1.4998516.

[30] Y. Tang *et al.*, "Hybrid acoustic metamaterial as super absorber for broadband low-frequency sound," *Sci. Rep.*, vol. 7, no. February, pp. 1–11, 2017, doi: 10.1038/srep43340.

[31] A. Sanada and N. Tanaka, "Extension of the frequency range of resonant sound absorbers using two-degree-of-freedom Helmholtz-based resonators with a flexible panel," *Appl. Acoust.*, vol. 74, no. 4, pp. 509–516, 2013, doi: 10.1016/j.apacoust.2012.09.012.

[32] A. O. Krushynska, "Between Science and Art: Thin Sound Absorbers Inspired by Slavic Ornaments," *Front. Mater.*, vol. 6, no. August, pp. 1–12, 2019, doi: 10.3389/fmats.2019.00182.

[33] J. Z. Song, P. Bai, Z. H. Hang, and Y. Lai, "Acoustic coherent perfect absorbers," *New J. Phys.*, vol. 16, 2014, doi: 10.1088/1367-2630/16/3/033026.

[34] C. Zhou, B. Yuan, Y. Cheng, and X. Liu, "Precise rainbow trapping for low-frequency acoustic waves with micro Mie resonance-based structures," *Appl. Phys. Lett.*, vol. 108, no. 6, 2016, doi: 10.1063/1.4941664.

[35] Z. Liang *et al.*, "Space-coiling metamaterials with double negativity and conical dispersion,"

Sci. Rep., vol. 3, pp. 1–6, 2013, doi: 10.1038/srep01614.

[36] C. Chen, Z. Du, G. Hu, and J. Yang, "A low-frequency sound absorbing material with subwavelength thickness," *Appl. Phys. Lett.*, vol. 110, no. 22, 2017, doi: 10.1063/1.4984095.

[37] S. Kumar, T. B. Xiang, and H. P. Lee, "Ventilated acoustic metamaterial window panels for simultaneous noise shielding and air circulation," *Appl. Acoust.*, vol. 159, p. 107088, 2020, doi: 10.1016/j.apacoust.2019.107088.

[38] X. Wu *et al.*, "Low-frequency tunable acoustic absorber based on split tube resonators," *Appl. Phys. Lett.*, vol. 109, no. 4, 2016, doi: 10.1063/1.4959959.

[39] X. Wang, X. Luo, H. Zhao, and Z. Huang, "Acoustic perfect absorption and broadband insulation achieved by double-zero metamaterials," *Appl. Phys. Lett.*, vol. 112, no. 2, 2018, doi: 10.1063/1.5018180.

[40] H. Ruiz, P. Cobo, and F. Jacobsen, "Optimization of multiple-layer microperforated panels by simulated annealing," *Appl. Acoust.*, vol. 72, no. 10, pp. 772–776, 2011, doi: 10.1016/j.apacoust.2011.04.010.

[41] D.-Y. Maa, "Potential of microperforated panel absorber," *J. Acoust. Soc. Am.*, vol. 104, no. 5, pp. 2861–2866, 1998, doi: 10.1121/1.423870.

[42] C. Q. Howard and B. S. Cazzolato, *Acoustic Analyses Using: MATLAB® and ANSYS®*. 2014.

[43] F. Fahy and A. Kalnins, "Sound and Structural Vibration Radiation, Transmission, and Response by Frank Fahy ," *J. Acoust. Soc. Am.*, vol. 81, no. 5, pp. 1651–1651, 1987, doi: 10.1121/1.395099.

[44] V. Romero-Garciá, G. Theocharis, O. Richoux, A. Merkel, V. Tournat, and V. Pagneux, "Perfect and broadband acoustic absorption by critically coupled sub-wavelength resonators," *Sci. Rep.*, vol. 6, no. January, pp. 6–13, 2016, doi: 10.1038/srep19519.

[45] Z. Yang, J. Mei, M. Yang, N. H. Chan, and P. Sheng, "Membrane-type acoustic metamaterial with negative dynamic mass," *Phys. Rev. Lett.*, vol. 101, no. 20, pp. 1–4, 2008, doi: 10.1103/PhysRevLett.101.204301.

[46] J. Guo, X. Zhang, Y. Fang, and R. Fattah, "Reflected wave manipulation by inhomogeneous impedance via varying-depth acoustic liners," *J. Appl. Phys.*, vol. 123, no. 17, 2018, doi: 10.1063/1.5022127.

[47] N. Jiménez, V. Romero-García, V. Pagneux, and J. P. Groby, "Quasiperfect absorption by subwavelength acoustic panels in transmission using accumulation of resonances due to slow sound," *Phys. Rev. B*, vol. 95, no. 1, pp. 1–10, 2017, doi: 10.1103/PhysRevB.95.014205.

[48] J.-P. Groby, R. Pommier, and Y. Aurégan, "Use of slow sound to design perfect and broadband passive sound absorbing materials," *J. Acoust. Soc. Am.*, vol. 139, no. 4, pp. 1660–1671, 2016, doi: 10.1121/1.4945101.

[49] J. Guo and J. Zhou, "An ultrathin acoustic carpet cloak based on resonators with extended necks," *J. Phys. D. Appl. Phys.*, vol. 53, no. 50, 2020, doi: 10.1088/1361-6463/abac2e.

[50] Z. Zhang, Y. Cheng, X. Liu, and J. Christensen, "Subwavelength multiple topological interface states in one-dimensional labyrinthine acoustic metamaterials," *Phys. Rev. B*, vol. 99, no. 22, pp. 2–10, 2019, doi: 10.1103/PhysRevB.99.224104.

[51] C. Zhang and X. Hu, "Three-Dimensional Single-Port Labyrinthine Acoustic Metamaterial: Perfect Absorption with Large Bandwidth and Tunability," *Phys. Rev. Appl.*, vol. 6, no. 6, pp. 1–8, 2016, doi: 10.1103/PhysRevApplied.6.064025.

[52] A. O. Krushynska, F. Bosia, M. Miniaci, and N. M. Pugno, “Spider web-structured labyrinthine acoustic metamaterials for low-frequency sound control,” *New J. Phys.*, vol. 19, no. 10, 2017, doi: 10.1088/1367-2630/aa83f3.

[53] T.-Y. Huang, C. Shen, and Y. Jing, “Membrane- and plate-type acoustic metamaterials,” *J. Acoust. Soc. Am.*, vol. 139, no. 6, pp. 3240–3250, 2016, doi: 10.1121/1.4950751.

[54] Y. Chen, G. Huang, X. Zhou, G. Hu, and C.-T. Sun, “Analytical coupled vibroacoustic modeling of membrane-type acoustic metamaterials: Plate model,” *J. Acoust. Soc. Am.*, vol. 136, no. 6, pp. 2926–2934, 2014, doi: 10.1121/1.4901706.

[55] Y. Chen, G. Huang, X. Zhou, G. Hu, and C.-T. Sun, “Analytical coupled vibroacoustic modeling of membrane-type acoustic metamaterials: Membrane model,” *J. Acoust. Soc. Am.*, vol. 136, no. 3, pp. 969–979, 2014, doi: 10.1121/1.4892870.

[56] N. Jiménez, W. Huang, V. Romero-García, V. Pagneux, and J. P. Groby, “Ultra-thin metamaterial for perfect and quasi-omnidirectional sound absorption,” *Appl. Phys. Lett.*, vol. 109, no. 12, 2016, doi: 10.1063/1.4962328.

[57] S. Huang, X. Fang, X. Wang, B. Assouar, Q. Cheng, and Y. Li, “Acoustic perfect absorbers via Helmholtz resonators with embedded apertures,” *J. Acoust. Soc. Am.*, vol. 145, no. 1, pp. 254–262, 2019, doi: 10.1121/1.5087128.

[58] S. Huang, X. Fang, X. Wang, B. Assouar, Q. Cheng, and Y. Li, “Acoustic perfect absorbers via spiral metasurfaces with embedded apertures,” *Appl. Phys. Lett.*, vol. 113, no. 23, 2018, doi: 10.1063/1.5063289.

[59] S. Bhattacharya, S. Kumar, S. K. Singh, P. Bhushan, M. Sahu, and O. Prakash, “Ashok chakra-structured meta-structure as a perfect sound absorber for broadband low-frequency sound,” *Appl. Phys. Lett.*, vol. 117, no. 19, 2020, doi: 10.1063/5.0022998.

[60] Benoit B. Mandelbrot, “The Fractal Geometry of Nature (Benoit B. Mandelbrot),” *SIAM Review*, vol. 26, no. 1. pp. 131–132, 1984, doi: 10.1137/1026020.

[61] M. Rahimi, F. B. Zarrabi, R. Ahmadian, Z. Mansouri, and A. Keshtkar, “Miniaturization of antenna for wireless application with difference metamaterial structures,” *Prog. Electromagn. Res.*, vol. 145, no. January, pp. 19–29, 2014, doi: 10.2528/PIER13120902.

[62] F. Venneri, S. Costanzo, and G. Di Massa, “Fractal-Shaped Metamaterial Absorbers for Multireflections Mitigation in the UHF Band,” *IEEE Antennas Wirel. Propag. Lett.*, vol. 17, no. 2, pp. 255–258, 2018, doi: 10.1109/LAWP.2017.2783943.

[63] W. J. Krzysztofik, “Fractals in Antennas and Metamaterials Applications,” *Fractal Anal. - Appl. Physics, Eng. Technol.*, 2017, doi: 10.5772/intechopen.68188.

[64] S. Castiñeira-Ibáñez, C. Rubio, V. Romero-García, J. V. Sánchez-Pérez, and L. M. García-Raffi, “Design, manufacture and characterization of an acoustic barrier made of multi-phenomena cylindrical scatterers arranged in a fractal-based geometry,” *Arch. Acoust.*, vol. 37, no. 4, pp. 455–462, 2012, doi: 10.2478/v10168-012-0057-9.

[65] V. Cappello *et al.*, “Ultrastructural characterization of the lower motor system in a mouse model of krabbe disease,” *Sci. Rep.*, vol. 6, no. 1, pp. 1–15, 2016, doi: 10.1038/s41598-016-0001-8.

[66] X. Man, B. Xia, Z. Luo, J. Liu, K. Li, and Y. Nie, “Engineering three-dimensional labyrinthine fractal acoustic metamaterials with low-frequency multi-band sound suppression,” *J. Acoust. Soc. Am.*, vol. 149, no. 1, pp. 308–319, 2021, doi: 10.1121/10.0003059.

[67] D.-Y. Maa, “Potential of microperforated panel absorber,” *J. Acoust. Soc. Am.*, vol. 104, no. 5, pp. 2861–2866, 1998, doi: 10.1121/1.423870.

[68] Y. Li and B. M. Assouar, “Acoustic metasurface-based perfect absorber with deep subwavelength thickness,” *Appl. Phys. Lett.*, vol. 108, no. 6, 2016, doi: 10.1063/1.4941338.

[69] J. W. Sullivan, “A method for modeling perforated tube muffler components. II. Applications,” *J. Acoust. Soc. Am.*, vol. 66, no. 3, pp. 779–788, 1979, doi: 10.1121/1.383680.

[70] J. W. Sullivan and M. J. Crocker, “Analysis of concentric-tube resonators having unpartitioned cavities,” *J. Acoust. Soc. Am.*, vol. 64, no. 1, pp. 207–215, 1978, doi: 10.1121/1.381963.

[71] Suyatno, P. Gontjang, I. Susilo, M. A. Anas, and W. Andi, “Acoustic performance of sonic crystal made from a half of PVC pipe,” *J. Phys. Conf. Ser.*, vol. 1153, no. 1, 2019, doi: 10.1088/1742-6596/1153/1/012009.

[72] S. R. Sundara Bharathi, D. Ravindran, A. Arul Marcel Moshi, R. Rajeshkumar, and R. Palanikumar, “Multi objective optimization of CNC turning process parameters with Acrylonitrile Butadiene Styrene material,” *Mater. Today Proc.*, vol. 27, pp. 2042–2047, 2019, doi: 10.1016/j.matpr.2019.09.055.

[73] J. Christensen and M. Willatzen, “Acoustic wave propagation and stochastic effects in metamaterial absorbers,” *Appl. Phys. Lett.*, vol. 105, no. 4, 2014, doi: 10.1063/1.4892011.

[74] Y. Duan *et al.*, “Theoretical requirements for broadband perfect absorption of acoustic waves by ultra-thin elastic meta-films,” *Sci. Rep.*, vol. 5, no. June, pp. 1–9, 2015, doi: 10.1038/srep12139.

[75] J. Christensen *et al.*, “Extraordinary absorption of sound in porous lamella-crystals,” *Sci. Rep.*, vol. 4, pp. 1–5, 2014, doi: 10.1038/srep04674.

[76] J. Mei, G. Ma, M. Yang, Z. Yang, W. Wen, and P. Sheng, “Dark acoustic metamaterials as super absorbers for low-frequency sound,” *Nat. Commun.*, vol. 3, pp. 756–757, 2012, doi: 10.1038/ncomms1758.

[77] G. D’Aguanno *et al.*, “Broadband metamaterial for nonresonant matching of acoustic waves,” *Sci. Rep.*, vol. 2, pp. 1–5, 2012, doi: 10.1038/srep00340.

[78] L. Fan, Z. Chen, S. Y. Zhang, J. Ding, X. J. Li, and H. Zhang, “An acoustic metamaterial composed of multi-layer membrane-coated perforated plates for low-frequency sound insulation,” *Appl. Phys. Lett.*, vol. 106, no. 15, 2015, doi: 10.1063/1.4918374.

[79] C. Xu, H. Guo, Y. Chen, X. Dong, H. Ye, and Y. Wang, “Study on broadband low-frequency sound insulation of multi-channel resonator acoustic metamaterials Study on broadband low-frequency sound insulation of multi-channel resonator acoustic metamaterials,” vol. 045321, no. February, 2021, doi: 10.1063/5.0047416.

[80] Z. Basiri, M. H. Fakheri, A. Abdolali, and C. Shen, “Non - closed acoustic cloaking devices enabled by sequential - step linear coordinate transformations,” *Sci. Rep.*, pp. 1–14, 2021, doi: 10.1038/s41598-021-81331-3.

[81] Y. Xue and X. Zhang, “Self-adaptive acoustic cloak enabled by soft mechanical metamaterials,” *Extrem. Mech. Lett.*, vol. 46, p. 101347, 2021, doi: 10.1016/j.eml.2021.101347.

[82] A. Phys, “GRIN metamaterial generalized Luneburg lens for ultra-long acoustic jet GRIN metamaterial generalized Luneburg lens for ultra-long acoustic jet,” vol. 144103, no. January, 2021, doi: 10.1063/5.0044436.

[83] S. Hyeon, C. Mahn, Y. Mun, Z. Guo, and C. Koo, “Acoustic metamaterial with negative density,” *Phys. Lett. A*, vol. 373, no. 48, pp. 4464–4469, 2009, doi: 10.1016/j.physleta.2009.10.013.

[84] O. Access, “Wave attenuation mechanism in an acoustic metamaterial with negative effective mass density,” 2009, doi: 10.1088/1367-2630/11/1/013003.

[85] V. M. Garc, “Quasi-two-dimensional acoustic metamaterial with negative bulk modulus,” vol. 184102, pp. 1–8, 2012, doi: 10.1103/PhysRevB.85.184102.

[86] S. H. Lee, C. M. Park, Y. M. Seo, Z. G. Wang, and C. K. Kim, “Composite Acoustic Medium with Simultaneously Negative Density and Modulus,” vol. 054301, no. FEBRUARY, pp. 1–4, 2010, doi: 10.1103/PhysRevLett.104.054301.

[87] I. Kousis and A. L. Pisello, “Double-negative acoustic metamaterials based on quasi-two-dimensional fluid-like shells,” 2012, doi: 10.1088/1367-2630/14/10/103052.

[88] S. Kumar, P. Bhushan, O. Prakash, and S. Bhattacharya, “Double negative acoustic metastructure for attenuation of acoustic emissions,” *Appl. Phys. Lett.*, vol. 112, no. 10, 2018, doi: 10.1063/1.5022602.

[89] and S. B. Sanjeet Kumar Singh Om Prakash, “Novel fractal acoustic metamaterials (FAMs) for multiple narrow-band near-perfect absorption Novel fractal acoustic metamaterials (FAMs) for multiple narrow-band near-perfect absorption,” vol. 035105, no. June, 2022, doi: 10.1063/5.0093128.

[90] B. L. Sound, H. Huang, E. Cao, M. Zhao, S. Alamri, and B. Li, “Spider Web-Inspired Lightweight Membrane-Type Acoustic,” pp. 1–17, 2021.

[91] J. A. Phys, “Sound absorption characteristics of aluminum foam with spherical cells,” vol. 113525, no. June, 2011, doi: 10.1063/1.3665216.

[92] M. E. D. and E. N. Bazley, “Acoustical properties o f fibrous absorbent materials,” no. 3, 1969.

[93] A. Phys, Y. Zhu, and S. Fan, “Extreme low-frequency ultrathin acoustic absorbing metasurface Extreme low-frequency ultrathin acoustic absorbing metasurface,” vol. 173506, no. July, 2019, doi: 10.1063/1.5122704.

[94] D. Maa, “Potential of microperforated panel absorber,” vol. 104, no. July 1998, pp. 2861–2866, 2014.

[95] C. Wang and L. Huang, “On the acoustic properties of parallel arrangement of multiple micro-perforated panel absorbers with different cavity depths,” vol. 130, no. April 2011, 2015, doi: 10.1121/1.3596459.

[96] M. R. Stinson, “sectional shape To (, o,” pp. 550–558, 1991.

[97] K. Sakagami, T. Nakamori, M. Morimoto, and M. Yairi, “Double-leaf microperforated panel space absorbers: A revised theory and detailed analysis,” *Appl. Acoust.*, vol. 70, no. 5, pp. 703–709, 2009, doi: 10.1016/j.apacoust.2008.09.004.

[98] Y. L. Zhiling Zhou, Sibo Huang, Dongting Li, Jie Zhu, “Broadband impedance modulation via non-local acoustic metamaterials,” *Natl. Sci. Rev.*, no. nwab171, pp. 1–297, 2021, doi: 10.1201/9781315366784.

[99] S. Huang *et al.*, “Compact broadband acoustic sink with coherently coupled weak resonances,” *Sci. Bull.*, vol. 65, no. 5, pp. 373–379, 2020, doi: 10.1016/j.scib.2019.11.008.

[100] Q. Xu, J. Qiao, J. Sun, G. Zhang, and L. Li, “A tunable massless membrane metamaterial for perfect and low-frequency sound absorption,” *J. Sound Vib.*, vol. 493, p. 115823, 2021, doi: 10.1016/j.jsv.2020.115823.

[101] H. Nguyen *et al.*, “A broadband acoustic panel based on double-layer membrane-type metamaterials,” *Appl. Phys. Lett.*, vol. 118, no. 18, 2021, doi: 10.1063/5.0042584.

[102] S. K. Singh, O. Prakash, and S. Bhattacharya, “Novel fractal acoustic metamaterials (FAM) for multiple narrow band near perfect absorption,” pp. 1–15.

[103] S.-H. Seo and Y.-H. Kim, “Silencer design by using array resonators for low-frequency band noise reduction,” *J. Acoust. Soc. Am.*, vol. 118, no. 4, pp. 2332–2338, 2005, doi: 10.1121/1.2036222.

[104] J. W. Sullivan, M. J. Crocker, R. W. H. Laboratories, and W. Lafayette, “cavities I _’,” pp. 207–215, 1978.

[105] J. W. Sullivan, “A method for modeling perforated tube muffler components. I. Theory,” *J. Acoust. Soc. Am.*, vol. 66, no. 3, pp. 772–778, 1979, doi: 10.1121/1.383679.

[106] A. You, M. A. Y. Be, and I. In, “Potential of microperforated panel absorber,” vol. 2861, no. 1998, 2016, doi: 10.1121/1.423870.

[107] J. S. Bolton and K. Hou, “Finite Element Models of Micro-Perforated Panels,” 2009.

[108] M. Molerón, M. Serra-Garcia, and C. Daraio, “Visco-thermal effects in acoustic metamaterials: From total transmission to total reflection and high absorption,” *New J. Phys.*, vol. 18, no. 3, 2016, doi: 10.1088/1367-2630/18/3/033003.

[109] V. C. Henríquez, V. M. García-Chocano, and J. Sánchez-Dehesa, “Viscothermal Losses in Double-Negative Acoustic Metamaterials,” *Phys. Rev. Appl.*, vol. 8, no. 1, pp. 1–12, 2017, doi: 10.1103/PhysRevApplied.8.014029.

[110] X. Xiang *et al.*, “Ultra-open ventilated metamaterial absorbers for sound-silencing applications in environment with free air flows,” *Extrem. Mech. Lett.*, vol. 39, p. 100786, 2020, doi: 10.1016/j.eml.2020.100786.

[111] V. Bontozoglou and G. Papapolymerou, “Laminar film flow down a wavy incline,” *Int. J. Multiph. Flow*, vol. 23, no. 1, pp. 69–79, 1997, doi: 10.1016/s0301-9322(96)00053-5.

[112] S. G. Kandlikar, D. Schmitt, A. L. Carrano, and J. B. Taylor, “Characterization of surface roughness effects on pressure drop in single-phase flow in minichannels,” *Phys. Fluids*, vol. 17, no. 10, 2005, doi: 10.1063/1.1896985.

[113] C. Q. Howard and B. S. Cazzolato, *and ANSYS*. .

[114] G. W. Milton, M. Briane, and J. R. Willis, “On cloaking for elasticity and physical equations with a transformation invariant form,” *New J. Phys.*, vol. 8, 2006, doi: 10.1088/1367-2630/8/10/248.

[115] S. A. Cummer and D. Schurig, “One path to acoustic cloaking,” *New J. Phys.*, vol. 9, 2007, doi: 10.1088/1367-2630/9/3/045.

[116] V. M. García-Chocano, J. Christensen, and J. Sánchez-Dehesa, “Negative refraction and energy funneling by hyperbolic materials: An experimental demonstration in acoustics,” *Phys. Rev. Lett.*, vol. 112, no. 14, pp. 11–15, 2014, doi: 10.1103/PhysRevLett.112.144301.

[117] J. Li, L. Fok, X. Yin, G. Bartal, and X. Zhang, “Experimental demonstration of an acoustic magnifying hyperlens,” *Nat. Mater.*, vol. 8, no. 12, pp. 931–934, 2009, doi: 10.1038/nmat2561.

[118] H. He *et al.*, “Topological negative refraction of surface acoustic waves in a Weyl phononic crystal,” *Nature*, vol. 560, no. 7716, pp. 61–64, 2018, doi: 10.1038/s41586-018-0367-9.

[119] T. Liu, X. Zhu, F. Chen, S. Liang, and J. Zhu, “Unidirectional Wave Vector Manipulation in Two-Dimensional Space with an All Passive Acoustic Parity-Time-Symmetric Metamaterials Crystal,” *Phys. Rev. Lett.*, vol. 120, no. 12, p. 124502, 2018, doi: 10.1103/PhysRevLett.120.124502.

[120] S. K. Singh, O. Prakash, and S. Bhattacharya, “Novel fractal acoustic metamaterials (FAMs) for multiple narrow-band near-perfect absorption,” *J. Appl. Phys.*, vol. 132, no. 3, 2022, doi: 10.1063/5.0093128.

[121] G. Ma and P. Sheng, “Acoustic metamaterials: From local resonances to broad horizons,” *Sci. Adv.*, vol. 2, no. 2, 2016, doi: 10.1126/sciadv.1501595.

[122] M. Yang and P. Sheng, “Sound Absorption Structures: From Porous Media to Acoustic Metamaterials,” *Annu. Rev. Mater. Res.*, vol. 47, pp. 83–114, 2017, doi: 10.1146/annurev-matsci-070616-124032.

[123] H. L. Zhang, Y. F. Zhu, B. Liang, J. Yang, J. Yang, and J. C. Cheng, “Omnidirectional ventilated acoustic barrier,” *Appl. Phys. Lett.*, vol. 111, no. 20, 2017, doi: 10.1063/1.4993891.

[124] T. Lee, T. Nomura, E. M. Dede, and H. Iizuka, “Ultrasparse Acoustic Absorbers Enabling Fluid Flow and Visible-Light Controls,” *Phys. Rev. Appl.*, vol. 11, no. 2, p. 1, 2019, doi: 10.1103/PhysRevApplied.11.024022.

[125] M. Sun, X. Fang, D. Mao, X. Wang, and Y. Li, “Broadband Acoustic Ventilation Barriers,” *Phys. Rev. Appl.*, vol. 13, no. 4, p. 1, 2020, doi: 10.1103/PhysRevApplied.13.044028.

[126] L. Shen *et al.*, “Broadband Low-Frequency Acoustic Metamuffler,” *Phys. Rev. Appl.*, vol. 16, no. 6, p. 1, 2021, doi: 10.1103/PhysRevApplied.16.064057.

[127] Z. Su, Y. Zhu, S. Gao, H. Luo, and H. Zhang, “High-Efficient and Broadband Acoustic Insulation in a Ventilated Channel With Acoustic Metamaterials,” *Front. Mech. Eng.*, vol. 8, no. May, 2022, doi: 10.3389/fmech.2022.857788.

[128] X. Xiang, H. Tian, Y. Huang, X. Wu, and W. Wen, “Manually tunable ventilated metamaterial absorbers,” *Appl. Phys. Lett.*, vol. 118, no. 5, 2021, doi: 10.1063/5.0037547.

[129] S. Kumar and H. P. Lee, “Labyrinthine acoustic metastructures enabling broadband sound absorption and ventilation,” *Appl. Phys. Lett.*, vol. 116, no. 13, 2020, doi: 10.1063/5.0004520.

[130] R. Dong, D. Mao, X. Wang, and Y. Li, “Ultrabroadband Acoustic Ventilation Barriers via Hybrid-Functional Metasurfaces,” *Phys. Rev. Appl.*, vol. 15, no. 2, pp. 1–7, 2021, doi: 10.1103/PhysRevApplied.15.024044.

[131] G. Fusaro, X. Yu, Z. Lu, F. Cui, and J. Kang, “A metawindow with optimised acoustic and ventilation performance,” *Appl. Sci.*, vol. 11, no. 7, 2021, doi: 10.3390/app11073168.

[132] J. Du, Y. Luo, X. Zhao, X. Sun, Y. Song, and X. Hu, “Bilayer ventilated labyrinthine metasurfaces with high sound absorption and tunable bandwidth,” *Sci. Rep.*, vol. 11, no. 1, pp. 1–8, 2021, doi: 10.1038/s41598-021-84986-0.

[133] J. Kang and M. W. Brocklesby, “Feasibility of applying micro-perforated absorbers in acoustic window systems,” *Appl. Acoust.*, vol. 66, no. 6, pp. 669–689, 2005, doi: 10.1016/j.apacoust.2004.06.011.

[134] X. Yu, S. K. Lau, L. Cheng, and F. Cui, “A numerical investigation on the sound insulation of ventilation windows,” *Appl. Acoust.*, vol. 117, pp. 113–121, 2017, doi: 10.1016/j.apacoust.2016.11.006.

[135] N. Yuya, N. Sohei, N. Tsuyoshi, and Y. Takashi, “Sound propagation in soundproofing casement windows,” *Appl. Acoust.*, vol. 70, no. 9, pp. 1160–1167, 2009, doi: 10.1016/j.apacoust.2009.04.006.

[136] M. R. Stinson, “The Propagation Of Plane Sound Waves In Narrow And Wide Circular Tubes, And Generalization To Uniform Tubes Of Arbitrary Cross-Sectional Shape,” *J. Acoust. Soc.*

Am., vol. 89, no. 2, pp. 550–558, 1991, doi: 10.1121/1.400379.

[137] M. L. Mujal, "Acoustics of ducts and mufflers with application to exhaust and ventilation system design." 1987.

[138] I. L. Ver and L. L. Beranek, *Noise and Vibration Control Engineering, Second Edition*, vol. 56, no. 4. 2008.

[139] M. H. O. Ipek, O. Serce, H. Karabulut, M. Koru, "Determining Sound Absorbing and Transmission Loss Properties of Rubbers Used in Automotive Industries," *Eurasia Proc. Sci. Technol. Eng. Math.*, vol. 4, pp. 137–148, 2018.

[140] A. Dell, A. Krynkin, and K. V. Horoshenkov, "The use of the transfer matrix method to predict the effective fluid properties of acoustical systems," *Appl. Acoust.*, vol. 182, p. 108259, 2021, doi: 10.1016/j.apacoust.2021.108259.

[141] S. A. Cummer, J. Christensen, and A. Alù, "Controlling sound with acoustic metamaterials," *Nat. Rev. Mater.*, vol. 1, no. 16001, 2016, doi: 10.1038/natrevmats.2016.1.

[142] B. Assouar, B. Liang, Y. Wu, Y. Li, J. C. Cheng, and Y. Jing, "Acoustic metasurfaces," *Nat. Rev. Mater.*, vol. 3, no. 12, pp. 460–472, 2018, doi: 10.1038/s41578-018-0061-4.

[143] Z. Wang, Z. Guo, Z. Li, and K. Zeng, "Design, manufacture, and characterisation of hierarchical metamaterials for simultaneous ultra-broadband sound-absorbing and superior mechanical performance," *Virtual Phys. Prototyp.*, vol. 18, no. 1, 2023, doi: 10.1080/17452759.2022.2111585.

[144] J. Huo, Y. Wang, N. Wang, W. Gao, J. Zhou, and Y. Cao, "Data-driven design and optimization of ultra-tunable acoustic metamaterials," *Smart Mater. Struct.*, 2023, doi: 10.1088/1361-665x/acc36c.

[145] S. K. Singh, O. Prakash, and S. Bhattacharya, "Hybrid fractal acoustic metamaterials for low-frequency sound absorber based on cross mixed micro-perforated panel mounted over the fractals structure cavity," *Sci. Rep.*, vol. 12, no. 1, pp. 1–9, 2022, doi: 10.1038/s41598-022-24621-8.

[146] S. K. Singh, O. Prakash, and S. Bhattacharya, "Novel fractal acoustic metamaterials (FAMs) for multiple narrow-band near-perfect absorption," *J. Appl. Phys.*, vol. 132, no. 3, pp. 1–9, 2022, doi: 10.1063/5.0093128.

[147] J. Yang, J. S. Lee, H. R. Lee, Y. J. Kang, and Y. Y. Kim, "Slow-wave metamaterial open panels for efficient reduction of low-frequency sound transmission," *Appl. Phys. Lett.*, vol. 112, no. 9, pp. 1–5, 2018, doi: 10.1063/1.5003455.

[148] R. Ghaffarivardavagh, J. Nikolajczyk, S. Anderson, and X. Zhang, "Ultra-open acoustic metamaterial silencer based on Fano-like interference," *Phys. Rev. B*, vol. 99, no. 2, pp. 1–10, 2019, doi: 10.1103/PhysRevB.99.024302.

[149] H. L. Zhang, Y. F. Zhu, B. Liang, J. Yang, J. Yang, and J. C. Cheng, "Omnidirectional ventilated acoustic barrier," *Appl. Phys. Lett.*, vol. 111, no. 20, pp. 1–4, 2017, doi: 10.1063/1.4993891.

[150] X. Yu, Z. Lu, L. Cheng, and F. Cui, "On the sound insulation of acoustic metasurface using a sub-structuring approach," *J. Sound Vib.*, vol. 401, pp. 190–203, 2017, doi: 10.1016/j.jsv.2017.04.042.

[151] A. Crivoi, L. Du, and Z. Fan, "Ventilated acoustic meta-barrier based on layered Helmholtz resonators," *Appl. Acoust.*, vol. 205, p. 109263, 2023, doi: 10.1016/j.apacoust.2023.109263.

[152] S. Kumar and H. P. Lee, "Recent advances in acoustic metamaterials for simultaneous sound

attenuation and air ventilation performances," *Crystals*, vol. 10, no. 8, pp. 1–22, 2020, doi: 10.3390/cryst10080686.

[153] G. Xie and X. Wang, "Optimal size design of Fabry-Pérot sound absorbers based on the loss equation," *J. Appl. Phys.*, vol. 130, no. 1, 2021, doi: 10.1063/5.0050502.

[154] N. Jiménez, V. Romero-García, V. Pagneux, and J. P. Groby, "Rainbow-trapping absorbers: Broadband, perfect and asymmetric sound absorption by subwavelength panels for transmission problems," *Sci. Rep.*, vol. 7, no. 1, pp. 1–12, 2017, doi: 10.1038/s41598-017-13706-4.

[155] V. Dubos, J. Kergomard, A. Khettabi, J. P. Dalmont, D. H. Keefe, and C. J. Nederveen, "Theory of sound propagation in a duct with a branched tube using modal decomposition," *Acta Acust.*, vol. 85, no. 2, pp. 153–169, 1999.

[156] A. E-, "Standard Test Method for Impedance and Absorption of Acoustical Materials Using a Tube, Two Microphones and a Digital Frequency Analysis System," *ASTM E 1050-12. ASTM Int. 2012*, vol. i, pp. 4–9, 2012, doi: 10.1520/E1050-102.2.

[157] N. Gordon, "THE MANDELBROT SET , FRACTAL GEOMETRY AND BENOIT MANDELBROT – The Life and Work of a Maverick Mathematician," no. June 2012, 2015, [Online]. Available: https://www.researchgate.net/profile/Nigel_Lesmoir-Gordon2/publication/270285889_THE_MANDELBROT_SET_FRACTAL_GEOMETRY_AND_BENOIT_MANDELBROT_-_The_Life_and_Work_of_a_Maverick_Mathematician/links/54a70a1f0cf256bf8bb6b9f8/THE-MANDELBROT-SET-FRACTAL-GEOMETRY-A.